UC
UNIVERSITY OF
CANTERBURY
Te Whare Wānanga o Waitaha
CHRISTCHURCH NEW ZEALAND

School of Physical and Chemical Sciences
University of Canterbury
Christchurch, New Zealand

ASTR690 MSc Thesis

submitted in partial fulfilment of the requirements for

The Degree of Master of Science in Astronomy

Ray Tracing & Averaging in Szekeres Cosmological Models

---

by

Morag A. Hills

Supervisor: Prof. David L. Wiltshire

2022

Abstract

In this thesis, we perform ray tracing analyses of the COMPOSITE dataset of 4534 galaxy redshifts and distances using quasi-spherical Szekeres models. The Szekeres models are a class of exact inhomogeneous dust solutions of the Einstein equations, which we utilise as toy models of local inhomogeneous structures for distances $\lesssim 150\,h^{-1}$ Mpc. In our case, we choose specific models that asymptote to the FLRW model beyond $\simeq 100\,h^{-1}$ Mpc, to restrict attention to the effects of 'local structure'. These solutions allow us to simulate light propagation through a local under-dense void with an adjacent over-dense structure, as measured by an observer situated at different points within the structures of the model. By ray tracing null geodesics over the sky of this observer while performing radial and angular averages, we have attempted to constrain the Szekeres models to match the Hubble expansion anisotropy of the COMPOSITE dataset, as well as the dipole and quadrupole anisotropies of the Cosmic Microwave Background (CMB). Previous ray tracing investigations undertaken by Bolejko *et al.* [1] have indicated potential non-kinematic contributions to the CMB dipole anisotropy due to relativistic differential expansion on the scale of local inhomogeneities. We revisit these results with corrections applied to a bug in their null vector initialisation procedure that led to some incorrect conclusions. We find that the application of Haantjes transformations to their Szekeres model is a promising avenue for obtaining a full match to the Hubble expansion anisotropy present in the COMPOSITE dataset.

Acknowledgements

First and foremost, I wish to thank my supervisor, Prof. David Wiltshire. I have learnt a tremendous amount of cosmology and general relativity from him while writing this thesis. Not only has he been an outstanding teacher, he has been an incredible mentor and support to me over some difficult times in the past few years. Working with him has been an absolute honour and a pleasure – and I will never tire of learning from him and listening to his many tales of life as a cosmologist.

I wish to thank my family: Mum, Dad and my brother Moe, for always supporting me to follow my dreams and pursue what I love. You are the three brightest stars of my universe, and I love you with all my heart. Special thanks are also due to my Dad for his help in proofreading this thesis.

Last, but certainly not least, I wish to thank all of my amazing friends for supporting me along this journey. I especially wish to thank Rudeep, for his incredible support and guidance in learning general relativity, among many other things. Many thanks are also due to Anastasia, for all the late nights studying together and the much-needed early morning coffee runs.

Contents

Chapter 1

Introduction

Understanding our place within the universe, against the intricate backdrop of cosmic structure and upon the perennial stage of space and time, is an insatiable desire of countless cosmologists and astrophysicists. It begins by kindling a fire in the heart of a starry-eyed student, and before long their burgeoning quest for knowledge propels them far out into a universe beyond their deepest imaginings. Soon enough, they encounter the inevitable limitations imposed by their Earth-bound circumstances. Somehow we must characterise the universe on increasingly large cosmological scales while restricted to just a single vantage point in space and the limits of observations on our past light cone.

Making sense of astronomical observations considering our theoretical conceptions is an exceptionally complicated and nuanced challenge – and not too dissimilar to an art in some cases. The standard ΛCDM model remains the long-standing cosmological concordance model of our universe, due to an excellent agreement with a wide range of observational data. However, there are numerous observations that are yet to be reconciled with the predictions of the standard model, and many of these observations are in significant and increasing tension. This has prompted many cosmologists to return to first principles and question some fundamental assumptions implicit in the justifications of the standard model. Of particular concern are the assumptions of spatial homogeneity and isotropy of the universe over a broad range of cosmic scales, which justifies the use of the FLRW geometry within the ΛCDM framework.

1.1 The Cosmological Principle

By far, the most significant and pervasive principle underpinning modern cosmology and astrophysics is the *cosmological* principle; the assumption that the universe appears the same for all observers when considered on sufficiently large scales. This premise is implicit in the first cosmological models of Einstein in 1917 [2], but it was first explicitly discussed by Milne [3]. However, the principle is based in much deeper reasoning, both physical and philosophical in nature, dating as far back as the critical paradigm shift of the 16^{th} Century Copernican revolution. With the establishment of the heliocentric model as the concordant model of the universe at that time, the notion of the Earth and its observers not residing at any special place in the cosmos became prevalent. This philosophical assumption within cosmology – that we should not reside at any sort of privileged position in space – is aptly referred to as the *Copernican* principle.

Observationally, we determine the Universe to be broadly isotropic in its distribution of structure, which means that it appears the same in all directions. By 'appearing the same' we mean that when averaged over large scales on the order of several hundred Mpc, the distribution of objects such as galaxies is spatially uniform. Since we observe a generally isotropic distribution of galaxies, as well as a very high degree of isotropy in the Cosmic Microwave Background (CMB) over these scales, the same result should apply for other observers provided the Copernican principle holds. However, there is a crucial limitation in that all our observations are made on our past light cone at a single spatial position, and we cannot compare our findings with other observers, except to the extent that it is possible to indirectly infer observations: e.g., the past temperature of the CMB in distant galaxies via the Sunyaev-Zel'dovich effect. Because our vantage point is limited to only a small patch of the full Universe, we must frequently make extrapolations regarding the nature of physics and matter in other observationally inaccessible regions. Although this means our evidence for the Copernican principle is rather indirect, a markedly non-Copernican cosmology would be difficult to reconcile with any physical model of the hot Big-Bang that is consistent with existing observations.

In order to transition from the Copernican principle to the cosmological principle, one must make additional assumptions about the evolution of the universe. In particular, the cosmological principle is generally understood as the statement that the average evolution of the universe is exactly that of a spatially homogeneous and isotropic model within general relativity – namely a model whose energy-momentum tensor evolves in time, but not in space. This is evidently an approximation, as at the late epochs of cosmic history the universe exhibits an increasingly complex networked structure. Tremendously large walls and filaments of galaxy clusters are found bounding a hierarchy of expansive and extremely empty voids, which results in a foam-like appearance on scales of roughly $10 - 100\,\mathrm{Mpc}$. While there is a simplicity in describing the spatial geometry of the universe on scales where the cosmological principle holds, it is less clear how well the average geometry applies on scales where inhomogeneities are pronounced.

Considering this, a refinement of the Copernican principle has been suggested by Wilt-

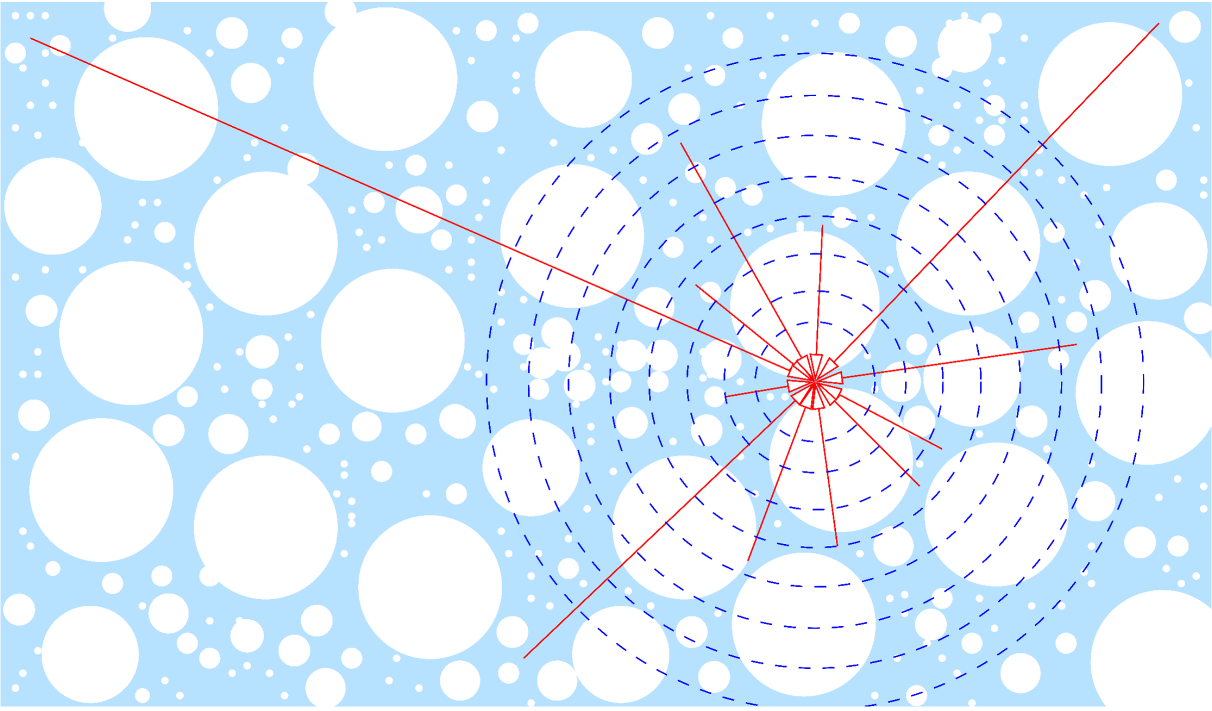

Figure 1.1: A diagram illustrating the process of averaging (in this case for spherical volumes) over large scale cosmic structures. The observable universe is structurally comprised of a networked hierarchy of galactic walls and filaments, with voids of diameter $\sim 30\,h^{-1}$ Mpc accounting for $\sim 40\,\%$ of the volume. Due to significant gradients in spatial curvature arising between regions of dramatically different density (e.g., walls and voids), observers can measure different expansion rates depending on their location. If an observer at a point averages the expansion rate over increasing spherical volumes (dotted lines), eventually they will measure a rate with minimal statistical deviations. This occurs when the spherical volume is much larger than the typical non-linear structures. Image credit: Wiltshire *et al.* [4].

shire [5]. The Copernican principle states that we belong to a class of typical observers, which we indeed are as observers residing within a galaxy. However, by the nature of the universe's structural evolution this produces a selection effect – the typical local environment of all observers and astronomical sources at late epochs are locations where the density of matter is greater than critical. Consequently, our view of the universe is 'mass-biased'. By contrast, most of the volume of space is in freely expanding void regions which are very close to empty – meaning that the volume-averaged viewpoint is very different. Furthermore, there can be significant gradients in spatial curvature between the high density environments of galaxies and the centre of voids. This leads to the question of how the physical quantities of cosmic rulers and clocks should be calibrated relative to volume averages when smoothing over structure. As such, we can expect systematic differences between the measurements of canonical observers in galaxies and the idealised 'volume-average' observers in voids.

1.2 The Standard Model of Cosmology

By assuming both the cosmological and Copernican principles to hold, numerous observations regarding the universe's expansion history support the widespread adoption of the standard ΛCDM model. Often referred to as the 'concordance' cosmological model, it is fundamentally defined by a background Friedmann-Lemaître-Robinson-Walker (FLRW) metric, which is the only solution of the Einstein equations in the case of spatial homogeneity and isotropy. Under these conditions, the geometry of the universe should be invariant under spatial rotations and translations due to the equivalence of spatial dimensions [6]. This reduces the independent components of the metric such that the FLRW metric in comoving coordinates is

$$\mathrm{d}s^2 = g_{\mu\nu}\,\mathrm{d}x^\mu\,\mathrm{d}x^\nu = -\,\mathrm{d}t^2 + a^2(t)\left[\frac{\mathrm{d}r^2}{1-kr^2} + r^2\big(\mathrm{d}\theta^2 + \sin^2\theta\,\mathrm{d}\phi^2\big)\right] \tag{1.1}$$

where $k = -1, 0, +1$ is the spatial curvature parameter and $a(t)$ is the scale factor. Because both the curvature parameter and scale factor under FLRW are not spatially dependent, the same metric prescription is often assumed to apply over all cosmological scales of interest. However, the stipulations of the cosmological principle can only be assumed to apply on scales that are sufficiently large enough to be homogeneous, at least in a statistical sense. Due to this, inhomogeneities on scales[1] below $\sim 100\,h^{-1}$ Mpc are treated in the FLRW framework as initial perturbations upon the constant curvature space of the background metric.

As well as the underlying FLRW background, the ΛCDM model contains another two key ingredients – a cosmological constant in the form of Λ and a cold dark matter (CDM) component. Together, these two components account for 95% of the universe's energy density at the present epoch, with only the remaining 5% residing in the non-relativistic baryonic matter with which we are familiar. These dark components of the universe represent persisting cosmic mysteries. The large amounts of CDM (constituting $\sim 25\%$ of the total energy density at the present epoch) is a matter component which interacts and clumps gravitationally but is yet to correspond to any detected particle. Furthermore, such particles (should they even exist) are not part of the standard model of particle physics and do not interact electromagnetically – meaning they really are 'dark'.

Even more mysterious than the elusive dark matter is the abundant 'dark energy' component – a smooth, pervasive fluid which does not clump gravitationally, and which is therefore distinct from dark matter. This statement can be understood in relation to the energy conditions, which are used to classify all possible forms of matter in general relativity. These conditions are related directly to the locally measured content of the energy momentum tensor $T^{\alpha\beta}$ and indirectly, via the Einstein equations, to the curvature tensor and the geodesic deviation of congruences of timelike and null geodesics. For a congruence of particles with 4–velocity $\mathbf{U}$, and a pressure P related to the local energy density ρc^2 by an equation of state $P = w\rho c^2$, there are several relevant energy conditions that apply specifically to a perfect fluid $T^{\alpha\beta} = (\rho + c^{-2}P)U^\alpha U^\beta + P g^{\alpha\beta}$. These conditions, which also apply in general, are given as follows [7]:

- *Weak energy condition*: $T^{\alpha\beta}W_\alpha W_\beta \geq 0$ for any timelike vector $\mathbf{W}$, and by continuity also for any null vector $\mathbf{W}$. This is equivalent to the statement that the locally measured energy density is positive, $\rho c^2 > 0$. For null vectors, by the Einstein equations the weak energy condition is equivalent to the *null convergence condition*: $R^{\alpha\beta}W_\alpha W_\beta \geq 0$ for any null vector $\mathbf{W}$. When the null convergence condition holds it then follows from the equation of geodesic deviation that the scalar expan-

---

[1] Here h is a dimensionless parameter defined by the value of the Hubble constant $H_0 \equiv \frac{1}{a}\frac{\mathrm{d}a}{\mathrm{d}t}\Big|_{t_0}$, being assumed to be $H_0 = 100\,h\,\mathrm{km/s/Mpc}$.

sion of a non-rotating null geodesic congruence is monotonically decreasing, (i.e., non-diverging). In physical terms, matter causes light rays to focus, a physical requirement for any macroscopic fluid.

- *Strong energy condition*: $T^{\alpha\beta}W_\alpha W_\beta \geq \frac{1}{2}T\,W^\alpha W_\alpha$ for any timelike vector $\mathbf{W}$. For a perfect fluid it can be shown that this leads to the weak energy condition, plus the additional requirement that $w \geq -1/3$ in the equation of state. By the Einstein equations, the strong energy condition is equivalent to the *timelike convergence condition*: $R^{\alpha\beta}W_\alpha W_\beta \geq 0$ for any timelike vector $\mathbf{W}$. This term appears in the equation of geodesic deviation of a timelike congruence – the Raychaudhuri equation. When the timelike convergence condition holds then the scalar expansion of a non-rotating timelike geodesic congruence is monotonically decreasing; i.e., the expansion is decelerating, so that the particles in the congruence clump together.
- *Dominant energy condition*: for any timelike vector $\mathbf{W}$, $T^{\alpha\beta}W_\alpha W_\beta \geq 0$ and $T^{\alpha\beta}W_\alpha$ is a non-spacelike vector i.e., in addition to the weak energy condition holding the locally measured flow vector of the fluid is non-spacelike. For a perfect fluid equation of state this translates to $-1 \leq w \leq 1$, or that physically the speed of sound cannot exceed the speed of light.

An accelerating expansion of timelike geodesics requires a violation of the strong energy condition; i.e., $w < -1/3$ for a perfect fluid 'dark energy' component. Since a cosmological constant is formally equivalent to a perfect fluid with pressure $P = -\rho c^2$, we see that it corresponds to the most extreme equation of state, $w = -1$, consistent with the dominant energy condition.[2]

The cosmological constant has a history as old as relativistic cosmology itself. It was first introduced by Einstein in 1917 [2] with a value finely tuned to balance the attractive self-gravity of a dust fluid, resulting in a static universe. Although the cosmological term was subsequently abandoned by Einstein [9] once the evidence for cosmic expansion emerged in the late 1920s, for several decades Λ went in and out of serious consideration as new astronomical observations of the expansion history were added. In the late 1990s, observations of type Ia supernovae led to the conclusion that they were systematically

---

[2] Since the early 2000s the case $w < -1$, or 'phantom energy', has been readily considered by many observational cosmologists when constraining cosmological parameters. However, if this were a fundamental fluid it would pose tremendous problems such as the violation of local energy-momentum conservation, causality etc. [8].

fainter, and hence at greater distances, than could be possible in a FLRW universe containing only dust (and radiation). The rate of expansion of the FLRW universe had to be accelerating at late cosmic epochs. As noted above, this requires a dominant component of matter which violates the strong energy condition. Since a cosmological constant was historically in the form of 'dark energy' which had been most widely studied, it was immediately adopted into the standard model of cosmology. Nonetheless, over the past 25 years numerous independent observational tests of the expansion history have yielded equations of state for the dark energy component which are consistent with the cosmological constant value, $w = -1$.

In addition to the significant 'dark' components and the small amount of baryonic matter, there are at present miniscule contributions to the total energy density due to tiny fractions of relic CMB photons and background cosmic neutrinos [10]. Just as the CMB photons free-stream to us from the last–scattering epoch at which photons decoupled from electrons in the primordial plasma, the background neutrinos free–stream from an earlier epoch at which neutrinos decoupled from the plasma. This occurred when the average thermal energy was around 1.4 MeV, and corresponds to the energy scale at which the weak interactions that convert neutrons into protons, and vice versa, fell out of equilibrium, resulting in the onset of primordial nucleosynthesis.

The Einstein equations for the FLRW metric (1.1), with a cosmological constant Λ and matter fields with a total density ρ and pressure P, are given by

$$\frac{\dot{a}^2}{a^2} + \frac{kc^2}{a^2} = \frac{8\pi G}{3}\rho + \frac{1}{3}\Lambda c^2\,, \tag{1.2}$$

$$\frac{\ddot{a}}{a} = \frac{-4\pi G}{3}\left(\rho + \frac{3P}{c^2}\right) + \frac{1}{3}\Lambda c^3\,. \tag{1.3}$$

On account of the Bianchi identity, the acceleration equation (1.3) can be derived by combining the Friedmann equation (1.2) with the equation of energy–momentum conservation

$$\dot{\rho} + 3\frac{\dot{a}}{a}\left(\rho + \frac{P}{c^2}\right) = 0\,. \tag{1.4}$$

In the standard cosmological model, the matter fields consist of the total radiation component (both background photons and neutrinos), ρ_r, with pressure $P = \frac{1}{3}\rho_r c^2$, and scales with the total nonrelativistic matter components (both baryons and CDM), ρ_m, which is pressureless. These two components each independently satisfy (1.4), provided they scale with the cosmic scale factor according to $\rho_r \propto a^{-4}$ and $\rho_m \propto a^{-3}$, respectively. Consequently, at early times when $\rho_R \gg \rho_M \gg \rho_\Lambda \equiv c^2\Lambda/(8\pi G)$ the universe is *radiation dominated*, whereas at later epochs when $\rho_M \gg \rho_R \gg \rho_\Lambda$ the universe is *matter domi-*

nated. The last-scattering epoch at $z_{\rm dec} \simeq 1100$ occurs after the epoch when the fractions of matter and radiation are equal at $z_{\rm eq} \simeq 3450$, but before the universe is fully matter dominated.

It is convenient to rewrite the Friedmann equation (1.2) as

$$\Omega_m + \Omega_r + \Omega_k + \Omega_\Lambda = 1, \tag{1.5}$$

where the density parameters are defined by

$$\Omega_m \equiv \frac{8\pi G \rho_m}{3H^2}, \qquad \Omega_r \equiv \frac{8\pi G \rho_r}{3H^2}, \qquad \Omega_k \equiv \frac{-kc^2}{a^2H^2}, \qquad \Omega_\Lambda \equiv \frac{\Lambda c^2}{3H^2}, \tag{1.6}$$

as fractions of the *critical density*, $\rho_{\rm c}(t) = 3H^2(t)/(8\pi G)$, where $H(t) \equiv \dot{a}/a$ is the Hubble parameter. The critical density is that of the Einstein–de Sitter universe with $\Omega_m = 1$, $k = 0$, $\Lambda = 0$ and $\Omega_r = 0$, which has the exact power-law solution $a \propto t^{2/3}$. The Einstein-de Sitter universe [9] corresponds to a critical case, since it just manages to expand forever with only nonrelativistic matter. This is compared to models with $\Lambda = 0$ and $k > 0$ ($\Omega_k < 0$), which recollapse $a \to 0$ at a finite crunch time $t = t_{\rm crunch}$, and models with $\Lambda = 0$ and $k < 0$ ($\Omega_k > 0$) which expand at a rate faster than Einstein-de Sitter, asymptotically reaching the expansion law, $a \propto t$, of an empty Milne universe [3] ($\Omega_m = \Omega_r = \Omega_\Lambda = 0$, $k < 0$) as $t \to \infty$.

For the concordance cosmology, the magnitude of the spatial curvature, $|\Omega_k|$, is small and usually neglected. This leaves a universe with three significant energy density components, Ω_m, Ω_r and Ω_Λ, which evolve as in Fig. 1.2.

Since the densities of matter and radiation both decrease as the volume of the universe increases, whereas the density of the cosmological constant is fixed, then if $\Lambda > 0$ we must eventually arrive at a Λ *dominated* epoch when $\rho_\Lambda \gg \rho_m \gg \rho_r$. In such a future epoch, the scale factor would grow exponentially with time, $a \propto \exp\left(\frac{1}{3}\sqrt{\Lambda}\, ct\right)$, as in the original de Sitter model [12]. However, it turns out that when FLRW models are fit to observational data, then $\rho_{m0} \equiv \rho_m(t_0) \simeq \frac{1}{2}\rho_\Lambda$ at the present epoch $t = t_0$. While $\ddot{a}(t_0) > 0$ as required for cosmic acceleration, $\ddot{a}(t_0) < a^2(t_0)H_0$, where an overdot denotes a derivative with respect to the cosmic time t. This means that the Hubble parameter $H(t) = \dot{a}/a$ is itself still *decreasing* today $\dot{H}(t_0) < 0$, whereas it would reach a positive constant $H(t) \to \sqrt{\Lambda}\, c/3$ as $t \to \infty$, in the epoch of Λ domination. Consequently we appear to be at a very special time in cosmic history, when the universe is just beginning a transition from matter domination to eventual Λ domination. The fact that we live at this special epoch is called the *cosmic coincidence problem.* While one might invoke the

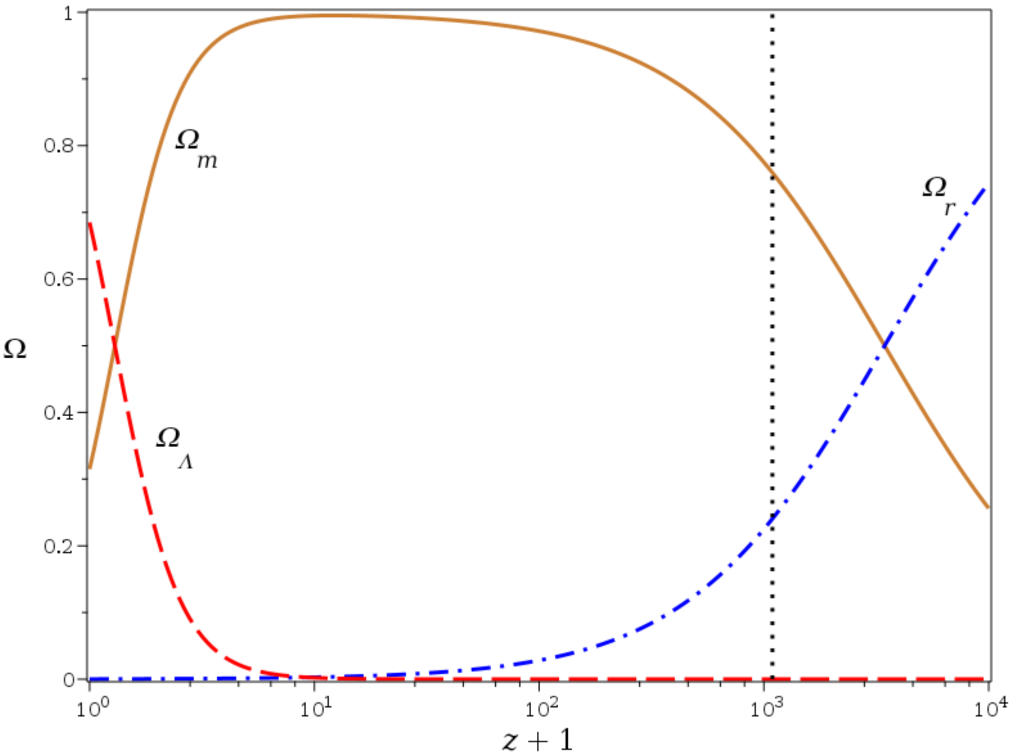

Figure 1.2: Energy densities of matter, Ω_m, radiation, Ω_r, and the cosmological constant, Ω_λ, as a function of $1 + z$ in the spatially flat concordance model. The vertical dotted line indicates the redshift of photon–electron decoupling, $z = 1090$. The parameters have been normalised to the present epoch values from *Planck* [11]: $\Omega_{m0} = 0.315$, $\Omega_{\Lambda 0} = 0.685$ and $\Omega_{r0} = 4.155\, h^{-2} \times 10^{-5}$, where $h = 0.674$ is the Hubble constant normalisation.

anthropic principle to explain this coincidence [13], it could also indicate that this is an aspect of the 'dark energy problem', which demands a more fundamental explanation.

To address the cosmic coincidence problem much effort has been invested in studying cosmological models which introduce one or fundamental dynamical scalar fields [14, 15], for which the phase space of the coupled Friedmann-scalar field equations has late time attractors which switch from decelerating to accelerating expansion. Such ideas include quintessence, K-essence and phantom fields introduced specifically as sources of dark energy, and alternatively scenarios using scalar fields such as the dilaton which appear naturally in string theory – for a review see, e.g., [16].

1.2.1 Redshifts & Distances in the Standard Cosmology

For an ideal comoving source and observer, both at rest with respect to the coordinates of (1.1), the cosmological redshift is

$$(1+z) = \frac{\lambda_{\rm obs}}{\lambda_{\rm em}} = \frac{a(t_0)}{a(t)} \tag{1.7}$$

where 'obs' and 'em' refer to the observer and source/emitter, respectively. For a source of absolute bolometric luminosity $\mathcal{L}$ in its rest frame which is observed with a flux $\mathcal{F}$, the luminosity distance d_L is defined by

$$d_L = \sqrt{\frac{\mathcal{F}}{4\pi\mathcal{L}}} \tag{1.8}$$

By then integrating the Friedmann equation (1.2) or (1.5), one may show that

$$d_L = \frac{c\,(1+z)}{H_0\sqrt{|\Omega_{k0}|}}\,\mathrm{sinn}\left(\sqrt{|\Omega_{k0}|}\int_1^{z+1}\frac{\mathrm{d}x}{\sqrt{\Omega_{\Lambda 0}+\Omega_{k0}x^2+\Omega_{m0}x^3+\Omega_{r0}x^4}}\right)\,, \tag{1.9}$$

where

$$\mathrm{sinn}(x) \equiv \begin{cases} \sin(x), & k=+1\ (\Omega_{k0}<0) \\ x, & k=0 \\ \sinh(x), & k=-1\ (\Omega_{k0}>0) \end{cases}\,. \tag{1.10}$$

Alternatively, for low redshifts we can invert (1.7) to obtain z as a Taylor series in $a(t)$, and a corresponding Taylor expansion of the luminosity-distance independently of the matter fields in the energy-momentum tensor,

$$d_L(z) = \frac{c}{H_0}\left\{ z + \frac{1}{2}\left(1 - q_0\right) z^2 \right.$$
$$\left. - \frac{1}{6}\left(1 - q_0 - 3{q_0}^2 + j_0 + \frac{kc^2}{{H_0}^2{a_0}^2}\right) z^3 + \mathcal{O}\big(z^4\big) \right\}, \qquad (1.11)$$

where $d_L(z)$ is the luminosity distance, $a_0 = a(t_0)$ is the present time scale factor and $k = -1, 0, 1$ is the spatial curvature. The parameters $q_0 = q(t_0)$ and $j_0 = j(t_0)$ are the deceleration and jerk parameters , respectively, which correspond to derivatives of the Hubble parameter $H_0 = H(t_0)$ as follows

$$H(t) = \frac{1}{a}\frac{\mathrm{d}a}{\mathrm{d}t}\,, \qquad q(t) = \frac{-1}{aH^2}\frac{\mathrm{d}^2a}{\mathrm{d}t^2}\,, \qquad j(t) = \frac{1}{aH^3}\frac{\mathrm{d}^3a}{\mathrm{d}t^2}\,. \qquad (1.12)$$

These kinematic parameters can be rewritten in terms of the density parameters for any specific matter model. For example, in the case of (1.5) we have $q_0 = \frac{1}{2}\Omega_{m0} + \Omega_{r0} - \Omega_{\Lambda 0}$.

Actual sources and observers will in general have small peculiar velocities with respect to the ‘cosmic rest frame’. Thus, our actual observed redshift will be

$$(1+z)_{\mathrm{obs}} = (1+z)_{\mathrm{FLRW}}(1+z)_{\mathrm{Doppler}}\,, \qquad (1.13)$$

where $(1+z)_{\mathrm{FLRW}}$ is given by (1.7) and the Doppler term includes local boosts of both the source and observer with respect to the cosmic rest frame at their respective locations. Suppose an observer O detects a photon with frequency ν arriving from the direction with unit vector $\hat{\boldsymbol{n}}$ on the sky. According to observer O, the photon has a 4-momentum $p^\mu = c^{-1}E(1, -\hat{\boldsymbol{n}})$ with energy $E = h\nu$. Another observer O', who is boosted with respect to O, will measure a photon 4-momentum $p'^\mu \equiv c^{-1}E'(1, -\hat{\boldsymbol{n}}') = \Lambda^\mu{}_\nu\, p^\nu$, where

$$\Lambda^\mu{}_\nu = \begin{pmatrix} \gamma & -\gamma\boldsymbol{\beta}^{\mathsf{T}} \\ -\gamma\boldsymbol{\beta} & I + (\gamma - 1)\hat{\boldsymbol{\beta}}\hat{\boldsymbol{\beta}}^{\mathsf{T}} \end{pmatrix}, \qquad \boldsymbol{\beta} = (\beta_x, \beta_y, \beta_z). \qquad (1.14)$$

Here $\beta = |\boldsymbol{\beta}| = v/c$ is the boost parameter, $\hat{\boldsymbol{\beta}} = \boldsymbol{\beta}/\beta$ is a unit vector in the direction of the boost in O’s frame and $\gamma = (1-\beta^2)^{-1/2}$ is the standard Lorentz factor. The time component of the Lorentz transformation, $p'^\mu = \Lambda^\mu{}_\nu\, p^\nu$, gives the well-known Doppler shift

$$\nu' = \gamma(1 + \boldsymbol{\beta}\cdot\hat{\boldsymbol{n}})\nu, \qquad (1.15)$$

while the space component

$$\hat{\boldsymbol{n}}' = \frac{\hat{\boldsymbol{n}} + [\gamma\beta + (\gamma - 1)\hat{\boldsymbol{\beta}} \cdot \hat{\boldsymbol{n}}]\hat{\boldsymbol{\beta}}}{\gamma(1 + \boldsymbol{\beta} \cdot \hat{\boldsymbol{n}})}, \tag{1.16}$$

gives the relativistic *aberration*, which is the change in arrival direction of a photon detected by an observer boosted with respect to the original observer.

From (1.16) we can determine the dot product $\boldsymbol{\beta} \cdot \hat{\boldsymbol{n}}'$, and consequently after a little algebra we find

$$\gamma^2(1 - \boldsymbol{\beta} \cdot \hat{\boldsymbol{n}}')(1 + \boldsymbol{\beta} \cdot \hat{\boldsymbol{n}}) = 1. \tag{1.17}$$

Combining (1.17) and (1.15), we find that the Doppler shift in terms of the direction $\boldsymbol{n}'$ that the boosted observer actually measures is

$$\nu' = \frac{\nu}{\gamma(1 - \boldsymbol{\beta} \cdot \hat{\boldsymbol{n}}')}. \tag{1.18}$$

Consequently, if we neglect the peculiar velocity of the source, the Doppler term in (1.7) for our own observations is conventionally taken to be

$$(1 + z)_{\text{Doppler}} = \frac{\nu}{\nu'} = \gamma(1 - \boldsymbol{\beta} \cdot \hat{\boldsymbol{n}}')\,, \tag{1.19}$$

where $\boldsymbol{\beta}$ is our boost parameter with respect to the cosmic rest frame, namely the frame in which the CMB dipole anisotropy vanishes – as we shall now discuss.

1.2.2 An Overview of the CMB

The cosmic microwave background (CMB) is widely regarded as the most valuable observation in modern cosmology. As the relic bath of radiation left over from the epoch of recombination, the CMB's detailed distribution of temperature fluctuations provides a wealth of information regarding the initial conditions of the universe before large-scale structure formation. In particular, within the framework of the FLRW models, exceptionally precise measurements of the peaks in the power spectrum of fluctuations are used to constrain the key cosmological parameters of the standard model[3].

The primordial universe in the immediate aftermath of the Big Bang consisted of a highly energetic plasma of radiation and fundamental particles. With temperatures exceeding 300,000 K, the formation of the first species of atomic matter was suppressed due to the tight coupling of photons to baryons. Scattering of these photons from free electrons meant that their mean-free-path was too short to allow free-streaming. Consequently, the universe was opaque to radiation at this epoch. Eventually, the rapid expansion and cooling of the universe permitted the first formation of atomic and molecular hydrogen[4], at which stage the photons decoupled from the plasma and began to free-stream through the universe largely uninterrupted. It is this process that produced the characteristic radiation signature of the CMB at a redshift of $z \sim 1100$.

1.2.3 The CMB Dipole Anisotropy

Increasingly precise measurements of the CMB have shown that its spectrum is almost that of an ideal blackbody, with an observed mean temperature of $T_0 = 2.7255\,\mathrm{K}$ [17]. This spectrum is also highly isotropic. When evaluated under a spherical harmonic expansion over the sky, the anisotropies primarily present at the $|\Delta T/T| \leq 10^{-5}$ level after the subtraction of the large monopole and dipole contributions. The dipole is the most prominent anisotropy measured in the CMB, with an amplitude of $3.3645 \pm 0.0020\,\mathrm{mK}$ and an alignment with $(l, b) = (263.99° \pm 0.12°, 48.26° \pm 0.03°)$ in galactic coordinates, when measured in the heliocentric frame [18].

The standard interpretation of the dipole's origin is that it arises due to a special relativistic boost of the observer relative to the uniform frame of the CMB. The dipole must certainly contain a kinematic component, since there is an observed annual modulation of order $|\Delta T/T| \sim 10^{-4}$ due to the Earth's motion around the sun. In the *purely kinematic* dipole interpretation, the 'rest frame' of the CMB is assumed to be that in which the radiation field is most isotropic. One must be careful, however, since general relativity allows for more general anisotropies due to the propagation of light through complex structures.

---

[3] The angular size of the sound horizon, which is determined from the first peak of the power spectrum, is one of the most precise measurements in modern cosmology.

[4] This event is usually known as recombination, although the prefix 're-' is somewhat misleading as this is the first occurrence.

A purely kinematic origin for the CMB dipole can be tested by observations of special relativistic aberration and modulation of the amplitude of the primary CMB anisotropies [19]. Returning to the discussion of section 1.2.1, if we consider an observer travelling with a velocity $\beta = v/c$ relative to an ideal frame in which the mean CMB spectrum is purely isotropic, with $T(\hat{\boldsymbol{n}}) = T_0$ in all directions, then the CMB temperature T they observe will have an anisotropy due to special relativity [20] of the form

$$T'(\hat{\boldsymbol{n}}') = \frac{T(\hat{\boldsymbol{n}})}{\gamma\left(1 - \hat{\boldsymbol{\beta}} \cdot \hat{\boldsymbol{n}}'\right)} \,. \tag{1.20}$$

Here $\hat{\boldsymbol{n}}$ and $\hat{\boldsymbol{n}}'$ are the unit vectors on the sky in the CMB frame and boosted (observer) frames, respectively. This expression still involves the unboosted blackbody temperature $T(\hat{\boldsymbol{n}})$, which can be rewritten in terms of $\hat{\boldsymbol{n}}'$ by first inverting (1.16) to give

$$\hat{\boldsymbol{n}} = \frac{\hat{\boldsymbol{n}}' - [\gamma\beta - (\gamma - 1)\hat{\boldsymbol{\beta}} \cdot \hat{\boldsymbol{n}}']\hat{\boldsymbol{\beta}}}{\gamma(1 - \boldsymbol{\beta} \cdot \hat{\boldsymbol{n}}')} \,. \tag{1.21}$$

Under the purely kinematic interpretation of the CMB dipole, one finds that the Solar system must be moving relative to the CMB frame with a velocity of $369 \pm 0.9\,\mathrm{km\,s^{-1}}$ in the direction of $(l, b) = (263.99° \pm 0.14°, 48.26° \pm 0.03°)$ [19]. Since this gives a small boost of magnitude $\beta = 1.23 \times 10^{-3}$, a Taylor expansion of (1.20) and (1.21) can be applied to give

$$T'(\hat{\boldsymbol{n}}') \approx T_0 \left(1 + \boldsymbol{\beta} \cdot \hat{\boldsymbol{n}}' + (\boldsymbol{\beta} \cdot \hat{\boldsymbol{n}}')^2 - \frac{1}{2}\beta^2 + \mathcal{O}(\beta^2)\right) . \tag{1.22}$$

Consequently, the patch of sky in the direction of motion of the observer will appear blueshifted towards higher temperatures, while the converse occurs for the patch of sky directly opposite. According to the conventional interpretation, an observer who performs a boost of an appropriate velocity in a direction opposite to the observed CMB dipole will observe no dipole, and find themselves ‘at rest’ relative to a universe undergoing a purely isotropic spatial expansion.

1.2.4 Primary & Secondary Sources of CMB Anisotropy

Beginning with work in the early 1990s [22], cosmologists have divided sources of CMB anisotropies into *primary anisotropies*, which largely relate to processes in the early universe and at large scales, and *secondary anisotropies*, which relate solely to the effects of structure formation along the observer’s line of sight.

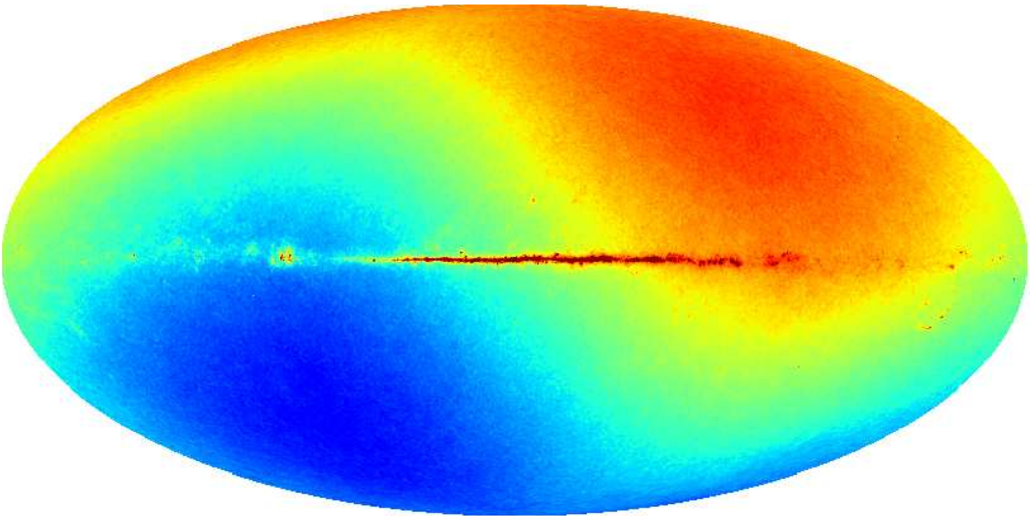

Figure 1.3: The 3.36 mK temperature dipole as seen in a 100 GHz map from the *Planck* NPIPE (PR4) data release. Image credit: Sullivan & Scott [21]

Primary sources of CMB anisotropy include:

- Intrinsic temperature anisotropies in the primordial plasma at the epoch of last scattering.
- Doppler effects associated with velocity perturbations in the primordial plasma at the epoch of last scattering.
- Gravitational redshifts and blueshifts from gravitational potential differences at the last scattering surface. This turns out to be the dominant effect observationally, and is known as the (ordinary) Sachs-Wolfe (SW) effect [23].
- The net effect of additional gravitational redshifts and blueshifts, which arise from time-dependent potentials integrated along an observer's line of sight to the last scattering surface. This is known as the integrated Sachs-Wolfe (ISW) effect.

The ISW effect is typically divided into *early* and *late* time effects. The early ISW effect occurs when radiation is still a significant fraction of the universe's energy density. From fig. 1.2, we note that $\Omega_r \simeq 0.24$ at last scattering ($z = 1090$) and decreases to $\Omega_r = 0.0035$ at $z = 11.24$ when Ω_m reaches its maximum. This is coincidentally close to the epoch of re-ionisation when neutral hydrogen is ionised by radiation from the first generation of stars.

At smaller redshifts, gravitational potentials grow with the advent of large-scale structure formation. When considered relative to a mean cosmic expansion, a photon will be blueshifted as it enters the potential well of an over-density, and redshifted on exiting (the opposite would be true for a photon traversing a void). However, since potentials do gradually evolve in time once one integrates over many of them, there is an observable effect on the received radiation which depends on the given cosmological model. This integrated Sachs-Wolfe (ISW) effect is thus the result of the evolving density perturbations over both early and late epochs of the post-recombination universe.

The ISW effect is usually considered in the regime of perturbation theory on a spatially homogeneous, isotropic background. Nonetheless, one can also consider the effect due to single large structures in the 'non-linear regime'. In the non-linear regime, this source of anisotropy is known as the Rees-Sciama effect [24].

Since the Rees-Sciama effect occurs beyond the scope of linear perturbation theory, it is only important in the late universe, and is therefore often classified as a secondary source of anisotropy.

Other secondary sources of anisotropy include:

- Gravitational lensing on small scales that is associated with cosmic structures.
- The Sunyaev-Zel'dovich (SZ) effect [25, 26], which occurs due to the scattering of CMB photons from ionised gas in dense galaxy clusters.
- The Vishniac effect, a second-order scattering effect associated with bulk motions of free electrons and their correlation with the electron density [27].

Conventionally, the SZ effect is divided into two aspects: (i) the thermal SZ (tSZ) effect associated with random motions of electrons in the intra-cluster gas; and (ii) the kinetic SZ (kSZ) effect associated with any systematic peculiar motion of the cluster relative to the CMB. In particular, the tSZ allows for the determination of the CMB at the location of a rich galaxy cluster. Not only that, one can further determine the temperature of the CMB dipole at this location by using the kSZ effect.

1.2.5 Large Scale CMB Anomalies

Provided that the kinematic interpretation of the CMB dipole is at least partially correct, then we should expect some consequences in our interpretation of the CMB anisotropy power spectrum once the dipole is appropriately subtracted. Anisotropies in the CMB temperature were first measured by the COsmic microwave Background Explorer (COBE) satellite [28], with follow-up analysis on small scales via ground and balloon-based observations [29–31]. The later surveys undertaken by the Wilkinson-Microwave-Anisotropy-Probe (WMAP) and the *Planck* surveyor satellite missions further mapped and identified these anisotropies in exquisite detail. However, over the course of these observations a variety of potentially anomalous features were also identified, many with a statistical significance that has only increased with the precision of measurements. Several of these anomalies are in considerable tension with the expectations of ΛCDM. There is also some debate regarding whether some are systematic or physical in origin, as well as whether they are intrinsic or extrinsic to the observed CMB.

The following features are perhaps the most significant large angle anomalies:

- **A lack of power at large angles:**
  As was first noted by COBE [32] and later confirmed by both WMAP [33–35] and *Planck* [36–38], the angular 2-point correlation function for fluctuations on the largest angular scales is unexpectedly close to zero [39]. This lack of correlation amounts to a lack of perturbations observed in the CMB with respect to the large-scale expectations of ΛCDM, which means that the observed universe is too spatially homogeneous on the largest scales. Moreover, it has been found that all modes below $\ell \leq 5$ contribute to the observed lack of correlation, which is suggestive of correlations between the power spectrum coefficients C_ℓ. These correlations are also not expected under ΛCDM, signalling a violation of the statistical isotropy and scale invariance of CMB fluctuations [40].
- **The hemispherical power asymmetry:**
  Analyses of the first year WMAP data [41] along with subsequent analyses of later WMAP [42, 43] and *Planck* [36–38] data have revealed a north-south hemispherical asymmetry in the CMB power spectrum. When this asymmetry is modelled as a dipolar modulation in the temperature field, one observes a higher temperature variance in the southern hemisphere compared to the north, with the plane that maximises this difference lying very close to the Ecliptic.
- **The quadrupole-octopole alignment:**
  Not only is there a curious alignment of the quadrupole and octopole planes to one another, but these planes are remarkably perpendicular to Ecliptic and further aligned with the CMB dipole [44–48]. This is reasonably unexpected in the context of ΛCDM, as the phases of the anisotropies should be random and uncorrelated.
- **The parity asymmetry:**
  The CMB parity asymmetry concerns the average symmetry of the CMB with respect to reflections about an origin point. There is strong evidence that this parity is violated, as was first noted in the WMAP7 data [49, 50], with the direction of maximum asymmetry for multipoles up to $\ell \sim 20$ seemingly normal to the direction of the CMB dipole. This direction is also close in alignment to the hemispherical

power asymmetry, which suggests that the two anomalies may be linked. There is also a further suggested correlation with the missing large angle power.

- **The cold spot:**
  There is very large – 10° diameter – unusually cold region located in the constellation Eridanus. This was first detected by WMAP and estimated to occur with 1.85% probability in a ΛCDM model with structures growing from Gaussian perturbations in N-body simulations [51]. This was confirmed with a similar level of statistical significance by the *Planck* satellite [36]. While it appears to be causally linked with the Eridanus supervoid, as detected in gravitational lensing studies, it has many puzzling features when compared with the expectations of N-body simulations in ΛCDM [52].

These large angle anomalies highlight the continued need to perform CMB analysis with careful attention towards the data handling and manipulation, as well as the numerous model assumptions involved. It remains an ongoing question as to whether these issues are resolvable within the standard ΛCDM framework, as its specific model assumptions are necessary in deriving key cosmological parameters, such as H_0, from the CMB power spectrum fluctuations.

1.2.6 Challenges for the Standard Model

Despite the overwhelming observational evidence supporting the consistency of ΛCDM, the model still faces some substantial challenges. Of these, the significant tension between determinations of the Hubble constant via a range of probes is of great concern – so much so that it has been deemed a ‘crisis’ for cosmology. The various measurement techniques used in determining the Hubble constant are characterised as either ‘early’ or ‘late’ type, depending on the evolutionary physics of the epoch at which they probe. Early type measurements of H_0 are primarily concerned with the analysis of the CMB and baryon acoustic oscillations (BAO) with respect to the predictions of ΛCDM. Such measurements are indirect estimates of H_0 that are sensitive to the physics of the ΛCDM model at early epochs. As the FLRW model describes physical distances by a time-dependent cosmic scale factor, it is assumed that the evolution of the scale factor remains consistent between early and late epochs.

The flagship ‘late type’ determination of H_0 is via the redshift-distance relationship of the nearby standardizable candles, such as Type Ia Supernovae (SNIa). The intrinsic magnitudes of SNIa are largely similar to each other, despite a scatter of roughly 40% in the peak brightness of their lightcurves [53]. However, as there exist empirical, colour dependent correlations between the SNIa intrinsic magnitudes and time over which the luminosity falls off (e.g. dimmer SNIa are observed to have a faster fall off in peak brightness than those that are brighter), the scatter can be reduced down to less than 15% or to approximately $0.1 - 0.2$ magnitude [53, 54]. By calibrating the supernovae lightcurves in this fashion, their luminosity distance as a function of redshift in the FLRW model and their distance modulus $m - M$ can be used to constrain the Hubble parameter as a function of redshift [55].

Using SNIa luminosity-distance measurements, Riess *et al.* [56] achieve a high-precision estimate of $H_0 = 74.03 \pm 1.42\,\mathrm{km\,s^{-1}\,Mpc^{-1}}$. However, this determination is in significant tension with the best fit *Planck* derived value of $H_0 = 67.4 \pm 0.5\,\mathrm{km\,s^{-1}\,Mpc^{-1}}$ [11]. This disagreement in the value of the Hubble constant is a key characteristic of early-time versus late-time H_0 determinations. Various late-type independent probes, such as gravitational time delays and Mira variables (in lieu of SNIa), are in concerning tensions of $4.5\sigma - 6.3\sigma$ with the results of *Planck* [57]. If the FLRW model is indeed assumed to hold on all cosmological scales and epochs, one would expect a degree of consistency between the various probes. Of course, this is provided that the underlying physics and potential systematic effects of a given probe are properly understood[5].

1.3 The Large-Scale Structure of the Universe

Although there exists astoundingly large dense (but still expanding) structures such as the $\sim 450\,\mathrm{Mpc}$ long Sloan Great Wall [58], the $\sim 495\,\mathrm{Mpc}$ long Huge Large Quasar Cluster [59] and the $1\,\mathrm{Gpc}$ long, $100\,\mathrm{Mpc}$ wide Giant Arc [60], the largest typical structures are voids of diameter $\sim 30\,h^{-1}\mathrm{Mpc}$ [61]. These voids have density contrasts $\delta_\rho \equiv (\rho - \bar{\rho})/\bar{\rho}$ of $\delta_\rho \leq -0.94$ (with $\delta_\rho = -1$ being the minimum density contrast possible when $\rho = 0$) and occupy some 40% of the present epoch universe [62, 63]. Understanding the effects of this complex inhomogeneous hierarchy of structures on our observations involves a variety of considerations, which we shall now discuss in relation to various measurements of anisotropy.

---

[5] The determination of H_0 from SNIa, despite being of high precision, can be finical. Calibrating the lightcurves for scatter requires consideration of the evolutionary behaviour of SNIa at different redshifts, as well as for corrections made for peculiar velocities. Moreover, these corrections are not always apparent in the public releases of SNIa datasets [54]

1.3.1 Scales of Statistical Homogeneity

A far from trivial concern when investigating the role of local inhomogeneities in the Standard Model is the scale at which statistical homogeneity applies. When dealing with averages over observations, it is typical to consider the observed density field in terms of spatial averages [64], which presupposes a split of space and time.

Arnowitt, Deser & Misner (ADM) [65] formulated a general $3+1$ spacetime split by noting that for an arbitrary manifold, one can always locally choose the coordinates,

$$\mathrm{d}s^2 = -\omega^0 \otimes \omega^0 + g_{ij}(t, \mathbf{x})\, \omega^i \otimes \omega^j, \tag{1.23}$$

where $\omega^0 \equiv \mathcal{N}(t, \mathbf{x})\, c\, \mathrm{d}t$, and $\omega^i \equiv \mathrm{d}x^i + \mathcal{N}^i(t, \mathbf{x})\, c\, \mathrm{d}t$ define the ADM lapse function $\mathcal{N}$, and shift vector $\mathcal{N}^i$. These coordinates can also be chosen globally if one restricts the evolution of Einstein's equations to that of irrotational fluids. Then (1.23) may be assumed to apply over global $t = \text{const}$ spatial hypersurfaces Σ_t .

Spatial averages are then defined on a compact domain of the spatial hypersurface Σ_t by

$$\langle \rho(t) \rangle_{\mathcal{D}_R} = \frac{1}{\mathcal{V}(t)} \left(\int_{\mathcal{D}_R} \mathrm{d}^3x \, \sqrt{\det {}^3g}\; \rho(t, \mathbf{x}) \right), \tag{1.24}$$

where

$$\mathcal{V}(t) \equiv \alpha R^3(t) = \int_{\mathcal{D}_R} \mathrm{d}^3x \, \sqrt{\det {}^3g}\,, \tag{1.25}$$

is the volume of the domain $\mathcal{D}_R \subset \Sigma_t$. The metric g_{ij}, where $1 \leq i$ and $j \leq 3$, is the intrinsic metric on the hypersurface Σ_t and α is a dimensionless constant that reflects the choice of geometry. Assuming ergodicity applies (where for a certain stochastic process the ensemble average may be replaced by a spatial average over the volume) [66], a widely used definition of homogeneity presupposes the existence of an average positive density, which is given by the following limit

$$\lim_{R(t) \to \infty} \langle \rho(t) \rangle_{\mathcal{D}_R} = \rho_0(t) > 0\,. \tag{1.26}$$

By further requiring that every point within Σ_t be contained within a domain $\mathcal{D}_{\lambda_0} \subset \mathcal{D}_R$, we can define a homogeneity scale $\lambda_0(t)$ such that

$$\left| \langle \rho(t) \rangle_{\mathcal{D}_R} - \rho_0(t) \right| < \rho_0(t)\,, \qquad \forall R > \lambda_0\,. \tag{1.27}$$

However, this scale greatly depends on the nature of the 2-point correlation function of density fluctuations, as the density field can only be obtained indirectly from the statistical distributions of tracers. Naturally, this determination is subject to the various systematic issues involved in taking both volume and flux limited samples, so practical measures of the statistical homogeneity scale are not directly based on relations such as (1.27). Regardless, the scale of statistical homogeneity $\lambda_0(t)$ demarcates the distance above which density fluctuations are small with respect to the mean and where a perturbative description of the universe is appropriate [64]. Furthermore, the transition to the approximate scale of statistical homogeneity is expected to be gradual, with no clear-cut agreement on its value as yet. Statistical analyses of large galaxy distribution surveys estimate the scale to be of order $70 - 120\, h^{-1}\,\mathrm{Mpc}$ based on the galaxy-galaxy 2-point correlation function [67, 68].

As part of the ΛCDM framework, inflation predicts a near scale invariant primordial density power spectrum, which induces small, almost scale independent fluctuations in the FLRW metric. When evaluating the evolution of structure at large scales, the first order perturbations of the Einstein equations atop a zero order FLRW background are then small enough that the evolution behaves linearly. This domain of structure formation above a given homogeneity scale is commonly referred to as the *linear* regime. Moreover, on decreasingly smaller scales, the linear perturbative approach becomes inapplicable as density fluctuations become increasingly significant. For instance, galaxy clusters can be found with density contrasts of order $\delta_\rho \sim 10^5$, whereas voids (which occupy more of the present epoch universe by volume) have density contrasts of order $\delta_\rho \sim -1$. Structure formation in these domains is evidently in the *non-linear* regime.

1.3.2 Averaging & Backreaction of Inhomogeneities

One of the key questions regarding averaging concerns the scales at which matter and geometry are understood to be coupled in terms of Einstein's equations. This is the 'fitting' problem of cosmology, which was first described by Ellis [69] and Ellis & Stoeger [70]. Einstein's equations are only directly tested on the scale of stellar systems up to super-massive black holes. There is no reason *a priori* to assume that the same equations hold when averaged on scales larger than those over which light has had time to propagate.

In actuality, the transition from the 'few-body' systems of stars and black holes to cosmological scales involves a complex hierarchy of structures, which we can consider schematically as [71]

$$g_{\mu\nu}^{\text{stellar}} \to g_{\mu\nu}^{\text{galaxy}} \to g_{\mu\nu}^{\text{cluster}} \to \left.\begin{array}{c} g_{\mu\nu}^{\text{wall}} \\ \vdots \\ g_{\mu\nu}^{\text{void}} \end{array}\right\} \to g_{\mu\nu}^{\text{universe}}\,. \tag{1.28}$$

Here ‘cluster’ refers to clusters of galaxies and ‘wall’ refers to the thin filaments and sheets of galaxy clusters that thread and surround cosmic voids to form the cosmic web. While the energy-momentum tensor that appears of the right-hand side of Einstein’s equations can be shown to be fluid-like as a result of coarse–graining over non-gravitational degrees of freedom, most steps in the hierarchy (1.28) also involve coarse–graining over gravitational energy, which is non-local. At each step one variously has the rotational energy of galaxies, the binding energy of stars in galaxies and of galaxies in clusters, the thermal energy of galaxies in clusters and, at the final step, the kinetic energy of expansion. Essentially, we are dealing with the problem of fitting one geometry inside another – a complex open problem considering the ambiguities in quantifying quasilocal gravitational energy [72].

If the Einstein equations apply on small scales, one can consider generic averages of them when constructing a coarse-grained or average geometry. Unfortunately, there is no unique way of integrating tensors over a region in general relativity, which is usually the first step in constructing an average. A variety of different approaches have been considered – for a review, see [73] – although the most studied approaches consider averages of scalar quantities associated with Einstein’s equations.

In the widely used spatial averaging scheme due to Buchert [74–76], one considers averages of scalar quantities associated with arbitrary congruences of timelike observers. For simplicity, consider the case in which spacetime is filled with an irrotational dust fluid. In that case, an observer congruence associated with the dust can be chosen so that their 4-velocities U^μ are orthogonal to the $t =$const hypersurfaces. We can then further choose synchronous coordinates with $\mathcal{N} = 1$ and $\mathcal{N}^i = 0$ in the ADM metric (1.23). With these choices, the Einstein equations may be averaged on a domain, $\mathcal{D}$, of the spatial hypersurfaces, Σ_t, to give

$$\begin{aligned} 3\frac{\dot{\bar{a}}^2}{\bar{a}^2} &= 8\pi G\left<\rho\right> - \frac{1}{2}c^2\left<\mathcal{R}\right> - \frac{1}{2}\mathcal{Q}, && (1.29)\\ 3\frac{\ddot{\bar{a}}}{\bar{a}} &= -4\pi G\left<\rho\right> + \mathcal{Q}, && (1.30)\\ \partial_t\left<\rho\right> + 3\frac{\dot{\bar{a}}}{\bar{a}}\left<\rho\right> = 0, & && (1.31)\end{aligned}$$

where an overdot denotes a t–derivative. The term $\mathcal{Q}$ is referred to as the *kinematic* *backreaction*, and is given by

$$\mathcal{Q} \equiv \frac{2}{3}\left\langle \Big(\Theta - \langle\Theta\rangle\Big)^2 \right\rangle - 2\left\langle\sigma^2\right\rangle = \frac{2}{3}\left(\left\langle\Theta^2\right\rangle - \langle\Theta\rangle^2\right) - 2\left\langle\sigma^2\right\rangle \,, \tag{1.32}$$

where $\sigma = \frac{1}{2}\sigma^{\alpha\beta}\sigma_{\alpha\beta}$ is the scalar shear of the congruence, $\sigma_{\alpha\beta} \equiv \nabla_{(\alpha}U_{\beta)}$, and $\Theta = \nabla_\alpha U^\alpha$ is the expansion of the congruence. In (1.29)–(1.32), angle brackets denote the spatial volume averages, as defined earlier in (1.24) and (1.25).

These equations look very similar to the Friedmann equations (1.2) and (1.3). However, there is an important difference: $\bar{a}$ is *not* the scale factor of any given geometry, but rather it is defined in terms of the average volume according to

$$\bar{a}(t) \equiv \left[\mathcal{V}(t)/\mathcal{V}(t_0)\right]^{1/3} . \tag{1.33}$$

It follows that the Hubble parameter appearing in (1.29)–(1.31) is related to the volume-average expansion scalar Θ, by

$$\frac{\dot{\bar{a}}}{\bar{a}} = \frac{1}{3}\langle\Theta\rangle \,. \tag{1.34}$$

The condition

$$\partial_t\left(\bar{a}^6\mathcal{Q}\right) + \bar{a}^4c^2\partial_t\left(\bar{a}^2\langle\mathcal{R}\rangle\right) = 0, \tag{1.35}$$

is required to ensure that (1.29) is the integral of (1.30).

In Buchert's scheme, the non-commutativity of averaging and time evolution is described by the exact relation [74]

$$\partial_t\langle\Psi\rangle - \langle\partial_t\Psi\rangle = \langle\Psi\Theta\rangle - \langle\Theta\rangle\langle\Psi\rangle \,, \tag{1.36}$$

for any scalar Ψ. This is an example of a generic feature of *backreaction* in averaging schemes. The process of constructing an Einstein tensor for an average geometry evolving in time will not, in general, coincide with the time evolution of an initially averaged geometry.

Equation (1.30) is suggestive, since it implies that if the backreaction term is large enough – e.g., for a large variance in expansion with small shear – then the volume average acceleration (1.30) could be positive. This occurs if $\mathcal{Q} > 4\pi G\langle\rho\rangle$, even though the expansion of all regions may be locally decelerating. Although the initial fraction of the volume occupied by the faster expanding voids is tiny, this fraction may nonetheless become significant at late epochs, skewing the average to give an illusion of acceleration during the transition to void domination.

While our universe certainly is void dominated, whether such an interpretation is correct depends on the realistic initial density perturbations, their subsequent evolution, and the operational interpretation of the Buchert formalism. Since Buchert's averaging formalism is a statistical one, additional assumptions are required to relate solutions of the Buchert equations (1.29)–(1.32) to cosmological observations. For example, Wiltshire's timescape scenario [5, 77] involves a reinterpretation of the Buchert scheme in which the time parameter t, which is associated with statistical averages, drifts away from the proper time of observers deep within bound structures with the evolution of the cosmic web. In this case, the interpretation of 'cosmic acceleration' does not simply involve equation (1.30).

In this thesis, we will not be concerned with cosmological averages and their evolution on the largest scales. Rather, we will consider the effects of inhomogeneities on light propagation for scales $\lesssim 100\, h^{-1}\,\mathrm{Mpc}$, on which a simple average homogeneous expansion does not apply.

1.3.3 Light Propagation through Inhomogeneities

Due to our 'mass-biased' perspective of the evolving universe, it is greatly important to consider the influence of large-scale structure on the propagation of light from source to observer. Concerning SN1a, which are key observables in determining the universe's expansion rate, a light ray bundle propagating from a given source to the observer will typically traverse regions that are both over-dense and under-dense with respect to the background cosmological model. Consequently, the angular diameter distance d_A will undergo focussing effects according to the Sachs optical equations [1, 23]

$$\frac{\mathrm{d}^2 d_A}{\mathrm{d}s^2} = -\left(\hat{\sigma}^2 + \frac{1}{2}R_{ab}k^a k^b\right) d_A\,, \tag{1.37}$$

where $\hat{\sigma} = \frac{1}{2}\hat{\sigma}_{ab}\,\hat{\sigma}^{ab}$ is the scalar shear of the null geodesic bundle, R_{ab} is the Ricci curvature and k^a is the tangent to the null geodesics of the congruence. The light ray bundle will hence be influenced by matter both outside and inside the beam to varying extents. Bundles that traverse regions primarily consisting of a smooth continuum of matter will be subject to *Weyl focussing*, which pertains to the shear term of (1.37). Conversely, a bundle which traverses regions of minimal matter will be subject to *Ricci focussing*, which pertains to the Ricci curvature term of (1.37). By the reciprocity theorem [78], the luminosity distance to the source is then

$$d_L = (1+z)^2\, d_A\,. \tag{1.38}$$

On the scales of $z \lesssim 0.1$ considered in our present investigation, the effects associated with Weyl focussing are negligible due to the magnitude and gradient of the density contrasts involved. However, even for small-scale inhomogeneities within a largely homogeneous universe, the focussing induced distance deviations can be on the order of a few percent relative to an exactly homogeneous universe.

1.3.4 Peculiar Velocities & Bulk Flows

When measuring the redshifts of objects such as individual galaxies on the sky, one typically attributes any deviations from a linear Hubble flow in the cosmic rest frame to random peculiar velocities induced by nearby gravitational interactions (e.g. , clustering). If we take (1.7) and assume that the observer is comoving with the cosmic rest frame, then the Doppler term can be attributed entirely to a peculiar velocity of the source. In that case, according to an observer in the cosmic rest frame at the source location the photon has a 4-momentum $p^\mu = c^{-1}E(1, -\hat{\boldsymbol{n}})$ as before, but in the boosted source frame the photon 4-momentum is now $p'^\mu = \Lambda^\mu{}_\nu\, p^\nu = c^{-1}E'(1, \hat{\boldsymbol{n}}')$, since the photon is outgoing. Then $\nu'/\nu = \gamma\,(1 + \boldsymbol{\beta}\cdot\hat{\boldsymbol{n}})$. Consequently, combining this with (1.7) the locally observed redshift is

$$\begin{aligned} cz &= c(\gamma-1) + \gamma\left[cz_{\mathrm{FLRW}} + \boldsymbol{v}\cdot\hat{\boldsymbol{n}}(1+z_{\mathrm{FLRW}})\right] \\ &\simeq cz_{\mathrm{FLRW}} + \boldsymbol{v}\cdot\hat{\boldsymbol{n}}(1+z_{\mathrm{FLRW}}) + \mathcal{O}\left(\beta^2\right) \qquad (1.39) \\ &\simeq cz_{\mathrm{FLRW}}\left[1+\mathcal{O}(\beta)\right] + \boldsymbol{v}\cdot\hat{\boldsymbol{n}}\,. \qquad (1.40) \end{aligned}$$

The Newtonian velocity addition approximation is commonly used in the literature, neglecting the $\mathcal{O}(\beta)$ correction. This is at most 0.5% for the data sets considered, which is typically at least one order of magnitude smaller than typical distance uncertainties.

With respect to a linear Hubble law, $cz_{\mathrm{FLRW}} = H_0\, r$, and in the limit that the $\mathcal{O}(z^2)$ terms in (1.11) can be neglected, a given object's peculiar velocity is thus interpreted as

$$v_{pec} \equiv \boldsymbol{v}\cdot\hat{\boldsymbol{n}} = cz - H_0\, r \tag{1.41}$$

where z is the redshift of the object and r is the object's luminosity distance. However, this assumes a standard of rest to exist, at least on large scales, such that the deviations described by (1.41) become negligible at increasing redshifts. En masse, the motions of galaxies within galaxy surveys are analysed to ascertain their bulk motion, which is obtained from the dipole in the peculiar velocity field of the sample. In the rest frame of the CMB, the observed peculiar velocity field of galaxies at distances $\boldsymbol{r}$, as determined from perturbation theory on a spatially FLRW background [79] is

$$\boldsymbol{v}(t_0, \boldsymbol{r}) = \frac{\Omega_{m0}^{0.55}}{4\pi} \int \mathrm{d}^3\boldsymbol{r}' \; \delta_m(\boldsymbol{r}') \, \frac{(\boldsymbol{r}' - \boldsymbol{r})}{|\boldsymbol{r}' - \boldsymbol{r}|^3} \,, \tag{1.42}$$

where Ω_{m0} is the present time matter density and δ_m is the density contrast with respect to the FLRW background. The power of 0.55 is obtained from a fitting formula for models with dark energy [80].

If the CMB dipole is to be interpreted purely kinematically, then it should be decomposed to account for our own known motions. Actual astronomical measurements are referred to the heliocentric frame, which integrates out the annual motion around the Sun. Furthermore, once we consider the systems to which we are gravitationally bound, we can account for the motion of the Sun within the Milky Way, and the motion of the Milky Way with respect to the Local Group (LG) of galaxies. On scales $\gtrsim 2\,\mathrm{Mpc}$, space is expanding, however. To account for the CMB dipole that would be measured in the LG rest frame within special relativity requires a boost velocity of [81]

$$635 \pm 38\,\mathrm{km\,s^{-1}} \quad \text{in the direction} \quad (\mathrm{l},\mathrm{b}) = (276.4^\circ, 29.3^\circ) \pm 3.2^\circ \,, \tag{1.43}$$

which is in the constellation of *Hydra*.

Over the last few decades, astronomers have sought to account for this motion in terms of the gravitational pull of large-scale fluctuations in the mass density. To resolve the CMB dipole, the boost (1.43) should be consistent with estimates determined from integrating the density field of nearby structures using (1.42) in perturbation theory, and its nonlinear extensions via N–body simulations. Once the boost (1.43) has been accounted for in terms of the *clustering dipole* of nearby structures, then the spherical average of the velocity field (1.42) should tend to zero as the distance r is further increased, at a rate consistent with a stochastic field of density perturbations produced by realistic simulations.

With the 1988 discovery of a large dense region known as the Centaurus–Hydra complex or the ‘Great Attractor’ [85], there were early hopes that CMB dipole could be fully accounted for. However, as years have gone by this hope has not been realised. Measurements of the density field are complicated by the systematics of volume–limited and flux–limited surveys, as well as other systematic biases which have to be carefully

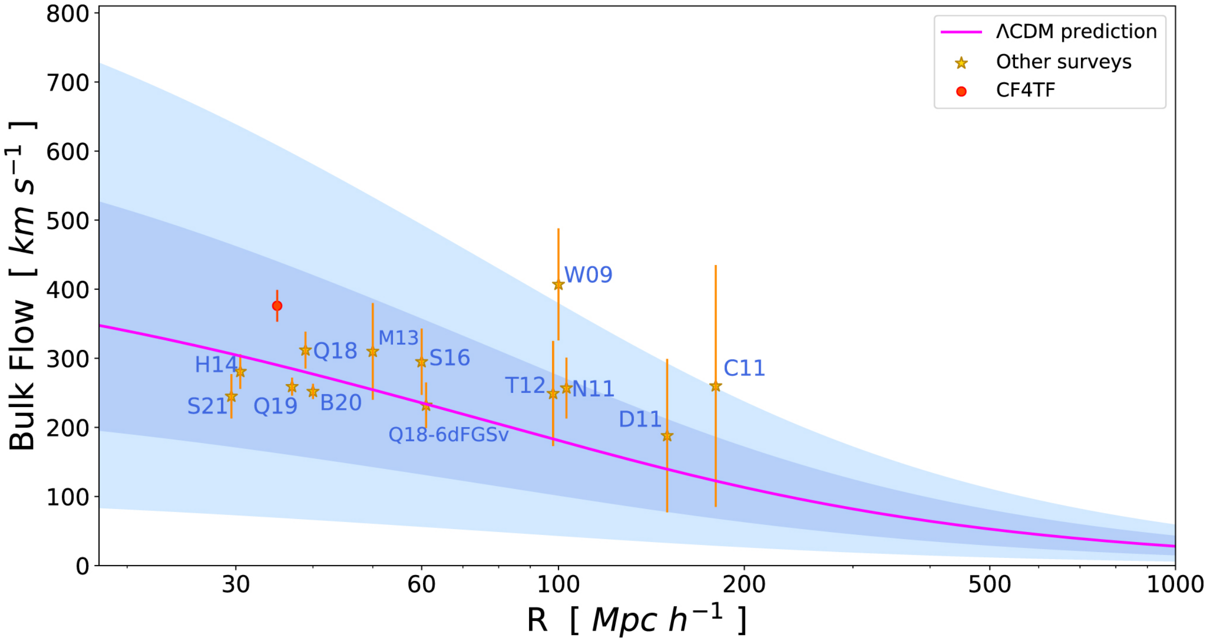

Figure 1.4: A comparison of various bulk flow amplitude estimates as a function of the survey depth for 13 surveys. CF4TF refers to the *Cosmicflows-IV* Tully-Fisher catalogue, while W09 refers to the bulk flow analysis of the COMPOSITE sample by Watkins, Feldman & Hudson [82, 83]. Image credit: Qin *et al.* [84].

accounted for.

The general lack of convergence of numerous bulk flow measurements towards a scale of statistical homogeneity remains a cause for concern. A variety of these measurements, with survey depths ranging from $30-200\,h^{-1}$ Mpc, all report bulk flow amplitudes that are within $200-400\,\mathrm{km\,s^{-1}}$, as shown in fig. 1.4. These bulk flows are largely consistent in their direction on the sky, despite the range of estimation techniques that different investigations employ. While surveys with smaller depths appear consistent with the predictions of ΛCDM, the amplitude of the bulk flows persist beyond the widely suggested $100\,h^{-1}$Mpc scale of statistical homogeneity. The Shapley concentration at a distance of $\sim 125-150\,h^{-1}$ Mpc has been suggested as a candidate for the major contribution to the clustering dipole. However, observations beyond the Shapley concentration have failed to find the expected in-fall on the opposite side of the structure [86].

In this thesis, we will analyse the COMPOSITE dataset, which has one of the larger survey depths shown in fig. 1.4. In their analysis of the COMPOSITE dataset, Watkins *et al.* [82] determined a significantly large bulk flow of $407 \pm 81\,\mathrm{km\,s^{-1}}$ within a Gaussian window of radius $50\,h^{-1}$ Mpc in the direction of $(l, b) = (287^\circ \pm 9^\circ, 8^\circ \pm 6^\circ)$. The bulk flow amplitude is over 2σ larger than that expected under ΛCDM, and larger than some other surveys of a similar depth. The COMPOSITE sample has been chosen for our analysis for reasons of its large size, depth, treatment of particular systematic biases and its sky coverage. This is essential for the analysis we undertake, as is further discussed in section

3.3.2.

1.3.5 Dipoles in Cosmic Source Populations

If the kinematic interpretation of the CMB dipole is correct, then it will have consequences that extend to any populations of cosmic sources at large redshifts which statistically are homogeneously distributed in the cosmic rest frame. It was first demonstrated by Ellis & Baldwin in 1984 [87] that the kinematic dipole feature should be detectable via the effects of special relativistic modulation and aberration in observations of the number counts of distant radio sources. For such populations of cosmic radio sources, both the individual and averaged spectra are expected to follow a power law of the form

$$S(\nu) \propto \nu^{-\alpha}, \tag{1.44}$$

where S is the flux density, ν is the frequency and α is the spectral index for a given individual source (or the average of the population).

The integral number count of the population per unit solid angle above a limiting flux limit can also be expressed with the following power law,

$$\frac{\mathrm{d}N}{\mathrm{d}\Omega}(> S) \propto S^{-x}, \tag{1.45}$$

where the value of the constant x may vary with the specifics of the population survey. Provided that the rest frame of the distant source population presumably coincides with the most uniform frame of the CMB, an observer moving with a velocity v with respect to this frame will observe a Doppler shifted source frequency of

$$\nu_{\mathrm{obs}} = \nu_{\mathrm{rest}}\delta\,, \tag{1.46}$$

where by (1.15) the function δ is given by

$$\delta = \gamma(1 + \beta\,\hat{\boldsymbol{\beta}} \cdot \hat{\boldsymbol{n}}) = \frac{1 + (v/c)\cos\theta}{\sqrt{1 - (v/c)^2}}\,. \tag{1.47}$$

Recall from section 1.2.1 that the angle $\theta = \cos^{-1}(\hat{\boldsymbol{\beta}}\cdot\hat{\boldsymbol{n}})$ gives the position of the source from the direction of the observer's velocity $\boldsymbol{v} = c\boldsymbol{\beta}$, with the angle measured in the 'cosmic rest frame' at the observer's location. Because of the dependence of the observed frequency on the angle of the source, it follows through (1.44) and (1.45) that the observed number count will be greatest in the direction of the observer's motion. This is the *relativistic* *modulation* effect associated with a Lorentz boost.

Relativistic modulation is a particularly important consideration when conducting flux limited surveys, as there will be a kinematic enhancement of the flux that brings otherwise excluded sources into the survey volume. As the observed flux of a source is proportional to its fixed frequency

$$S_{\mathrm{obs}}(\nu_{\mathrm{obs}}) \propto S_{\mathrm{rest}}(\nu_{\mathrm{obs}})\, \delta^{1+\alpha} \propto \delta\, \nu_{\mathrm{rest}}^{-\alpha} \propto \delta^{1+\alpha}\, \nu_{\mathrm{obs}}^{-\alpha}\,, \tag{1.48}$$

the flux-limited observed number density is given by

$$\left(\frac{\mathrm{d}N}{\mathrm{d}\Omega}\right)_{\mathrm{obs}} = \left(\frac{\mathrm{d}N}{\mathrm{d}\Omega}\right)_{\mathrm{rest}} \delta^{x(1+\alpha)}\,. \tag{1.49}$$

By then considering the aberration of the source positions due to the observer's motion, where the elements of the solid angle in the direction of θ are related through

$$\mathrm{d}\Omega_{\mathrm{obs}} = \mathrm{d}\Omega_{\mathrm{rest}}\ \delta^{-2}\,, \tag{1.50}$$

the observed number count for $v/c \ll 1$ and $\delta \approx [1 + (v/c)\cos\theta]$ to first order is then

$$\left(\frac{\mathrm{d}N}{\mathrm{d}\Omega}\right)_{\mathrm{obs}} = \left(\frac{\mathrm{d}N}{\mathrm{d}\Omega}\right)_{\mathrm{rest}} \left[1 + [2 + x(1+\alpha)]\left(\frac{v}{c}\right)\cos\theta\right]. \tag{1.51}$$

By assuming that the sources are indeed isotropically distributed within their rest frame i.e., provided the cosmological principle holds on the scale of interest, we should observe a number count dipole of kinematic origin on the sky with an amplitude of $\mathcal{D}_N = [2 + x(1+\alpha)]\,(v/c)$.

At the time of publication in the early 1980s, Ellis & Baldwin [87] were limited in testing their hypothesis due to the unavailability of sufficiently large source catalogues. However, the great advancements in the scope of astronomical surveys has allowed many studies into the anisotropy of sources over the past 20 years. In the 2002 investigation of Blake & Wall [88], the number counts of radio galaxies were analysed as a consistency check of the standard cosmological model. Particular attention is paid to the influence of a foreground 'clustering' dipole due to our local galactic superstructures. This presents as an anisotropic distribution of local galaxies that will contribute a significant dipole component to the overall dipole observed in the distant, isotropically distributed source population. The results of the analysis conclude that both the magnitude and direction of the number density dipole on the sky is consistent with that derived from the observed

CMB dipole. From this, they confirm that the standard cosmological model used to interpret the CMB is valid, with sources at $z \sim 1$ thus coinciding with the cosmic rest frame.

However, a later reanalysis of Blake & Wall performed by Singal [89] determined a velocity dipole amplitude of $\sim 1600 \pm 400\,\mathrm{km\,s^{-1}}$, which is approximately four times larger than the CMB expectation and double that originally reported by Blake & Wall. Despite this significant disagreement in the magnitude of the dipole, its alignment remains consistent with the direction of the CMB dipole. Furthermore, it was found that such results could not be randomly re-obtained at a $> 99\%$ confidence level.

There have been numerous other studies involving cosmic dipoles published over the past decade [90–94]. During the writing of this thesis, there were several papers on the subject of cosmic dipoles released – and a few of which garnered particular attention regarding the ongoing Hubble tension. Published in late-2020, the investigation of Secrest *et al.* [95] used an all-sky sample of 1.3 million WISE quasars to reject an exclusively kinematic CMB dipole hypothesis at the 3.9σ level. They determine a dipole amplitude of $D_1 = 0.0173$, twice the CMB expectation, in the direction $(l, b) = (234.1°, 29.2°)$.[6] This is only 29.8° from the Planck (2018) location of the CMB dipole at $(l, b) = (264.021°, 48.253°)$. Given that the mean redshift of the sample is $z = 1.2$, this result suggests that the effects contributing to the dipole extend well beyond those of local effects.

Another important paper released in late-2020 was the cosmic radio dipole investigation of Siewert *et al.* [97]. Based on detailed statistical analyses of the TGSS-ADR1, WENSS, SUMSS and NVSS radio source catalogues, they find that the dipole amplitudes across all four surveys are greater than expected based on the CMB dipole. In particular, the dipole amplitudes they determine for NVSS agree with the results of Singal [89], Rubart & Schwarz [90], Bengaly *et al.* [93] and Tiwari & Nusser [98]. Additionally, they describe an overall increasing dipole amplitude with decreasing frequency, which is in line with literature expectations. However, they note that a purely kinematic contribution to the dipole is unlikely given its frequency dependence.

Overall, these significant observations of cosmic dipoles, in tandem with bulk flow

---

[6] However, a recent argument has been put forward by Dalang & Bonvin [96] regarding the generally neglected redshift evolution of the sources. In a re-analysis of Secrest *et al.* [95], they suggest that the tension can be reduced drastically by modifying the number count framework of Ellis & Baldwin [87] for a suitably defined source evolution.

measurements, are driving factors in the potential rejection of the purely kinematic dipole hypothesis.

1.4 Variations in the Hubble Expansion

Rather than assuming that a single uniform expansion rate applies in all observable directions, one can instead measure directional variations in the expansion rate from a sample of objects with sufficient sky coverage. By combining and extending the angular averaging techniques established by McClure & Dyer [99], and the radial spherical averages investigated by Li & Schwarz [100] for the Hubble Space Telescope Key data set, Wiltshire *et al.* [4] performed an analysis of the angular and radial variation of the local expansion on $\lesssim 150\,h^{-1}$ Mpc scales using the COMPOSITE dataset [82, 83].

While the HST Key dataset contained a large fraction of supernovae distances, which are more precise than other distance indicators, it contained a total of only 76 data points, which meant that the sky coverage was low and the statistical confidence of the conclusions of refs. [99, 100] was not high. Although the COMPOSITE sample contains many distances with larger uncertainties of up to 10%, the sheer size of the sample – 4534 galaxy distances and redshifts – allows for significantly greater statistical confidence. Importantly, it enables one to reliably perform analyses of the variation of expansion by averaging in independent radial shells as well as with angular window functions.

1.4.1 Minimum Spherically Averaged Hubble Variation

Making no other cosmological model assumptions other than that a suitably defined average linear Hubble law exists, Wiltshire *et al.* [4] firstly investigated the spherically averaged patterns of Hubble flow variation of the COMPOSITE dataset in the frames of the CMB, local group (LG) and the 'local sheet' (LS) of galaxies [81]. While Li & Schwarz [100] only had sufficient data to split the sample into inner and outer radial shells, Wiltshire *et al.* [4] extended their method to determine the best fitting linear Hubble law in successive independent radial shells s, by minimising the sum,

$$\chi_s^2 = \sum_i^{N_s} \left[{\sigma_i}^{-1}(r_i - cz_i/H)\right]^2 , \tag{1.52}$$

with respect to H by a standard linear regression, where z_i and r_i denote the redshift and luminosity distance of each data point, and N_s is the number of COMPOSITE data points contained within the shell, s. Each shell subsequently has a different best fit Hubble constant H_s, which is given by

$$H_s = \left(\sum_{i=1}^{N_s} \frac{(cz_i)^2}{\sigma_i{}^2} \right) \left(\sum_{i=1}^{N_s} \frac{cz_i r_i}{\sigma_i{}^2} \right)^{-1} , \tag{1.53}$$

where σ_i is the individual distance uncertainty of the i-th data point.

By characterising the relative variation

$$\delta H_s = \big(H_s - \bar{H}_0 \big) / \bar{H}_0 \,, \tag{1.54}$$

of each H_s to the global asymptotic value $\bar{H}_0$, Wiltshire *et al.* [4] found that the variation of the spherically averaged Hubble flow in the Local Group (LG) frame is less than that found in the CMB frame, $\Sigma_s |\delta H_{\rm s,LG}| < \Sigma_s |\delta H_{\rm s,CMB}|$, with very strong Bayesian evidence. This result was a surprise given the common intuition that the CMB frame should coincide with the frame of the cosmic standard of rest, and should therefore naïvely be a frame of minimal statistical variation in the Hubble expansion.

Wiltshire *et al.* [4] found an explanation for this surprising result by considering the difference $\Delta H_s = H_{\rm s,CMB} - H_{\rm s,LG}$, where the subscripts CMB and LG refer to (1.53) evaluated in the CMB and Local Group frames, respectively. They observed that the values of ΔH_s for each shell were roughly inversely proportional to the average value of their squared luminosity distances $\langle r_i^2 \rangle_s$. This can be understood if the Local Group frame is close to one in which the variation of the spherically averaged Hubble expansion is minimised. Suppose we have an ideal frame in which this is true, with an ideal dataset of redshifts z_i that are uniformly distributed over the sky. If the central observer then performs an arbitrary local boost, each z_i will be replaced with z_i', as given by (1.40). In the Newtonian velocity addition approximation, neglecting the $\mathcal{O}(\beta)$ terms, this results in the changes $(cz_i)^2 \to (cz_i')^2 = (cz_i)^2 + 2cz_i\,\boldsymbol{v}\cdot\hat{\boldsymbol{n}}_i + (\boldsymbol{v}\cdot\hat{\boldsymbol{n}}_i)^2$ in the numerator of (1.53), as well as $cz_i r_i \to cz_i r_i + r_i\,\boldsymbol{v}\cdot\hat{\boldsymbol{n}}_i$ in the denominator. For data uniformly distributed over the sky, the linear terms in (1.53) are self-cancelling: adding a boost velocity to data on one side of the sky leads to a subtraction of a boost of the same magnitude on the opposite side of the sky. To leading order we then have

$$\begin{aligned} \Delta H_s = H_s' - H_s &\sim \left(\sum_{i=1}^{N_s} \frac{(\boldsymbol{v}\cdot\hat{\boldsymbol{n}}_i)^2}{\sigma_i^2} \right) \left(\sum_{i=1}^{N_s} \frac{cz_i r_i}{\sigma_i^2} \right)^{-1} \\ &\approx \frac{v^2}{3\bar{H}_0 \, \langle r_i^2 \rangle_s} \,. \end{aligned} \tag{1.55}$$

The COMPOSITE sample does not fully cover the sky. As with other galaxy surveys it lacks data in the plane of the Milky Way galaxy, the so-called 'Zone of Avoidance', where the Milky Way obscures distant galaxies[7]. However, since the Zone of Avoidance is symmetrical on the sky, the arguments leading to (1.55) still apply. Wiltshire *et al.* [73] verified the relation (1.55) for $\Delta H_s = H_{\text{s,CMB}} - H_{\text{s,LG}}$, apart from shells in a small range of distances $40 \lesssim d_L \lesssim 60\,h^{-1}$ Mpc, in which the average values of H_s in the CMB frame are closer to the asymptotic Hubble constant than in the LG frame: $|\delta H_{\text{s,CMB}}| < |\delta H_{\text{s,LG}}|$ in (1.54). As such, the boost to the CMB frame appears to be compensating for structures in this range – the most prominent being the Great Attractor.

McKay & Wiltshire [101] subsequently undertook a systematic investigation of arbitrary boosts of the central observer to determine the frame in which the spherically averaged Hubble expansion variation was minimised for the COMPOSITE sample via (1.55). While they confirmed the result of Wiltshire *et al.* [73] for the difference between the CMB and LG frames, they also found that one can perform boosts of order 100 – 200 $\mathrm{km\,s^{-1}}$ in the plane of the Milky Way without changing the statistical likelihood of the fit to (1.55) [101]. The absence of data in the Zone of Avoidance appears to be responsible for this degeneracy. Consequently, while one cannot conclusively say that the LG frame is the one in which the spherically averaged Hubble expansion is minimised, it appears to be included in a degenerate set of such frames. McKay & Wiltshire also investigated the *Cosmicflows-II* sample [102] of 8162 redshifts and distances, finding consistent results. However, *Cosmicflows-II* has an unsubtracted distribution Malmquist bias – corresponding to a monopole in H_0 which limits its usefulness. One can only perform differential comparisons for which the monopole systematic cancels, but this adds to the uncertainties.

In the standard cosmology, the relation (1.55) is found well within the 'non-linear regime' of structure formation, which is typically treated with Newtonian N-body simulations. Consequently, a simple relation of the form (1.55) was unexpected. Nonetheless, some researchers did find explanations in terms of N-body simulations with large bulk flows [103–106]. In particular, Kraljic & Sarkar noted that if there is an additional bulk flow $\boldsymbol{v}_{\text{bulk}}$ in the frame in which the spherically averaged Hubble expansion is minimised,

---

[7] See section 3.3.2 for a more in-depth discussion of the COMPOSITE dataset.

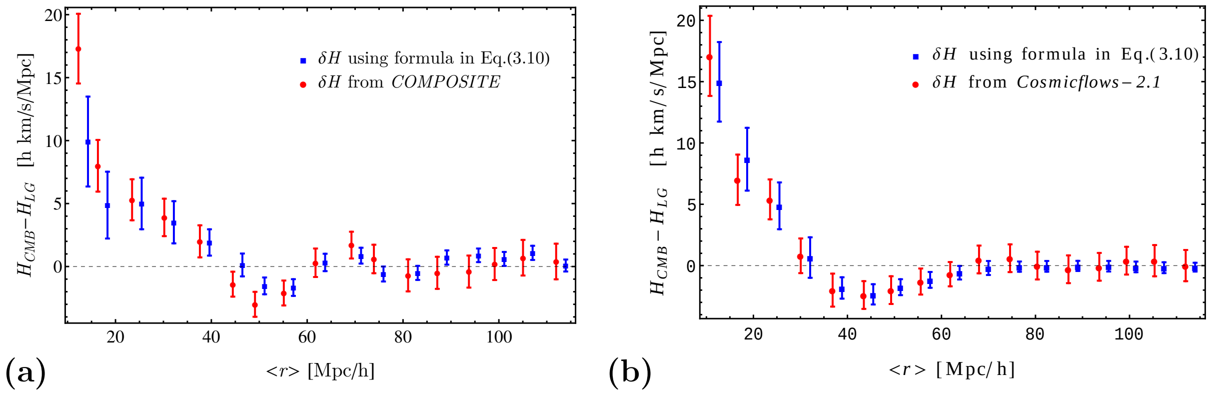

Figure 1.5: Difference of the spherically averaged Hubble constant in independent radial shells, as evaluated in the CMB and LG frames respectively. **(a)** Comparison of COMPOSITE data [82, 83] to (1.56); **(b)** Comparison of *Cosmicflows-II* data [102] to (1.56). Note that equation (3.10) in [103] is (1.56) here while their δH_s is our ΔH_s. Image credit: Kraljic & Sarkar (2016) [103].

then by similar arguments (1.55) is replaced by

$$\Delta H_s = H_s' - H_s \approx \frac{1}{H_0 \left\langle r_i^2 \right\rangle_s} \left(\frac{1}{3} |\mathbf{v}|^2 - \frac{1}{3} 2\boldsymbol{v} \cdot \mathbf{v}_{\text{bulk}}(\langle r_i \rangle_s) \right) . \tag{1.56}$$

With this modification, they were able to find locations within N-body simulations for which one could not only fit the r^{-2} dependence of ΔH_s found by Wiltshire *et al.* [73], but also the deviation for shells in the range $40 \lesssim d_L \lesssim 60\, h^{-1}$ Mpc as shown in fig. 1.5.

A framework in which the spherically averaged Hubble expansion is most uniform in the Local Group frame without large bulk flows is consistent with non-kinematic differential expansion on $\lesssim 100\, h^{-1}$ Mpc scales. Nonetheless, the result of Kraljic & Sarkar shows that more detailed observational campaigns will be required to distinguish the two hypotheses. The likelihood of large bulk flows is yet to be determined in the ΛCDM framework, and cannot be separated from the question of selection effects and statistical biases in current datasets.

The investigations of Bolejko *et al.* [1], which form the starting point for this thesis, build on the work of Wiltshire *et al.* [4] by asking whether the local Hubble expansion found for the COMPOSITE dataset can be replicated in general relativistic models of local expansion on $\lesssim 150\, h^{-1}$ Mpc scales.

1.4.2 Non-Kinematic Differential Expansion

If the redshift of an observation is not adequately described by (1.13), there are evidently non-kinematic contributions present. Whether these contributions are due to physical causes or due to an unaccounted for observational bias, it is important to ascertain to what extent they modify the observed redshift.

This thesis is principally built upon the investigation of Bolejko *et al.* [1], which sought to characterise the effects of a non-kinematic differential expansion of space due to local inhomogeneities. They proposed that the non-kinematic redshift contributions entering into (1.13) create an anisotropic variation in the observed Hubble expansion, in accordance with the findings of Wiltshire *et al.* [4]. To explore this, they use exact inhomogeneous solutions of the Einstein equations to produce toy models of the nearby universe up to $\sim 100\,h^{-1}\,\mathrm{Mpc}$.

It is necessary to define canonical choices of the CMB *rest frame* and our local Lorentz frame, in order to specify the factor of $(1+z)_{\mathrm{FLRW}}$ in (1.13). The canonical CMB rest frame is defined by matching our observed $1.23 \times 10^{-3}\,T_0$ CMB temperature dipole in the heliocentric frame to the dipole of the following series expansion,

$$\frac{T_0}{\gamma_{\mathrm{CMB}}(1-\beta_{\mathrm{CMB}}\cos\theta)} = T_0\left[1+\beta_{\mathrm{CMB}}\cos\theta+\beta_{\mathrm{CMB}}^2\left(\cos^2\theta-\frac{1}{2}\right)+\dots\right] \tag{1.57}$$

where $\beta_{\mathrm{CMB}}\cos\theta \equiv \boldsymbol{\beta}_{\mathrm{CMB}}\cdot\hat{\boldsymbol{n}}_{\mathrm{hel}}$. Within the heliocentric frame, $\hat{\boldsymbol{n}}_{\mathrm{hel}}$ is the unit vector on the sky, $\boldsymbol{\beta}_{\mathrm{CMB}} = \boldsymbol{v}_{\mathrm{CMB}}/c$ is the boost vector of the CMB frame and $\gamma_{\mathrm{CMB}} = (1-\beta_{\mathrm{CMB}}^2)^{-1/2}$ is the standard Lorentz gamma factor.

We can then define the frame of local *average isotropic expansion* (AIE) to be the Lorentz frame at our location in which the spherically averaged redshift-distance relation of independent radial shells varies minimally with respect to a linear Hubble law. In doing so, one should find that the redshift of an observed source will feature a non-kinematic anisotropy with a dependence $z(\hat{\boldsymbol{n}}_{\mathrm{AIE}})$, where $\hat{\boldsymbol{n}}_{\mathrm{AIE}}$ is the unit vector on the sky in the AIE frame. This causes a departure of the source redshift from the description given by (1.13), such that performing a boost from the AIE frame to the heliocentric frame should yeild a non-negligible difference in the amplitude of the CMB dipole.

To formally describe the variation in the CMB dipole due to variations in the local Hubble expansion rate, we can define *general relativistic non-kinematic differential expansion* or *relativistic differential expansion* to be present when the difference

$$\Delta T_{\mathrm{nk-hel}} = \frac{T_{\mathrm{AIE}}}{\gamma_{\mathrm{AIE}}(1-\boldsymbol{\beta}_{\mathrm{AIE}}\cdot\hat{\boldsymbol{n}}_{\mathrm{hel}})} - \frac{T_0}{\gamma_{\mathrm{CMB}}(1-\boldsymbol{\beta}_{\mathrm{CMB}})} \tag{1.58}$$

has a significant non-zero dipole when expanded over the sky in spherical harmonics [1]. Similar to (1.57), $\boldsymbol{\beta}_{\mathrm{AIE}} = \boldsymbol{v}_{\mathrm{AIE}}/c$ is the boost of the AIE frame in the heliocentric frame,

$\gamma_{\mathrm{AIE}} = (1 - \beta_{\mathrm{AIE}}^2)^{-1/2}$ and

$$T_{\mathrm{AIE}}(\boldsymbol{n}_{\mathrm{AIE}}) = \frac{T_{\mathrm{CMB}}}{1 + z_{\mathrm{AIE}}(\hat{\boldsymbol{n}}_{\mathrm{AIE}})} \tag{1.59}$$

is the anisotropic temperature of the CMB as measured in the AIE frame. Here, $T_{\mathrm{CMB}} = (1 + z_{\mathrm{dec}})T_0$ is the mean intrinsic temperature of the CMB at recombination and z_{dec} is the constant isotropic redshift of recombination within the FLRW model.

1.5 Summary of Research

The primary aim of this thesis is to perform a reanalysis of the results of Bolejko *et al.* [1], with corrections made for incorrect calculations perfomed within the simulation. Unfortunately, the original ray tracing routines utilised in Bolejko *et al.* [1] contain an erroneous initialisation procedure for the setup of individual null geodesics. This meant that each light ray was propagated in an incorrectly determined direction, which was expected to influence the overall dipole and quadrupole in the Hubble flow variation. The error was first discovered during the investigation of Dam [107], who subsequently developed a correction for the affected routine in their master's thesis. However, until the work of this present thesis, the correction had yet to be implemented for the results of Bolejko *et al.* [1].

In **Chapter 2**, we give an overview of the two inhomogeneous cosmological models of interest to our investigation. The first of these is the Lemaître-Tolman-Bondi model; a radially inhomogeneous solution of the Einstein equations that has been used extensively in the past for modelling cosmic voids. It is also a spherically symmetric generalisation of the second model presented in the overview, the Szekeres model, which is central to our ray tracing analyses.

In **Chapter 3**, the methodology of our simulations is described in terms of the formalisms and computational schemes involved. The specifications of our particular Szekeres model will be discussed and the details of the ray tracing procedure will be elaborated upon.

Finally, in **Chapter 4**, the results of our ray tracing simulations will be presented in comparison to the results of Bolejko *et al.* [1]. We also examine the variation of the results for changes in the observer position, as well as under small Haantjes transformations applied to the Szekeres model.

Chapter 2

Inhomogeneous Cosmological Models

On large scales, inhomogeneities in the standard cosmology are often modelled using linear perturbation theory on an FLRW background, even at late times. On scales much less than $100\,h^{-1}$ Mpc, where non-linear structures begin to dominate, we move towards different methods of cosmological modelling. The growth of non-linear structures, such as cosmic voids and walls, involve significant density contrasts that restrict the use of early-time perturbative approaches. Instead, the study of late-time structure formation is often tasked to complex Newtonian N-Body simulations. However, these simulations are unable to capture relativistic effects at a scale where they should be significant. The coupling of matter and geometry is simply neglected. It is thus of considerable benefit to incorporate fully relativistic methods into studies of structure formation on small scales.

A promising approach to modelling the local universe is through inhomogeneous cosmological models with an effective fluid (often dust) energy-momentum tensor. Such models are well suited for describing structure arising from non-linear regimes. They are built upon exact solutions of Einstein's equations, with initial conditions specified as functions of the metric. The two models of interest to our investigation are the Lemaître-Tolman-Bondi (LTB) and Szekeres solutions, with parameters adapted to approach the FLRW model asymptotically beyond a $\sim 100\,h^{-1}$ Mpc scale of statistical homogeneity. In the following section, an overview of both models will be presented. However, it is the Szekeres model that we shall be using extensively in our ray tracing simulations. The LTB model is contained within the Szekeres model as a spherically symmetric limit, so it is presented in what follows as an important preliminary.

In this chapter, unless otherwise stated, we will use natural units in which $G = 1$ and $c = 1$.

2.1 The Lemaître-Tolman-Bondi Model

The LTB model is an exact solution of Einstein's equations for a spherically symmetric geometry containing only a pressureless, irrotational dust. It was first presented in the 1933 paper of Lemaître [108], wherein the stability of general relativistic models was assessed for collapsing matter condensations. Einstein models exhibiting anisotropies were shown to depart from equilibrium and undergo a contraction catalysed by the anisotropy. Further examination of this unstable behaviour was later performed by Tolman in 1934 [109][1]. More recently, the LTB solutions are frequently applied as toy models for an inhomogeneous universe. A unique feature of these models is the lack of a preferred symmetry centre, which explicitly breaks the Copernican principle. While this renders the model unrealistic in providing a complete description of our universe, it nonetheless has relativistic features that FLRW models do not. A particular example of such occurs for observers located in vast cosmic voids. The observers witness an apparent acceleration of cosmic expansion, even though the expansion is locally decelerating everywhere else. A basic feature of inhomogeneous models is that regions of varying local density will undergo expansions with decelerations that are position-dependent. This further complicates the notion of an average deceleration across all lines of sight. Despite the ability of the LTB model to explain perceived accelerated expansion and other cosmological observations, the scale of voids it requires are not observationally supported. Our interest here will be in the modelling of smaller inhomogeneities, on scales $\leq 100\,h^{-1}\,\mathrm{Mpc}$, in the regime where all astronomers agree that inhomogeneities are large.

2.1.1 The LTB Metric

Any general spherically symmetric metric can be written in the form

$$\begin{aligned} \mathrm{d}s^2 &= g_{\mu\nu}\,\mathrm{d}x^\mu\,\mathrm{d}x^\nu \\ &= -\mathrm{e}^{C(t,r)}\,\mathrm{d}t^2 + \mathrm{e}^{A(t,r)}\,\mathrm{d}r^2 + R^2(t,r)(\mathrm{d}\theta^2 + \sin^2\theta\,\mathrm{d}\phi^2)\,, \end{aligned} \tag{2.1}$$

---

[1] Bondi performed a reanalysis of this solution over a decade later [110] with an elegant analysis of geodesics on the background. The referring to of these solutions as the Lemaître-Tolman, Tolman-Bondi or Lemaître-Tolman-Bondi solutions varies in the literature.

where $C(t,r)$, $A(t,r)$ and $R(t,r)$ are determined through the appropriate Einstein field equations. The LTB dust source has the energy momentum tensor

$$T^{\mu\nu} = \rho\, u^{\mu}\, u^{\nu}\,, \tag{2.2}$$

where u^{μ} are the 4-velocities of a congruence of 'dust particles' and $\rho = \rho(t,r)$ is spherically symmetric density with respect to a centrally located observer in the congruence. If we assume that the coordinates are comoving with the dust, but with a generic time coordinate, then the 4-velocity of the dust congruence must be

$$u^{\mu} = e^{-C/2}\delta^{\mu}_{t} = e^{C/2}(1,0,0,0)\,. \tag{2.3}$$

Due to the spherical symmetry of the metric, the dust will flow only along the radial coordinate extending from the model's centre, with the particles remaining at fixed spatial coordinates (r,θ,ϕ). Because of this, we have $\mathrm{d}r = \mathrm{d}\theta = \mathrm{d}\phi = 0$, so that the coordinate time t is related to the proper time τ of the dust by $\mathrm{d}\tau = e^{C/2}\,\mathrm{d}t$. We can further observe that these properties emerge from the equations of energy-momentum conservation for a perfect fluid ${T^{\mu\nu}}_{;\nu} = 0$. Without a pressure contribution, these equations reduce to $u^{\nu}\nabla_{\nu}u^{\mu} = 0$, which is identically the condition for defining geodesics under an affine parametrisation. The proper time τ will then correspond to the affine parameter, and the dust particles will travel along these geodesics.

If we further choose $C = 0$ or $\tau = t$, then the coordinates are also synchronous. Such a choice is possible globally in the absence of vorticity, so long as the dust geodesics do not cross. The Einstein field equations for the metric (2.1) with a dust source are then,

$$G_{\hat{t}\hat{t}} = \mathrm{e}^{-C}\left(\frac{\dot{R}^2}{R^2}+\frac{\dot{A}\dot{R}}{R}\right) - \mathrm{e}^{-A}\left(2\frac{R''}{R}+\frac{R'^2}{R^2}-\frac{A'R'}{R}\right)+\frac{1}{R^2}$$

$$= \kappa\rho + \Lambda \ , \tag{2.4}$$

$$G_{\hat{r}\hat{r}} = -\mathrm{e}^{-C}\left(2\frac{\ddot{R}}{R}+\frac{\dot{R}^2}{R^2}-\frac{\dot{C}\dot{R}}{R}\right) + \mathrm{e}^{-A}\left(\frac{R'^2}{R^2}+\frac{C'R'}{R}\right)-\frac{1}{R^2}$$

$$= \kappa P - \Lambda \ , \tag{2.5}$$

$$G_{\hat{\theta}\hat{\theta}} = -\frac{\mathrm{e}^{-C}}{4}\left(4\frac{\ddot{R}}{R}-2\frac{\dot{C}\dot{R}}{R}+2\frac{\dot{A}\dot{R}}{R}+2\ddot{A}+\dot{A}^2-\dot{C}\dot{A}\right)$$

$$+\frac{\mathrm{e}^{-A}}{4}\left(4\frac{R''}{R}+2\frac{C'R'}{R}-2\frac{A'R'}{R}+2C''+C'^2-C'A'\right)$$

$$= \kappa P - \Lambda \ , \tag{2.6}$$

$$G_{\hat{t}\hat{r}} = \mathrm{e}^{-A}\left(\frac{\dot{A}R'}{R}+\frac{\dot{R}C'}{R}-2\frac{\dot{R}'}{R}\right) = 0 \ , \tag{2.7}$$

where primes denote partial derivatives with respect to r and over-dots denote partial derivatives with respect to t. With our choice of synchronous coordinates $C = 0$ and equation (2.7) becomes

$$\frac{\partial}{\partial t}\left(\mathrm{e}^{-A/2}R'\right) = 0 \ . \tag{2.8}$$

This, in turn, may be integrated over time for $R' \neq 0$ to obtain

$$\mathrm{e}^{A} = \frac{R'^2}{1+2E(r)} \ , \tag{2.9}$$

where the arbitrary function $E(r)$ arises from the integration. Finally, by using this result (2.9) and setting both $P = 0$ and $C = 0$ for equation (2.5) we can eliminate R'^2 so that

$$2\frac{\ddot{R}}{R}+\frac{\dot{R}^2}{R^2}-\frac{2E}{R^2}-\Lambda = 0 \ . \tag{2.10}$$

Multiplying equation (2.10) by $R^2\dot{R}$ and assuming $\dot{R} \neq 0$ we then obtain an equation that may be integrated to give

$$\dot{R}^2 = 2E(r) + \frac{2M(r)}{R} + \frac{1}{3}\Lambda R^2 \ , \tag{2.11}$$

where $M(r)$ is another arbitrary function of integration. This key equation defines the evolution of R given the functions $M(r)$, $E(r)$ and the cosmological constant term Λ. Here, the function $E(r)$ corresponds to the spatial curvature of the constant-t hypersurface, which may also be regarded as the energy per unit mass of the dust. In order to maintain the correct signature of the metric, it is required that $E \geq -1/2$ for all r. Additionally, in the case that $E = -1/2$, which requires $\dot{R} = 0$ at the given r, there will exist a neck or wormhole [111]. The other arbitrary function $M(r)$ describes the *active gravitational mass* within a constant-r shell, which is responsible for generating the gravitational field. This is distinct from the integrated masses of all dust particles which comprise the matter content of the model N, as is described in [110]. The difference between N and M when $M < N$ is known as the relativistic mass defect, which determines whether the system is either bound, unbound, or 'marginally' bound according to whether $E < 0$, $E > 0$ or $E = 0$ respectively. This can be further shown by considering the integrated mass of all dust particles over the volume of interest, as

$$\begin{aligned} N(r) &= \int_V \rho(t,r)\sqrt{{}^3g}\,\mathrm{d}^3x \\ &= 4\pi \int_0^r \rho \frac{R^2 R'}{\sqrt{1+2E}}\,\mathrm{d}\tilde{r} = \int_0^r \frac{M'(\tilde{r})}{\sqrt{1+2E(\tilde{r})}}\,\mathrm{d}\tilde{r}\ . \end{aligned} \tag{2.12}$$

Note that $N(r)$ varies from $M(r)$ by a factor of $\sqrt{1+2E(r)}$ [111].

By rearranging equation (2.11), we obtain another integral in terms of the arbitrary function $t_B(r)$ as follows:

$$t - t_B(r) = \int_0^R \frac{\mathrm{d}\tilde{R}}{\sqrt{2E + 2M/\tilde{R} + \frac{1}{3}\Lambda\tilde{R}^2}}\ . \tag{2.13}$$

The function $t_B(r)$ is denoted the 'bang time' at a given r, and allows the big bang within the model to vary with position. Since each shell evolves independently of its neighbours, they may individually emerge from the big bang singularity at different times, according to when $R(t_B(r), r) = 0$ for each [112]. This gives rise to the possibility of a non-simultaneous big bang, which contrasts with the FLRW model, wherein the whole of space emerges from the big bang singularity at a singular instant. For particular values of Λ, the big bang may instead never occur, a feature that is also present in Friedmann models.

With $C = 0$, equation (2.4) may be expressed through equations (2.8) and (2.10) as

$$\kappa\rho(t,r) = 8\pi\,\rho(t,r) = \frac{2M'}{R^2 R'}\ , \tag{2.14}$$

which describes the time-dependent energy density of the model.

Finally, through setting $C = 0$ and by substituting in equation (2.9) the LTB metric (2.1) becomes

$$\mathrm{d}s^2 = -\,\mathrm{d}t^2 + \frac{R'^2}{1+2E(R)}\,\mathrm{d}r^2 + R^2(t,r)\left(\mathrm{d}\theta^2 + \sin^2\theta\,\mathrm{d}\phi^2\right)\ , \tag{2.15}$$

where one must solve evolution equation (2.11) to obtain $R(t,r)$. Solutions to equation (2.11) must generally be found using numerical methods unless $\Lambda = 0$.

2.1.2 Solutions to the Evolution Equations for $\Lambda = 0$

When $\Lambda = 0$ one can obtain the following parametric solutions of the evolution equation (2.11) for different values of $E(r)$:

- When $E < 0$ the evolution is *elliptic*:

$$\begin{aligned} R(t,r) &= \frac{M}{(-2E)}(1-\cos\eta)\,, \\ \eta - \sin\eta &= \frac{(-2E)^{3/2}}{M}(t - t_B(r))\,. \end{aligned} \tag{2.16}$$

- When $E = 0$ the evolution is *parabolic*:

$$R(t,r) = \left(\frac{9}{2}M\,(t - t_B(r))^2\right)^{1/3}\ . \tag{2.17}$$

- When $E > 0$ the evolution is *hyperbolic*:

$$\begin{aligned} R(t,r) &= \frac{M}{2E}(\cosh\eta - 1)\,, \\ \sinh\eta - \eta &= \frac{(2E)^{3/2}}{M}(t - t_B(r))\,. \end{aligned} \tag{2.18}$$

In all cases, $M \equiv M(r)$ and $E \equiv E(r)$ as above, while η is defined implicitly in terms of t and r in the elliptic and hyperbolic cases.

Concerning elliptic evolution there also exists a time t_C which corresponds to the 'big crunch' singularity of the collapsing universe. This is defined as

$$t_C(r) - t_B(r) = \frac{2\pi M}{(-2E)^{3/2}} = T(r) \tag{2.19}$$

where $T(r)$ is the lifetime of a given shell with coordinate position r.

2.1.3 Regularities & Regular Extrema

From examination of equation (2.14), it is apparent that the mass density $\rho(t, r)$ will approach infinity for positions where $R = 0 \neq M'$, as well as for positions where $R' \neq 0 \neq M'$. The former of these cases correspond to the big bang singularity $R(t_B, r) = 0$, and will necessarily occur when $\Lambda = 0$. However, in the latter case one can have the formation of regular extrema or shell crossing singularities, as $R' \to 0$ when the proper distance between two neighbouring shells becomes zero. As each shell is uniquely labelled by the radial comoving coordinate r, it is possible for shells of different comoving radii to cross, meaning that they are no longer uniquely specified.

If the density ρ remains finite at this point of crossing, with $R' = 0$, the shell surfaces are then regular extrema. At a shell crossing singularity the density instead diverges (in addition to the Kretschmann scalar $R_{\mu\nu\sigma\lambda}R^{\mu\nu\sigma\lambda}$), with its value becoming negative upon the other side provided the sign of R' also changes.

In a physical context where pressure is non-negligible, this curvature singularity may correspond to a zero pressure limit of an acoustic wave wherein the density is large but finite. Regions of high density should therefore give rise to pressure gradients which suppress the occurrence of such singularities. It is also the case that geodesic bundles entering the shell crossing singularity will fail to converge as they otherwise would at the big bang. The physical interpretation of this is that objects will not undergo compression when approaching the singularity.

2.1.4 The FLRW Limit of the LTB Model

In the above equations (2.14) and (2.15) there exists a coordinate freedom in r due to the equations being invariant under coordinate transformations of the form $r = f(\tilde{r})$. By judiciously selecting this transformation, it is possible to fix one of the three functions $M(r)$, $E(r)$ and $t_B(r)$ so that the remaining two are independent. We can then retrieve the Friedmann solutions analogous to solutions (2.16), (2.17) and (2.18) in the spatially homogeneous limit provided we select M as the radial coordinate such that

$$M(r) = M_0 r^3 \,, \qquad E(r) = -\frac{1}{2} k r^2 \,, \qquad t_B = const \,.$$

This characterises the dust solutions for a spatially homogeneous and isotropic FLRW universe, where one has $t_B = const$ and $E/M^{2/3} = const$. The familiar FLRW scale factor $a(t)$ then follows from $R(t, r) = a(t)r$. As the Friedmann models are thus contained within the LTB class under the specified limits, one can observe similarities in their characteristics. Owing to the similarities between the LTB metric and the FLRW metric in comoving coordinates, it is perhaps unsurprising that each LTB shell behaves as if individually defined by an FLRW metric, which evolves from its specific point of emergence at $t_B(r)$.

As the value of the function $E(r) = -kr^2$ describes the spatial curvature of constant-t hypersurfaces, it may also be shown to characterise the expansion of space-time. Setting k as a function of r such that $E(r) = -k(r)r^2 < 0$, one can arrive at an expansion law of the form $R(t, r) \simeq r(t - t_B(r))\sqrt{-k(r)}$ via the asymptotic open LTB solution as $t \to \infty$. As such, it is possible for one to create expansion laws based upon an appropriate choice of $k(r)$. It has been shown that the expansion law corresponding to $k(r) = -1/(1 + r^\alpha)$ for $\alpha < 2$ will induce an accelerated expansion for a centrally placed LTB observer [113]. While this solution violates the Copernican principle, it demonstrates the important principle that an apparently accelerated expansion may indeed arise in inhomogeneous solutions of general relativity without the need of a cosmological constant.

2.1.5 Formation of Structures & Voids

The LTB model is of particular interest in the study of inhomogeneous cosmological models, due to its utility in modelling the formation of both cosmic voids and structures. This is apparent in the early descriptions of the model, pertaining to the instability of the Einstein and Friedmann models to the growth of perturbations. Lemaître [114] first suggests the formation of extra-galactic structures (particularly regarding galaxies, then referred to as 'nebulae') through the condensation of matter via instability.

The work of Tolman [109] further provided an early description of the creation of voids by considering Friedmann models subject to initial perturbations described by the LTB model. This is characterised by a variation in the LTB density relative to that of the corresponding Friedmann background, by defining the relation $R_{\text{LTB}}(t_i, r) = rR_{\text{F}}(t_i)$ between the models [111]. Provided the initial densities of each model are different from each other and with the assumption of

$$\left.\frac{\dot{R}'}{R'}(t_i)\right|_{\text{LTB}} = \left.\frac{\dot{R}}{R}(t_i)\right|_{\text{F}} \,, \tag{2.20}$$

the LTB mass density (2.14) may be re-expressed as

$$\begin{aligned}\left[\frac{\partial^2}{\partial t^2}\ln\rho_{\text{LTB}}\right](t_i) &= \left[2\frac{\dot{R}^2}{R^2} - 2\frac{\ddot{R}}{R} + \frac{\dot{R}'^2}{R'^2} - \frac{\ddot{R}'}{R'}\right](t_i) \\ &= \left[2\frac{\dot{R}^2}{R^2} + \frac{\dot{R}'^2}{R'^2} + \frac{1}{2}\kappa\rho_{\text{LTB}} + \Lambda\right](t_i)\,, \end{aligned} \tag{2.21}$$

where the evolution equation (2.11) is used to reduce the expression to that of the last line.

A similar result applies to the background Friedmann density, namely

$$\left[\frac{\partial^2}{\partial t^2}\ln\rho_{\text{F}}\right](t_i) = \left[3\frac{\dot{R}^2}{R^2} + \frac{1}{2}\kappa\rho_{\text{F}} + \Lambda\right](t_i)\,. \tag{2.22}$$

Taking the difference of equations (2.14) and (2.22) we obtain

$$\frac{\partial^2}{\partial t^2}\left(\ln\rho_{\text{LTB}} - \ln\rho_{\text{F}}\right) = \frac{1}{2}\kappa\left(\rho_{\text{LTB}} - \rho_{\text{F}}\right)\,. \tag{2.23}$$

This result demonstrates that initial over-densities or under-densities of the LTB model, which are attributed to an initial perturbation with respect to the corresponding Friedmann background, will evolve away from the background as time progresses. However, we note that over-dense regions will continue to increase in density unabated until the occurrence of singularities, including shell-crossings. Unfortunately, this behaviour arises due to the lack of pressure and rotation within the model, which would otherwise physically prevent such a collapse from occurring. An additional investigation by Sen [115] further supported these findings with an approach where the initial velocity is instead varied while the initial density remains unperturbed.

The evolution of voids and structures in both the Szekeres and LTB models are investigated in the monograph of Bolejko *et al.* [116], who consider the evolution of the Szekeres solution as compared to the corresponding LTB case. It is found that for large isolated voids, the evolution of the density contrast is considerably more rapid than it is for smaller voids bordered by high density regions. This corresponds to a greater expansion rate within the largest voids, combined with a growth of mass concentrations in high density regions located at the perimeter, facilitating the development of galactic walls and filaments. These elongated over-dense structures are also found to evolve at a much greater rate than that of more compact over-densities.

2.2 The Szekeres Model

The Szekeres cosmological model, which was first presented in the 1975 paper [117], provides a generalisation of the LTB model where the symmetries are relaxed to allow for more varied descriptions of inhomogeneity. Unlike the LTB model, it has no Killing vectors. Nonetheless, much like the LTB case, the Szekeres model contains only a pressureless irrotational dust source such that the metric describes shells of constant-r. However, these shells differ from LTB in that they are generally non-concentric. Mathematically, this is expressed via functions within the metric that characterise deviations from the symmetry of the equivalent LTB model. By specifying these functions, it is possible to model a dipole within the mass distribution on each shell, with the extent of this dipole controlled by the relative shifting and rotations between the shells. These combined characteristics make the Szekeres model an excellent means for modelling cosmic voids with an adjacent over-density, approximating a galactic cluster.

2.2.1 The Metric in Projective Coordinates

The parametrisation process required to obtain the Szekeres metric is more elaborate than that for the preceding LTB case. To begin, the metric is first defined in terms of synchronous comoving coordinates $u^\mu = \delta^\mu{}_t = (1, 0, 0, 0)$ for a perfect fluid dust source, and possible cosmological constant, as

$$\mathrm{d}s^2 = -\,\mathrm{d}t^2 + \mathrm{e}^{2\alpha}\,\mathrm{d}r^2 + \mathrm{e}^{2\beta}\left(\mathrm{d}p^2 + \mathrm{d}q^2\right) \,, \tag{2.24}$$

where $\alpha = \alpha(t, r, p, q)$ and $\beta = \beta(t, r, p, q)$ are functions to be defined and (p, q) label the 'projective coordinates'. These coordinates allow for a mapping of the Szekeres metric to spherical coordinates via a standard Riemann stereographic projection, as is further described in section 2.2.2. When defined in this manner, the metric is both comoving and synchronous by the same justifications that are given for the LTB case in Section 2.1. However, the Szekeres model is irrotational due to the vanishing vorticity $\omega_{\mu\nu} \equiv \nabla_{[\mu}u_{\nu]} = 0$. This also renders the model inadequate for virialised applications [111].

Maintaining the same description of the model originally presented within [117], the above metric (2.24) contains two arbitrary functions, $\alpha(t,r,p,q)$ and $\beta(t,r,p,q)$, which are determined by the solutions of the appropriate Einstein equations. To therefore derived the forms of the metric functions e^{α} and e^{β}, we follow the well described parametrisation choice presented in depth by [111]. The necessary components of the Einstein tensor $G_{\mu\nu}$ are also presented within [111].

For any perfect fluid source, the off-diagonal energy-momentum tensor components vanish, constraining the corresponding Einstein equations. For our dust fluid the G_{rr} field equation yields

$$\frac{\partial}{\partial t}\left(\mathrm{e}^{\beta-\alpha}\beta'\right) = 0\ , \tag{2.25}$$

where a prime denotes a partial derivative with respect to the r coordinate. Additionally, the $G_{rp} = G_{rq} = 0$ field equations are given by

$$\frac{\partial}{\partial p}\left(\mathrm{e}^{-\alpha}\beta'\right) = \frac{\partial}{\partial q}\left(\mathrm{e}^{-\alpha}\beta'\right) = 0\,, \tag{2.26}$$

so that β' can be then expressed as

$$\beta' = u(t,r)\mathrm{e}^{\alpha}\,. \tag{2.27}$$

The integral function $u(t,r)$ provides an important distinction between two subfamilies of solutions. These are the $\beta' = 0$ subfamily, including the homogeneous FLRW, Kantowski-Sachs and Datt-Ruban models, and the $\beta' \neq 0$ subfamily containing both the LTB and Szekeres models. As we are only concerned with the $\beta' \neq 0$ case in which $u(t,r) \neq 0$, equation (2.27) may be re-expressed as,

$$\frac{\partial}{\partial t}\left[\mathrm{e}^{\beta}u(t,r)\right] = 0\,, \tag{2.28}$$

which yields a solution of the form

$$\mathrm{e}^{\beta} = \frac{\mathrm{e}^{\nu(r,p,q)}}{u(t,r)} = \Phi(t,r)\,\mathrm{e}^{\nu(r,p,q)}\,, \tag{2.29}$$

where $\nu(r,p,q)$ is another arbitrary function to be determined. In seeking solutions to the remaining Einstein equations it is necessary to assume that

$$\frac{\partial}{\partial p}\left(\dot{\beta}\right) = \frac{\partial}{\partial q}\left(\dot{\beta}\right) = 0\,, \tag{2.30}$$

as otherwise no solutions are recovered. These conditions may then be applied to equation (2.27) to allow one to define e^{α} as

$$\mathrm{e}^{\alpha} = \Phi(t,r)\,\beta' = \Phi' + \Phi\nu' \,. \tag{2.31}$$

Finally, by incorporating equations (2.29) and (2.31) into the orthonormal frame field equation $G_{\hat{r}\hat{r}} = -\Lambda$ we obtain

$$\mathrm{e}^{-2\nu}\left(\frac{\partial^2\nu}{\partial p^2} + \frac{\partial^2\nu}{\partial q^2}\right) + 1 = 2\Phi\ddot{\Phi} + \dot{\Phi}^2 + \kappa\mathcal{P}\Phi^2 = -k(r)\,, \tag{2.32}$$

where $k(r)$ corresponds to the curvature parameter that was encountered in the LTB case, with the identification $k(r) = -2E(r)$. It is possible to simplify the left-hand-most side of this equation such that an expression for $\mathrm{e}^{-\nu}$ may be obtained in terms of arbitrary functions of r as follows

$$\mathrm{e}^{-\nu} = A(r)\left(p^2 + q^2\right) + 2B_1(r)\,p + 2B_2(r)\,q + C(r)\,. \tag{2.33}$$

However, these functions must necessarily be defined such that they satisfy

$$4\left(AC - {B_1}^2 - {B_2}^2\right) = 1 + k(r)\,, \tag{2.34}$$

in order to be consistent with equation (2.32).

As we have now obtained expressions (2.29), (2.31) and (2.33) the Szekeres metric defined by (2.24) is fully specified. However, for usability, it is typical to perform a further re-parametrisation in terms of additional arbitrary functions to render the metric more suitable for modelling purposes. This is achieved by defining a parameter ℓ such that

$$\ell = 1 + k(r) = 4\left(AC - {B_1}^2 - {B_2}^2\right)\ , \tag{2.35}$$

where the functions A, B_1 and B_2 are defined in terms of the arbitrary functions S, P and Q to be

$$A = \frac{\sqrt{|\ell|}}{2S}\,, \qquad B_1 = \frac{-\sqrt{|\ell|}P}{2S}\,, \qquad B_2 = \frac{-\sqrt{|\ell|}Q}{2S}\,. \tag{2.36}$$

Using these definitions within (2.35) and rearranging yields the following expression for the function C as follows:

$$C = \frac{\sqrt{|\ell|}S}{2}\left[\left(\frac{P+Q}{S}\right)^2 + \epsilon\right], \tag{2.37}$$

where by definition $\epsilon = \ell/|\ell|$. By substituting expressions (2.36) and (2.37) into (2.33) we obtain

$$\mathrm{e}^{-\nu} = \mathcal{E} = \frac{S}{2}\left[\left(\frac{p-P}{S}\right)^2 + \left(\frac{q-Q}{S}\right)^2 + \epsilon\right] \tag{2.38}$$

which further allows the functions $\mathrm{e}^{2\alpha}$ and $\mathrm{e}^{2\beta}$ to be re-parametrised using equations (2.31) and (2.29), respectively. In doing so, the function Φ is also redefined to be $\Phi = |\ell|R$, such that R matches that given in the LTB case. Completing this re-parametrisation for (2.24) produces the following form for the Szekeres metric in projective coordinates (p, q):

$$\mathrm{d}s^2 = -\,\mathrm{d}t^2 + \frac{(R' - R\mathcal{E}'/\mathcal{E})^2}{\epsilon - k}\,\mathrm{d}r^2 + \frac{R^2}{\mathcal{E}^2}(\mathrm{d}p^2 + \mathrm{d}q^2) \tag{2.39}$$

where primes continue to denote a partial derivative with respect to r. However, this coordinate r no longer corresponds to the radial distance from the origin, as the non-concentric arrangement of the shells will mean that their origins need not coincide. The parameter ϵ delineates three subtypes of the model. As we are solely interested in the quasi-spherical subtype, we will only consider the case where $\epsilon = +1$. Otherwise, ϵ may be set to 0 or -1, corresponding to the quasi-planar and quasi-pseudo-spherical subtypes respectively. The function $k = k(r)$ defines the local spatial curvature in the same fashion as it does within the LTB model. Again, the function $R = R(t, r)$ is the proper areal radius of a given shell, as it is within the LTB model.

An important component of the above Szekeres metric (2.39) is the function $\mathcal{E} = \mathcal{E}(r, p, q)$, which describes the deviation of the Szekeres model from the corresponding LTB model via equation (2.38). This expression contains three arbitrary functions $S(r)$, $P(r)$ and $Q(r)$, which characterise the dipole asymmetry within the model that varies with respect to r.

2.2.2 The Metric in Spherical Coordinates

In projective coordinates, the Szekeres metric (2.39) assumes a diagonal form which aids in the manipulation of the Riemann and Ricci tensors, as well as in specifying the geodesic equations. However, while this form is indeed simple and readable, it is somewhat less intuitive to work with for the purposes of modelling. Because of this, it is both useful

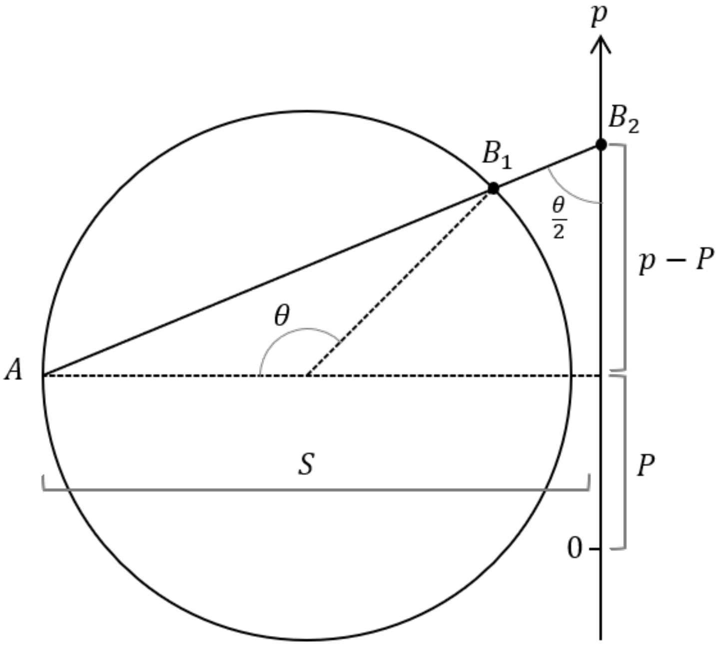

Figure 2.1: The two-dimensional cross-section of the Szekeres stereographic projection for $q = Q$. The line extending from the projection point at A intersects the sphere at a single point B_1 before it meets the projective plane at the point B_2. The projection point is shown to be displaced from the origin by distance P with a distance S from the projective plane.

and common to redefine the metric in terms of a Riemannian stereographic projection of the form

$$\begin{aligned} p - P &= S \cot\left(\frac{\theta}{2}\right) \cos\phi \\ q - Q &= S \cot\left(\frac{\theta}{2}\right) \sin\phi \end{aligned} \tag{2.40}$$

where (θ, ϕ) are spherical coordinates. The original (p, q) coordinates will map to a sphere through the proposed stereographic projection, such that the transformations will define the full p-q plane with $0 \leq \theta \leq \pi$ and $0 \leq \phi \; 2\pi$. This can be visualised through a 2D demonstration by considering lines extending from a projection point at the top of the sphere, which then intersect both the sphere and a 2D projection point at a single point per line. The projection plane is located at a distance $S(r)$ beneath the projection point, with an origin displaced by $(-P, -Q)$. The spherical coordinates (θ, ϕ) can be seen to relate to the projective coordinates, (p, q), as the point where $\theta = 0$ is simply the projection point where p and q would otherwise diverge. The location of the projection point may differ between shells, such that the top of one shell may point in a different direction to that of another. Additionally, due to the dependence of the functions S, P and Q on the coordinate r, the mapping of the projective coordinates may also differ from shell to shell.

As equation (2.38) is ill-defined when $S(r) = 0$, it is general to assume that $S(r) > 0$ when handling expressions dependent upon the dipole functions. The derivative of equation (2.38) with respect to r is then

$$\begin{aligned}\mathcal{E}'(r,p,q) =& \frac{1}{S}\left[(P-p)P' + (Q-q)Q'\right] \\ &- \frac{S'}{2S^2}\left[p^2 + q^2 - 2pP - 2qQ + P^2 + Q^2 - \epsilon S^2\right]\end{aligned} \tag{2.41}$$

By further setting $\mathcal{E}' = 0$ in the above equation (2.41) and rearranging, one can obtain the following equation for what will be a circle in the p-q projective plane

$$\left[p - \left(P - P'\frac{S}{S'}\right)\right]^2 + \left[q - \left(Q - Q'\frac{S}{S'}\right)\right]^2 = S^2\left(\frac{P'^2 + Q'^2}{S'^2} + \epsilon\right) \tag{2.42}$$

which is centred upon the point $(p_c, q_c) = (P - P'S/S', Q - Q'S/S')$ and has a radius of $L_c = S\sqrt{(P'^2 + Q'^2)/S'2 + \epsilon}$. This expression for $\mathcal{E}'$ is particularly informative, as it demonstrates the geometrical implications of $\mathcal{E}'/\mathcal{E}$ upon the g_{rr} component of the Szekeres metric. The circle described by equation (2.42) splits the p-q plane such that $\mathcal{E}' < 0$ within the circle, while $\mathcal{E}' > 0$ outside. As such, the locus (2.42) defines poles and zeros in the function of $\mathcal{E}'/\mathcal{E}$. Subsequently, the variations of p and q within $\mathcal{E}'/\mathcal{E}$ will influence the g_{rr} component, further causing p-q variations in the radial separation of neighbouring constant-r shells. The cumulative effect of this is the non-symmetric displacements of the shells relative to each other, which highlights an important geometrical distinction between the Szekeres and LTB models.

By defining the expressions (2.40) and substituting these into the Szekeres metric (2.39) it assumes the non-diagonal form:

$$\begin{aligned}\mathrm{d}s^2 =& -\mathrm{d}t^2 + \frac{1}{1-k}\left[R' - \frac{R}{S}(S'\cos\theta + N\sin\theta)\right]^2 \mathrm{d}r^2 \\ &+ \left[\frac{S'\sin\theta + N(1-\cos\theta)}{S}\right]^2 R^2\,\mathrm{d}r^2 \\ &+ \left[\frac{(\partial_\phi N)(1-\cos\theta)}{S}\right]^2 R^2\,\mathrm{d}r^2 - \frac{2[S'\sin\theta + N(1-\cos\theta)]}{S}R^2\,\mathrm{d}r\,\mathrm{d}\theta \\ &+ \frac{2(\partial_\phi N)\sin\theta(1-\cos\theta)}{S}R^2\,\mathrm{d}r\,\mathrm{d}\phi + R^2(\mathrm{d}\theta^2 + \sin^2\theta\,\mathrm{d}\phi^2)\end{aligned} \tag{2.43}$$

where $N(r,\phi) \equiv (P'\cos\phi + Q'\sin\phi)$ and ∂_ϕ denotes a partial derivative with respect to ϕ. Furthermore, the expression for $\mathcal{E}$ in projective coordinates simplifies in spherical coordinates to

$$\mathcal{E}(r,\theta,\phi) = \frac{S}{1-\cos\theta}$$

such that the expression for $\mathcal{E}'/\mathcal{E}$ becomes

$$\frac{\mathcal{E}'}{\mathcal{E}} = -\frac{S'\cos(\theta) + N\sin(\theta)}{S} \tag{2.44}$$

This makes the angular variation of the dipole functions apparent, as S' will vanish for certain values of θ while P' and Q' will vanish for certain values of ϕ. In the event that $P' = Q' = 0$, there will be no ϕ dependence in the function $\mathcal{E}'/\mathcal{E}$, which has been demonstrated to characterise the dipole distribution. Therefore, provided $S' \neq 0$, the model will be symmetric about the axis defined by S, with the dipole position only varying with the θ coordinate. This simple implementation of the Szekeres model is what is primarily investigated within this paper. Moreover, in the case where $S' = P' = Q' = 0$ it is readily seen that $\mathcal{E}'/\mathcal{E}$ will have no angular variation, such that there is an absence of dipolar structure and the metric reduces to the spherically symmetric form of the LTB model.

The full extent of the dipole function behaviour can be observed by defining 'local rectangular directions' for a given shell as

$$\hat{x} = \sin\theta\cos\phi\,, \qquad \hat{y} = \sin\theta\sin\phi\,, \qquad \hat{z} = \cos\theta\,, \tag{2.45}$$

so that

$$\frac{\mathcal{E}'}{\mathcal{E}} = \frac{-1}{S}\left(\hat{x}P' + \hat{y}Q' + \hat{z}S'\right)\,. \tag{2.46}$$

This further demonstrates that P'/S defines the anisotropy in the direction of $(\theta,\phi) = (\pi/2, 0)$, Q'/S in the direction of $(\theta,\phi) = (\pi/2,\pi/2)$ and S'/S in the direction of $\theta = 0$, which are the $\hat{x}$, $\hat{y}$ and $\hat{z}$ directions respectively.

2.2.3 The Density Dipole

The equation for the evolution of R can be obtained similarly to (2.11) by considering the left-hand portion of (2.32)

$$2R\ddot{R}^2 = -k(r) + \frac{2M(r)}{R} + \frac{1}{3}\Lambda R^2\,, \tag{2.47}$$

where the mass function $M(r)$ arises as a first integral and $-k(r) = 2E(r)$ as in the LTB case. Here we can see through the identical forms of (2.47) and (2.11) that the evolution of the constant-r is uninfluenced by the $S(r)$, $P(r)$, $Q(r)$ dipole functions of the Szekeres metric.

Although evolution-wise the Szekeres and LTB models are identical, the mass density of the Szekeres model will vary due to the presence of the dipole functions within $\mathcal{E}$. The Szekeres mass density is defined from the $G_{tt} = \kappa\rho = -1$ field equation as

$$\kappa\rho = \frac{2\left(M' - 3M\mathcal{E}'/\mathcal{E}\right)}{R^2\left(R' - R\mathcal{E}'/\mathcal{E}\right)} \tag{2.48}$$

with the $\mathcal{E}'/\mathcal{E}$ term defined by(2.44). We can then see that (2.48) reduces to the LTB density (2.14) when $S' = P' = Q' = 0$, as this means that $\mathcal{E}'/\mathcal{E} = 0$.

2.2.4 Shell Shifting & Rotation

Although Szekeres models have been studied for several decades, there are some geometrical aspects concerning the shifting and rotation of shells that have only been elucidated recently. Shell rotation in particular has recently been demonstrated to affect the cross-sectional visualisation of constant-t slices through a given model. While shell shifting has been reasonably well known over the past few years, a recent investigation by Hellaby [118] examined whether the spherical coordinates of the Szekeres metric under stereographic projection maintained their orientation on successive constant-r shells. This was further explored in excellent detail by Buckley and Schlegel [112], who demonstrated that neglecting the relative rotations and shifts of each shell produces a misleading representation of the geometry for a 2D cross-section. Because the extent of these effects has been unknown until recently, most visualisations of Szekeres models in previous papers are not entirely correct. Within this thesis, we shall apply the corrections suggested within Buckley and Schlegel's recent paper, such that the depictions of our model are portrayed accurately.

Shell Shifting

The Szekeres shell shifting effect arises due to the dipole functions within the g_{rr} term of (szek metric), which describes the minimum proper distance between shells at r and $r + \delta r$. Because these functions are responsible for the dipole distribution of the density through $\mathcal{E}'/\mathcal{E}$, a shell at $r + \delta r$ will be displaced relative to its neighbour at r:

- In the direction $(\theta, \phi) = (\pi/2, 0)$ by an angular distance:

$$\delta\hat{x} = \frac{RP'/S}{\sqrt{1-k}} \tag{2.49}$$

- In the direction $(\theta, \phi) = (\pi/2, \pi/2)$ by an angular distance:

$$\delta\hat{y} = \frac{RQ'/S}{\sqrt{1-k}} \tag{2.50}$$

- In the direction $(\theta, \phi) = (0, 0)$ by an angular distance:

$$\delta\hat{z} = \frac{RS'/S}{\sqrt{1-k}} \tag{2.51}$$

These shifts will result in the compaction of shell surfaces in the direction opposite that of the shifting, with the density increasing where the shells are closest. We can observe this behaviour in the density equation (2.48), wherein the mass function will vary with r so that the mass redistributes to form a dipole in the direction of the shift. As the density interior to the shell is not symmetric, it is necessary that the mass be distributed such that the shell expands spherically.

One can further characterise this density variation of the Szekeres model by considering two components: the effective average density ρ_{int} within a given shell and the corresponding LTB density ρ_{LTB}. If for a given shell we have $\rho_{\text{LTB}} > \rho_{\text{int}}$ or,

$$\left[\frac{M'}{4\pi R' R^2}\right]_{\text{LTB}} > \left[\frac{3M}{4\pi R^3}\right]_{\text{int}}, \tag{2.52}$$

then the density gradient will be largest at the point where the shells are compressed. The density contrast at this point will then approach positive or negative infinity according to whether the shell's density is over-dense or under-dense relative to the interior density, respectively. For there to exist an over-dense region within the shell, it is then necessary for the overall shell density to be greater than its average interior density. Finally, in the case that $\rho_{\text{LTB}} = \rho_{\text{int}}$, the density will remain uniform in the presence of shell shifting. Consequently, the dipole functions responsible for the shifting are incapable of producing inhomogeneities with an initially inhomogeneous background. Therefore, there must exist an inhomogeneity in the initial prescription of the model in order for a dipole asymmetry to develop.

Visualising the Shell Shifting & Rotation Effects

In order to track the rotation of a shell relative to its neighbour, we utilise a matrix $A(r)$ to store the cumulative rotations of all interior shells relative to each other. A given shell at $r + \delta r$ will hence be rotated relative to the shell at r by

$$A(r + \delta r) = R_y(\alpha)\, R_x(\beta)\, A(r)\,, \tag{2.53}$$

where $R_y(\alpha)$ and $R_x(\beta)$ are the y and x rotation matrices in the shell's LRF as follows

$$R_y(\alpha) = \begin{pmatrix} \cos\alpha & 0 & \sin\alpha \\ 0 & 1 & 0 \\ -\sin\alpha & 0 & \cos\alpha \end{pmatrix} \qquad R_x(\beta) = \begin{pmatrix} 1 & 0 & 0 \\ 0 & \cos\beta & -\sin\beta \\ 0 & \sin\beta & \cos\beta \end{pmatrix}\,. \tag{2.54}$$

As we have already determined, the shell at $r + \delta r$ will be rotated by $\delta r\, P'/S$ about the negative y-axis and by $\delta r\, Q'/S$ about the positive x-axis. Therefore, the rotation angles α and β correspond to

$$\alpha = \frac{P'}{S}\delta r \qquad \beta = -\frac{Q'}{S}\delta r\,. \tag{2.55}$$

Finally to obtain the relative shift of the $r+\delta r$ we append the directional shifts (2.49-2.51) modified by the rotation matrix $A(r)$ to the shift of the shell at r as follows

$$\Delta(t, r + \delta r) = \Delta(t, r) + \frac{R(t,r)}{\sqrt{1 - k(r)}}\, A^T(r) \begin{pmatrix} P'/S \\ Q'/S \\ S'/S \end{pmatrix}\,. \tag{2.56}$$

After systematically tracking the rotations and shifts of each shell, we can plot a 2D projection of the Szekeres model by applying them to its Cartesian coordinate representation $(X, Y, Z) = (R\hat{x}, R\hat{y}, R\hat{z})$. In order to do so, we must effectively neglect the curvature of the model by setting $k(r) = 0$ when calculating the shell shifting in (2.56). This will introduce a distortion effect in the plotting of each shell, where the distance between each shell of radius $R(t, r)$ will not be accurately depicted, depending on the true value of $k(r)$. However, plotting the shells in this manner gives an accurate representation of distances along each of their surfaces[2].

The Cartesian coordinates (X', Y', Z') that include the shell shifting and rotation effects can then be built from the shift (2.56) and rotation arrays (2.53) as follows:

$$\begin{pmatrix} X' \\ Y' \\ Z' \end{pmatrix} = R(t,r)\, A^T(r) \begin{pmatrix} \sin\theta\cos\phi \\ \sin\theta\sin\phi \\ \cos\theta \end{pmatrix} + \Delta(t,r)\,. \tag{2.57}$$

We will use the above procedure when visualising particular Szekeres models in subsequent chapters.

2.2.5 Haantjes Transformations

While producing an axially symmetric Szekeres model with only $S'(r) \neq 0$ is relatively straightforward, one may wish to have more precise control over the positioning of the dipole through both $P'(r)$ and $Q'(r)$ while still maintaining the necessary conditions for axial symmetry. However, this would require the careful parametrisation of $P(r)$ and $Q(r)$ so that the projective coordinates hold constant along the symmetry axis. This is because the relative rotations of shells to each other (which are induced by having $P' \neq 0$ and/or $Q' \neq 0$) must be compensated for by changes in the relative shifting direction, in order for the symmetry axis to remain a straight line in the projective coordinates. Fortunately, there exists a series of convenient coordinate transformations, known together as a Haantjes transformation, which allow for the dipole to be repositioned in any arbitrary direction.

The Haantjes transformation can be considered as the result of three successive subtransformations, the first of which being a coordinate inversion across the $p^2 + q^2 = P^2 + Q^2 + S^2$ reflection plane (or the $P\sin\theta\cos\phi + Q\sin\theta\sin\phi + S\cos\theta = 0$ reflection plane in spherical coordinates). This transforms the projective coordinates as well as the

---

[2] There is an alternative method of plotting the shell shifts and rotations [112] that maintains the distances along lines of constant (p, q). However, this results in a distortion of the distances along each shell's surface, as well as a distortion of their radii.

dipole functions to

$$(\tilde{p},\, \tilde{q}) = \frac{(p,\, q)}{p^2 + q^2}\,, \qquad \left(\tilde{P},\, \tilde{Q},\, \tilde{S}\right) = \frac{(P,\, Q,\, S)}{P^2 + Q^2 + S^2}\,, \tag{2.58}$$

where over-tildes denote the transformed quantities. The next sub-transformation performed after the inversion is a constant coordinate translation of the form

$$(\tilde{p},\, \tilde{q}) = (p + p_0,\, q + q_0)\,, \tag{2.59}$$

$$\left(\tilde{P},\, \tilde{Q},\, \tilde{S}\right) = (P + p_0,\, Q + q_0,\, S)\,, \tag{2.60}$$

where the dipole functions must also be translated to maintain the form of the metric. As this simply corresponds to translating the origin point of the projective coordinates, it does not affect the spherical coordinate representation of the model. The final sub-transformation is another coordinate inversion of the form (2.58 across the now modified projection plane.

For a quasi-spherical Szekeres model in which $P' = Q' = 0$ initially, performing a Haantjes transformation will modify the (p, q) coordinates as follows:

$$\tilde{p} = \frac{p + D_1(p^2 + q^2)}{\tau}\,, \qquad \tilde{q} = \frac{q + D_2(p^2 + q^2)}{\tau}\,, \tag{2.61}$$

where τ is given by

$$\tau = 1 + 2D_1\, p + 2D_2\, q + \left({D_1}^2 + {D_2}^2\right)\left(p^2 + q^2\right)\,, \tag{2.62}$$

and both D_1 and D_2 are arbitrary constants. However, to maintain the model's physical relations and the form of the metric, the dipole functions must also be modified as follows:

$$\tilde{P} = \frac{P + D_1\,(P^2 + Q^2 + S^2)}{T}\,, \tag{2.63a}$$

$$\tilde{Q} = \frac{Q + D_2\,(P^2 + Q^2 + S^2)}{T}\,, \tag{2.63b}$$

$$\tilde{S} = \frac{S}{T} \tag{2.63c}$$

where T is given by

$$T = 1 + 2D_1\,P + 2D_2\,Q + \left({D_1}^2 + {D_2}^2\right)\left(P^2 + Q^2 + S^2\right). \tag{2.64}$$

Performing a Haantjes transformation of this form is especially convenient when constructing a complex, axially symmetric Szekeres model with $P' \neq 0 \neq Q'$. If one begins with a simple axially symmetric model with only $S' \neq 0$, such as the Szekeres model of Bolejko *et al.* [1], the dipole anisotropy can be arbitrarily repositioned without manually specifying the forms of P and Q. By specifying the constants D_1 and D_2 in terms of the desired angular position, the Haantjes transformation will automatically adjust the dipole functions to satisfy the axial symmetry requirements in the transformed model. The values of D_1 and D_2 required to transform the anisotropy to the position (ϑ, φ) as measured from the minimum value of the anisotropy r_l are

$$D_1 = \frac{1 - \cos\vartheta}{\sin\vartheta}\,\cos\varphi\, e^{-S(r_l)}\,, \tag{2.65a}$$

$$D_2 = \frac{1 - \cos\vartheta}{\sin\vartheta}\,\sin\varphi\, e^{-S(r_l)} \tag{2.65b}$$

Chapter 3

Model Setup & Initialisation

In the following chapter, we detail the construction of the Szekeres model that is implemented in our ray tracing simulations, including the ray tracing methodology that is involved. Using the foundational overview of the Szekeres model presented in the previous chapter, we construct an axially symmetric Szekeres model to simulate a local cosmic void with an adjacent over-dense structure. By then backwards propagating light rays through the model to both the simulated CMB and the COMPOSITE dataset (by numerically integrating the null geodesic equations), we can explore how the presence of local inhomogeneities influence the measurements made by an observer placed within the model. While in this thesis we adopt the same Szekeres model prescription as Bolejko *et al.* [1], hereafter referred to as BNW, we correct for an erroneous initialisation of the initial null vectors within the ray tracing routines. As a key part of our investigation, we will compare our corrected results with those of BNW to assess the effect they may have on their conclusions.

The FORTRAN90 programs used to perform the simulations within this thesis were originally developed by K. Bolejko [1] and L. H. Dam [107]. These programs also use the HEALPix libraries for FORTRAN90 to handle the manipulation of data on the spherical sky. Additional analysis, including data presentation and plotting, is achieved using a combination of Python and Mathematica.

3.1 The Density Profile

In order to produce our axially symmetric Szekeres model, it is first necessary to define a suitable mass profile for the underlying density distribution. As is described by equation (2.48), the density of a constant r shell is given in terms of the function $R(t, r)$ and the dipole modulation of $\mathcal{E}'/\mathcal{E}$. However, this equation also contains the yet to be specified mass function $M(r)$, which simply varies with the radial coordinate. So long as this function is selected appropriately, there is a reasonable amount of choice in the form it assumes.

3.1.1 The Mass Distribution

For our simulations, we adopt the same mass profile utilised by both BNW and Dam (2016) [107], which features a large, central under-density with respect to the background density at the origin. The mass distribution $M(r)$ of this model is given by

$$M(r) = M_0(r) + \delta M(r) = \frac{1}{2}\Omega_{m0}{H_0}^2 r^3 (1 + \delta(r)) \,, \tag{3.1}$$

where

$$M_0(r) = \frac{4}{3}\pi\bar{\rho}\,(t_0)\,r^3 = \frac{1}{2}\Omega_{m0}{H_0}^2 r^3 \,, \tag{3.2}$$

is the homogeneous FLRW mass profile of the background. Within equation (3.1) the function $\delta M(r)$ describes the deviation of the mass profile from that of the homogeneous background M_0. This deviation is further specified in terms of the function

$$\delta(r) = \frac{1}{2}\delta_0 \left(1 - \tanh\frac{r - r_0}{2\Delta r}\right) \,, \tag{3.3}$$

which depends on a local perturbation parameter $\delta_0 \in [-1, 0]$. This negative perturbation will correspond to an under-dense region centred on the origin of the model so that the mass profile will be below that of the background for $r < r_0$, where the parameter r_0 gives the chosen characteristic size of the void. The parameter Δr then controls the steepness of the void density profile, i.e., the rate of transition between the model's over-dense and under-dense regions. By defining our Szekeres model in this fashion, the deviation described by (3.3) will approach zero as $r \to \infty$. When this occurs, we have $M(r) \to M_0(r)$, such that the mass profile asymptotically approaches that of the homogeneous FLRW background.

3.1.2 Specifying the Szekeres Functions

Thus far we have identified the three parameters δ_0, r_0 and Δr, which allow us to control the physical characteristics of the Szekeres void via the mass profile $M(r)$. It now remains to specify the dipole functions within (2.44, such that the density equation (2.48 is fully defined. As we are interested in the same axially symmetric Szekeres model as

BNW, we will define our dipole functions by,

$$P(r) = 0\,, \qquad Q(r) = 0\,, \qquad S(r) = \left(\frac{r}{1\,\mathrm{Mpc}}\right)^{\alpha}\,\mathrm{Mpc}\,, \tag{3.4}$$

where the parameter α is introduced to control the strength of the dipole displacements. With only the function $S(r)$ non-constant, the dipole will be confined to z-axis of a shell's LRF. Correspondingly, the Szekeres shells will only undergo shifting along this axis in the direction of $(\theta, \phi) = (0, 0)$. As $P' = Q' = 0$, there will be no rotational effects requiring extra consideration. It further follows under this choice of parametrisation that the LTB model can be retrieved by setting $\alpha = 0$ such that $S' = P' = Q' = 0$.

Maintaining the specifications of BNW, we choose the function $R(t, r)$ to coincide with the coordinate-r at the present time. This fixes the coordinates so that $R(t_0, r) = r$ with t_0 the current age of the universe. In addition, we define the big bang singularity to occur simultaneously for all comoving observes, so that $t_B(r) = 0$ for all r. A value for $k(r) = -2E(r)$ may then be obtained for each r by solving (2.47) with attention to our choice of $R(t_0, r) = r$.

3.1.3 Specifying the Model Parameters

The model specifications of BNW are now summarised in terms of four parameters, these being α, δ_0, r_0 and Δr respectively. However, in addition to these there exist a further three parameters r_{obs}, θ_{obs} and ϕ_{obs}, that are responsible for the observer's location relative to the model's origin. The observer position relative to structures within the model plays a significant role in the anisotropy observed on their sky. However, in the axially symmetric case it suffices to choose $\phi_{\text{obs}} = \pi/2$, as when $P(r) = Q(r) = 0$ there is no model variation with the ϕ coordinate. Furthermore, BNW choose $\Delta r = 0.1\,r_0$ to simplify the parameter space down to five free parameters: α, δ_0, r_0, r_{obs} and θ_{obs}. While these parametrisation choices produce an idealised, easy to handle Szekeres model, it overall lacks the complexity required to produce exact representations of local structures. Despite this, the model is still capable of demonstrating realistic anisotropic effects that resemble features present in observations.

To obtain the best values for the model's five free parameters, BNW performed a parameter space search with the following constraints in order of significance:

1. A maximum CMB temperature of $T_0 + \Delta T$ where

$$\Delta T(l = 276.4^\circ, b = 29.3^\circ) = 5.77 \pm 0.36\,\mathrm{mK}\,, \tag{3.5}$$

is the amplitude and direction of the CMB dipole in the frame of the LG and $T_0 = 2.725\,\mathrm{K}$ is the mean CMB temperature.

2. A CMB quadrupole that is lower than the observed value of

$$C_{2,\mathrm{CMB}} < 242.2^{+563.6}_{-140.1}\,\mu\mathrm{K}^2\,. \tag{3.6}$$

   Although this value is much smaller than what is expected under the standard cosmology, the constraint ensures that the quadrupole generated from local inhomogeneities is less than what arises due to baryonic physics at last scattering.

3. A dipole in the Hubble expansion anisotropy that is consistent with the observed anisotropy of the COMPOSITE dataset, including the redshift dependence.

4. A quadrupole in the Hubble expansion anisotropy that is consistent with the observed anisotropy of the COMPOSITE dataset, including the redshift dependence.

By imposing these constraints, BNW obtained the following free parameter values through a grid search of the parameter space:

$$\begin{aligned} \alpha &= 0.86\,, \\ \delta_0 &= -0.86\,, \\ r_0 &= 38.5\,h^{-1}\,\mathrm{Mpc}\,, \\ \Delta r &= 0.1\,r_0\,. \end{aligned} \tag{3.7}$$

They also determine an observer position of

$$\begin{aligned} r_{\mathrm{obs}} &= 25\,h^{-1}\,\mathrm{Mpc}\,, \\ \theta_{\mathrm{obs}} &= 0.705\pi\,, \\ \phi_{\mathrm{obs}} &= 0.5\pi\,, \end{aligned} \tag{3.8}$$

where r_{obs}, θ_{obs} and ϕ_{obs} are the spherical coordinates of the observer from the centre of the Szekeres model. However, it is important to note that these particular parameter values were determined from routines containing the incorrect initialisation method for the initial null vectors (which will alter the directions in which light rays are propagated). Although we continue to use these values in our present work, they do not necessarily correspond to the best-fit values of the model using the corrected routines.

In fig. 3.1, we plot the density of our Szekeres model both with and without the shell shifting effects described in section 2.2.4. As to be expected, there are no rotations applied

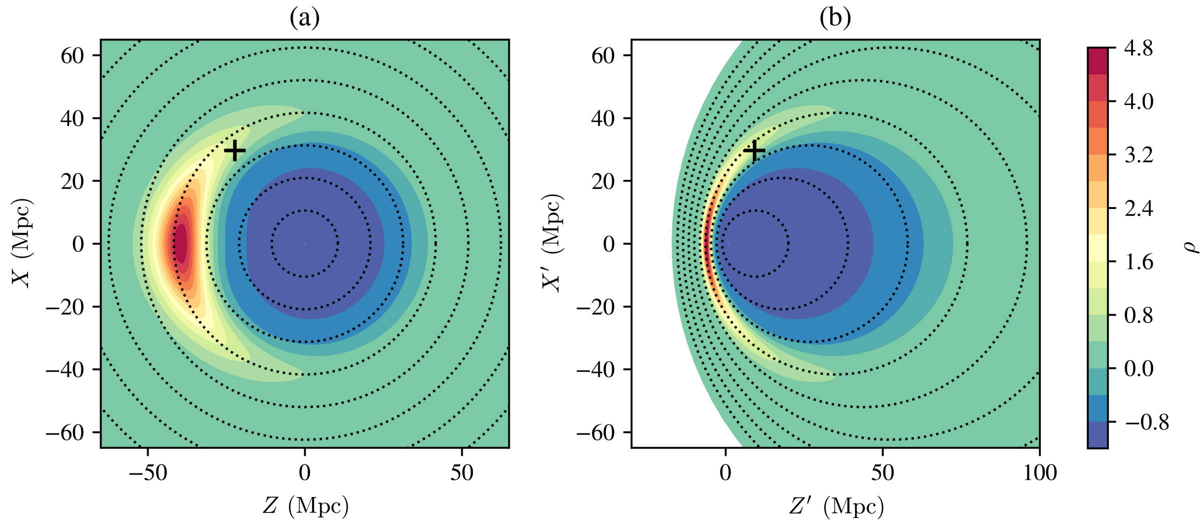

Figure 3.1: The density distribution of our axially symmetric Szekeres model normalised to the FLRW background density, where $X = R(t_0, r)\hat{x}$, $Z = R(t_0, r)\hat{z}$ and Z' is determined by (2.57) in the absence of shell rotations. In both panels, shells of constant r are traced with thin dotted circles, while the cross indicates the observer located at $(r_{\rm obs}, \theta_{\rm obs}, \phi_{\rm obs}) = \left(25\,h^{-1}\,\text{Mpc},\, 0.705\,\pi,\, 0.5\,\pi\right)$. The *left-hand* panel (a), shows the model plotted 'naïvely' without accounting for shell shifting along the symmetry axis. The *right-hand* panel shows the model correctly plotted with shell shifting effects. This is achieved following the method described in section 2.2.4.

to the shells, as $P' = Q' = 0$ in the quasi-spherical case. However, we can see that each shell is shifted along the negative Z'-axis, compressing the shells where the density of the model is greatest. The extent of the over-density appears much narrower along the Z'-axis.

3.1.4 The Cosmological Parameters

As the density is defined in terms of a spatially flat FLRW background, we must specify appropriate cosmological parameters. We will adopt the same values as were used by both BNW and Dam [107], namely,

$$(\Omega_{m0}, \Omega_{\Lambda 0}, \Omega_{k0}, h) = (0.315, 0.685, 0, 0.673)\ , \tag{3.9}$$

which are themselves derived from the *Planck* dataset for a best-fit spatially flat FLRW cosmology. The present day Hubble constant is then,

$$H_0 = 67.3\,\text{km}\,\text{s}^{-1}\,\text{Mpc}^{-1}\,, \tag{3.10}$$

as $H_0 = 100\,h\,\mathrm{km\,s^{-1}\,Mpc^{-1}}$. Since we have $\Omega_k = 0$, the present age of the universe t_0 can then be determined through the following analytic solution of the Friedmann equation

$$t_0 = \frac{1}{3H_0\sqrt{\Omega_\Lambda}} \ln\left(\frac{1+\sqrt{\Omega_\Lambda}}{1-\sqrt{\Omega_\Lambda}}\right) . \tag{3.11}$$

3.2 Analysis on the Spherical Sky

As we are dealing with measurements of both the CMB temperature anisotropies and average Hubble flow variation over the spherical sky, it is necessary to deal with the observed fields in terms of spherical harmonic functions. When considering the CMB temperature field in particular, which is understood to arise due to statistical processes in the primordial plasma, the estimated power spectrum of a given monopole can be determined via the corresponding spherical harmonic coefficients. In our analysis, we utilise the HEALPix (Hierarchical Equal Area isoLatitude Pixelisation) scheme to efficiently store our ray traced datasets and routinely perform a spherical harmonic analysis of the results.

3.2.1 Computation of the CMB Dipole

Firstly, the quantities of interest must be expressed as functions of the angular position of observation on the sky. For example, deviations from the mean CMB temperature T_0 can be characterised by the dimensionless anisotropy function,

$$\Theta(\theta,\phi) = \frac{\Delta T(\theta,\phi)}{T} = \frac{T(\theta,\phi) - T_0}{T_0} . \tag{3.12}$$

We can then perform a spherical harmonic decomposition of this temperature anisotropy into a sum of spherical harmonic functions $Y_{\ell m}$ and coefficients $a_{\ell m}$

$$\Theta(\theta,\phi) = \sum_{\ell=0}^{\infty} \sum_{m=-\ell}^{\ell} a_{\ell m}\, Y_{\ell m} , \tag{3.13}$$

where for each multipole value $\ell \geq 0$ there are $2\ell+1$ values of m. For the dipole component $\ell = 1$ there are three separate $Y_{\ell m}$ to consider for $m = \pm 1$ and $m = 0$ as follows:

$$Y_{10} = \sqrt{\frac{3}{4\pi}} \cos\theta \tag{3.14a}$$

$$Y_{1\pm1} = \mp\sqrt{\frac{3}{8\pi}} \sin\theta\, e^{\pm i\phi} \tag{3.14b}$$

To examine the dipole ($\ell = 1$) component of (3.13), we expand the equation out using (3.14a) and (3.14b) to obtain

$$\begin{aligned}
\sum_{m=-1}^{1} a_{1m}\, Y_{1m} &= \sqrt{\frac{3}{8\pi}}\, \sin\theta\, e^{-i\phi} + \sqrt{\frac{3}{4\pi}}\, \cos\theta - \sqrt{\frac{3}{8\pi}}\, \sin\theta\, e^{i\phi} \\
&= \sqrt{\frac{3}{8\pi}} \Big[\big(a_{1-1} + a^{*}_{1-1}\big)\, \sin\theta\, \cos\phi + \sqrt{2}\, a_{10}\, \cos\theta \\
&\qquad\qquad - i(a_{11} - a^{*}_{11})\, \sin\theta\, \sin\phi \Big] \\
&= \sqrt{\frac{3}{8\pi}} \Big[2a^{im}_{11}\, \sin\theta\, \sin\phi - 2a^{re}_{11}\, \sin\theta\, \cos\phi + \sqrt{2}\, a_{10}\, \cos\theta \Big] \\
&= \boldsymbol{d} \cdot \hat{\boldsymbol{n}}\,, \qquad (3.15)
\end{aligned}$$

where we have used the fact that $a^{*}_{\ell m} = (-1)^m\, a_{\ell -m}$ and $a^{re}_{1-1} = -a^{re}_{11}$, with starred quantities denoting the complex conjugate. The vector

$$\hat{\boldsymbol{n}} = \left(n^{\hat{x}}, n^{\hat{y}}, n^{\hat{z}}\right) = (\sin\theta\cos\phi, \sin\theta\sin\phi, \cos\theta) \qquad (3.16)$$

is the observed direction of the dipole on the sky, while the vector

$$\boldsymbol{d} = (d_x, d_y, d_z) = \sqrt{\frac{3}{4\pi}} \left(-\sqrt{2}a^{re}_{11}, \sqrt{2}a^{im}_{11}, a_{10}\right) \qquad (3.17)$$

gives the components of its magnitude determined by the $a_{\ell m}$ coefficients. Considered individually, these coefficients are determined over the full sphere of observations

$$a_{\ell m} = \int_0^{2\pi} \mathrm{d}\phi \int_0^{\pi} \mathrm{d}\theta \sin\theta\, \Theta(\theta, \phi)\, Y^{*}_{\ell m}(\theta, \phi) \qquad (3.18)$$

with the first few $a_{\ell m}$ containing the bulk of the information about the CMB sky, given that we are particularly concerned with large angle fluctuations. The amplitude (or temperature) of the ℓ-th spherical harmonic is given by

$$\Delta T_{\ell}^{2} = \sum_{m} \frac{|a_{\ell m}|^2}{4\pi}, \qquad (3.19)$$

3.2.2 Cosmic Variance

As the observed CMB is only a single realisation of an underlying statistical process, the coefficients $a_{\ell m}$ can be considered as independently distributed complex random variables with zero mean. The mean value of the power spectrum as a function of the ℓ-th multipole is thus

$$C_\ell = \langle |a_{\ell m}|^2 \rangle \,, \tag{3.20}$$

which is equivalent to an ensemble average over many independent realisations by assuming ergodicity[1] of the underlying model. Because each C_ℓ is independent of m (of which there are $2\ell+1$ values for each ℓ) we can construct an unbiased estimator for C_ℓ as follows:

$$\tilde{C}_\ell = \frac{1}{2\ell+1} \sum_m |a_{\ell m}|^2 \,, \tag{3.21}$$

although this assumes a complete sky coverage.

If we assume that the temperature anisotropy field $\Theta(\hat{\boldsymbol{n}})$ is statistically isotropic, where the unit vector $\hat{\boldsymbol{n}}$ is the observed direction on the sky, then the 2-point correlation function

$$C(\hat{\boldsymbol{n}}, \hat{\boldsymbol{n}}') = \langle \Theta(\hat{\boldsymbol{n}})\, \Theta(\hat{\boldsymbol{n}}') \rangle \,, \tag{3.22}$$

depends solely on the angle θ between the $\hat{\boldsymbol{n}}$ and $\hat{\boldsymbol{n}}'$ as follows

$$C(\hat{\boldsymbol{n}}, \hat{\boldsymbol{n}}') = (\hat{\boldsymbol{n}} \cdot \hat{\boldsymbol{n}}') = C(\theta) \,, \tag{3.23}$$

where $\hat{\boldsymbol{n}} \cdot \hat{\boldsymbol{n}}' = \cos\theta$. This is because in the case of statistical isotropy, the CMB is rotationally invariant. By then expanding the 2-point correlation function $C(\theta)$ in terms of Legendre polynomials, $P_\ell\,(\cos\theta)$ we obtain

$$C(\theta) = \frac{1}{4\pi} \sum_\ell (2\ell+1)\, C_\ell\, P_\ell\,(\cos\theta) \,, \tag{3.24}$$

---

[1] If an underlying model satisfies the requirements of the ergodic theorem the ensemble average can instead be interpreted as an average over all positions of a distinct realisation. This can be shown to be the case for Gaussian random fields, such as that of the CMB temperature fluctuations.

by the addition theorem of spherical harmonic functions. Further manipulation of equation (3.24) by applying the orthogonality relation of spherical harmonic functions then yields

$$\langle a_{\ell m}\, a^*_{\ell' m'} \rangle = \delta_{\ell\ell'}\, \delta_{mm'}\, C_\ell\,. \tag{3.25}$$

This result demonstrates that for a statistically isotropic field, the real space 2-point correlation function $C(\theta)$ holds the same information as the angular power spectrum $C_\ell = \langle |a_{\ell m}|^2 \rangle$ in harmonic space. As the latter is independent of the angular resolution of the experiment, it is the most relevant for comparative purposes.

Because we are restricted in our estimation of C_ℓ to an average over m, the difference in the observed mean versus the ensemble average of the power spectrum gives a measure of cosmic variance,

$$\sigma_\ell{}^2 = \left\langle \left(C_\ell - \tilde{C}_\ell \right)^2 \right\rangle = \frac{2}{2\ell + 1} C_\ell{}^2 \tag{3.26}$$

which is significant over large scales.

3.2.3 Mapping the Sky with HEALPix

Working with data that is projected upon a spherical sky, such as our ray traced CMB and spherically averaged Hubble expansion variation, requires an efficient mapping method that can handle a large volume of unique data points. As in BNW, our simulations utilise the HEALPix (Hierarchical Equal Area isoLatitude Pixelisation) libraries, which handles the data points in a pixelised spherical map for ease of manipulation.

Mapping of the CMB sky in a pixelised format was first accomplished with the COBE quadrilateralised spherical cube scheme, whereby the sky is projected onto an inscribed cube using a curvilinear area-conserving projection. However, with the increasing resolution of the later WMAP and Planck detectors, it became necessary to adopt a more efficient pixelisation scheme that allowed for fast computations across the entire sky. The HEALPix scheme of Gorski*et al.* [119] has since become the standard CMB data format. The pixelated map data is stored on a sphere using a tree-structured tessellation, with each of the equally sized pixels corresponding to a (l, b) coordinate position.

The resolution of the HEALPix map is given by $N_{\mathrm{pix}} = (12N_{\mathrm{side}})^2$, where $N_{\mathrm{side}} = \{4, 8, 16, ...\}$ is the number of subdivisions required of the 12 base resolution tiles to achieve the target resolution. In the majority of our simulations, we set $N_{\mathrm{side}} = 8$ to minimise the computational intensity involved in ray tracing the COMPOSITE dataset. Each map is therefore comprised of 768 uniquely indexed pixels, which HEALPix can efficiently

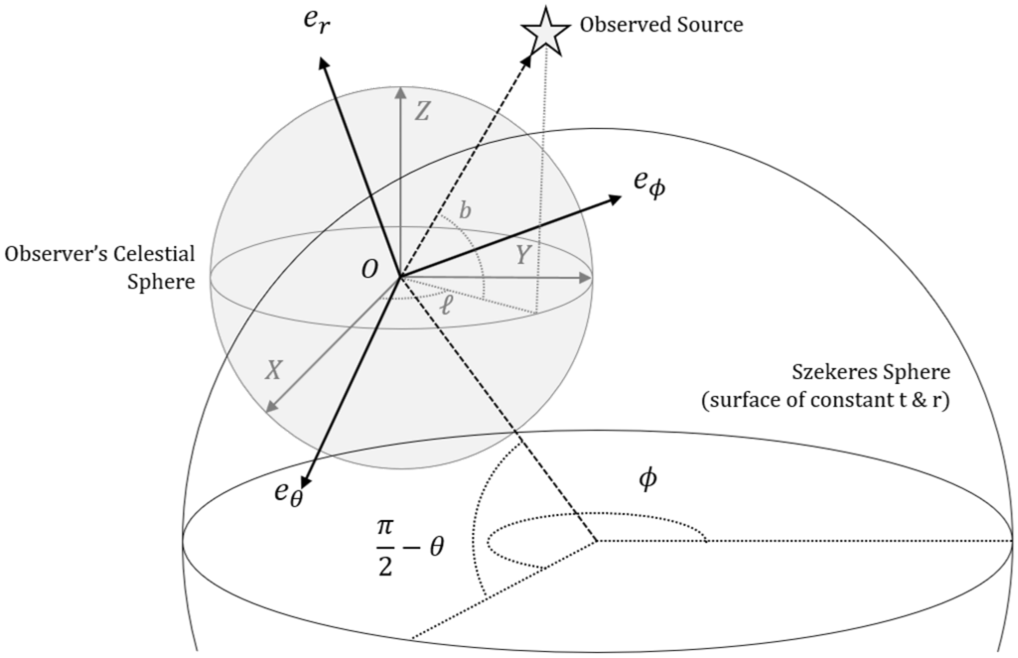

Figure 3.2: The relationship between the celestial sphere of the observer within the Szekeres model and the Szekeres spherical coordinates. Adapted from Dam [107].

evaluate in terms of spherical harmonics. In practice, the integration in determining the a_{lm} coefficients by equation (3.18) becomes a sum over $N_{\rm pix}$ pixels

$$\begin{aligned} a_{\ell m} &\approx \sum_{i=1}^{N_{\rm pix}} \Theta(\theta_i, \phi_i)\, Y^*_{\ell m}(\theta_i, \phi_i)\, \sin\theta_i\, \Delta\theta_i\, \Delta\phi_i \qquad (3.27) \\ &= \frac{4}{N_{\rm pix}} \sum_{i=1}^{N_{\rm pix}} \Theta(\hat{\boldsymbol{n}}_i)\, Y^*_{\ell m}(\hat{\boldsymbol{n}}_i)\,, \qquad (3.28) \end{aligned}$$

where $\Delta\theta_i$ is constant as each $N_{\rm side}$ indexes an isolatitude band. After the calculation of the $a_{\ell m}$ and C_ℓ via HEALPix's subroutines, the dipole position and amplitude are derived using equations (3.17) and (3.19) (for $\ell = 1$), respectively.

3.3 The Ray Tracing Methodology

The key stages of the ray tracing simulation are as follows:

1. After defining our Szekeres model according to the functions (3.1), (3.2), (3.3) and (3.4), we begin by ray tracing the CMB dipole as seen by the observer. This is achieved by propagating individual light rays through the Szekeres model to each of the $N_{\rm pix}$ pixels of the HEALPix sky, before then determining the amplitude and

position vector of the generated dipole.

2. Using the position vector of the ray traced CMB dipole, the true CMB dipole position and the positions of the COMPOSITE dataset in galactic coordinates (l, b) are rotated onto the Szekeres local sky coordinates (θ, ϕ) [2]. A schematic diagram of the relation between the various coordinates is given in fig. 3.2.

3. After expressing the position of each galaxy in the Szekeres coordinate frame, we begin to ray trace the full COMPOSITE dataset via numerical integration of the null geodesic equations. For each galaxy, a ray is backwards propagated from the observer to the source until the given distance of galaxy d_i is achieved. This allows us to obtain the modified redshift of the galaxy as observed through the intervening Szekeres model.

4. Once the entire COMPOSITE dataset has been ray traced, the Hubble expansion variation is calculated using spherical averages for increasing redshift values up to $z = 0.08$. At each redshift considered, the distances of the ray traced COMPOSITE sample are randomly reshuffled 5000 times to reproduce fig. 6 of BNW.

3.3.1 Setting the Initial Conditions

In the following section, we detail the corrected procedure for setting the initial null vector of each ray according to Dam [107]. As each individual pixel of the HEALpix sky corresponds to the direction in which a ray is observed, we first determine an observed direction vector $\boldsymbol{\hat{n}}$ of a local spatial frame in terms of the pixel's (l, b) coordinates. In Cartesian coordinates, the components of $\boldsymbol{\hat{n}}$ are simply:

$$\hat{n}^x = \cos b \cos l \,, \qquad \hat{n}^y = \cos b \sin l \,, \qquad \hat{n}^z = \sin b \,. \tag{3.29}$$

The next step is to determine the local orthonormal basis $\{\boldsymbol{e}_{\hat{a}}\}$ by considering the following line element,

$$\mathrm{d}s^2 = g_{\mu\nu} \, \mathrm{d}x^\mu \otimes \mathrm{d}x^\nu = \eta_{\hat{a}\hat{b}} \, \boldsymbol{\omega}^{\hat{a}} \otimes \boldsymbol{\omega}^{\hat{b}} \,, \tag{3.30}$$

---

[2] The Szekeres local sky coordinates (θ, ϕ) referenced here should not be confused with the spacetime θ and ϕ coordinates.

where $\eta_{\hat{a}\hat{b}} = \text{diag}{-1,1,1,1}$. The 1-forms $\{\boldsymbol{\omega}^{\hat{a}}\}$ dual to the orthonormal basis $\{\boldsymbol{e}_{\hat{a}}\}$ are then given by

$$\boldsymbol{\omega}^{\hat{a}}(\boldsymbol{e}_{\hat{b}}) = \omega_\mu^{\hat{\alpha}}\, e^\mu_{\hat{b}} = \delta^{\hat{a}}_{\hat{b}}\,, \tag{3.31}$$

where $\omega^{\hat{\alpha}}_\mu$ are simply the components of $\boldsymbol{\omega}^{\hat{a}}$. The line element of our axially symmetric Szekeres model follows from the metric (2.43) with $N(r,\phi) = 0$:

$$\begin{aligned} ds^2 = &- \mathrm{d}t^2 + \frac{1}{1+2E}\left[R' + \frac{R}{S}(S'\cos\theta)\right]^2 \mathrm{d}r^2 + \left(\frac{S'}{S}\right)^2 R^2 \sin^2\theta\, \mathrm{d}r^2 \\ &- 2\left(\frac{S'}{S}\right) R^2 \sin\theta\, \mathrm{d}r\, \mathrm{d}\theta + R^2\big(\mathrm{d}\theta^2 + \sin^2\theta\, \mathrm{d}\phi^2\big)\,. \end{aligned} \tag{3.32}$$

By extracting the 1-forms from this line element and using them to solve equation (3.31), we obtain the following orthonormal basis

$$e_{\hat{a}}{}^{\mu} = \begin{pmatrix} 1 & 0 & 0 & 0 \\ 0 & \Gamma & 0 & 0 \\ 0 & \Gamma \frac{S'}{S}\sin\theta & \frac{1}{R} & 0 \\ 0 & 0 & 0 & \frac{1}{R\sin\theta} \end{pmatrix}, \tag{3.33}$$

where

$$\Gamma = \frac{\sqrt{1+2E}}{R}\left(\frac{R'}{R} + \frac{S'}{S}\cos\theta\right)^{-1}. \tag{3.34}$$

Because in the local orthonormal frame we have $k^{\hat{a}} = (-1, \hat{\boldsymbol{n}})$, with the affine parameter defined so that the rays propagate backwards in time, we finally transform back into Szekeres spherical coordinates

$$k_0^\mu = k^{\hat{a}}\, e_{\hat{a}}{}^{\mu}\big|_{t=t_0} = \begin{pmatrix} -1 \\ \Gamma\, \hat{n}^x \\ \Gamma\, \frac{S'}{S}\sin\theta\, \hat{n}^x + \frac{1}{R}\, \hat{n}^y \\ \frac{1}{R\sin\theta}\, \hat{n}^z \end{pmatrix}_{t=t_0}. \tag{3.35}$$

However, in the original ray tracing routines of BNW the initial null vectors are incorrectly calculated due to the erroneous neglecting of off-diagonal terms in the Szekeres metric.[3] This meant that each null vector was instead normalised by taking

$$k_0^r = \frac{k^{\hat{r}}}{\sqrt{g_{rr}}}\,, \qquad k_0^\theta = \frac{k^{\hat{\theta}}}{\sqrt{g_{\theta\theta}}}\,, \qquad k_0^\phi = \frac{k^{\hat{\phi}}}{\sqrt{g_{\phi\phi}}}\,. \tag{3.36}$$

Consequently, by taking the spatial norm,

$$\begin{aligned} g_{ij}\, k_0^i\, k_0^j &= \left(k^{\hat{r}}\right)^2 + \left(k^{\hat{\theta}}\right)^2 + \left(k^{\hat{\phi}}\right)^2 + \frac{2g_{r\theta}}{\sqrt{g_{rr}g_{\theta\theta}}}\,, \\ &= 1 - 2\frac{S'}{S}\sin\theta\left[\left(\frac{S'}{S}\sin\theta\right)^2 + \frac{1}{1+2E}\left(\frac{R'}{R} + \frac{S'}{S}\cos\theta\right)^2\right]^{-1/2}\,, \end{aligned} \tag{3.37}$$

it is evident that the resulting vector field k^μ is timelike as opposed to null. Furthermore, because both $k^{\hat{r}}$ and $k^{\hat{\theta}}$ contain local direction cosines, a global scaling cannot distort the impacted results into correct ones.

3.3.2 The COMPOSITE Dataset

The determination of the average Hubble expansion variation within our Szekeres model requires a large sample of galaxies to serve as tracers. Not only must the sample have excellent sky coverage to prevent the biasing of results, but it must also contain a range of individual distances extending up to $\sim 100\,h^{-1}\,$Mpc to thoroughly probe the entire volume of the Szekeres model.

As in BNW, we choose[4] to use the COMPOSITE dataset of Watkins *et al.* (2009), which contains 4534 galaxies and clusters compiled across eight independent sky surveys, with a combined characteristic depth of $34\,h^{-1}\,$Mpc. As a peculiar velocity dataset, the sample was used to obtain a bulk flow estimate of $407 \pm 81\,\mathrm{km\,s^{-1}}$ in the direction of $(l, b) = (287^\circ \pm 9^\circ, 8^\circ \pm 6^\circ)$ within a Gaussian window of radius $50\,h^{-1}\,$Mpc. This was found to disagree significantly with the expectations from ΛCDM with WMAP5 cosmological

---

[3] As is discussed in section 2.2.2, the Szekeres metric is only diagonal when $S(r) = P(r) = Q(r) = 0$ - which is when it reduces to the LTB metric. The BNW code used a routine that is correct for the LTB model, and computationally faster in that case - but unfortunately, it is incorrect for the Szekeres model.

[4] There are other larger datasets now available, such as the *Cosmicflows* datasets. However, as compared to the COMPOSITE sample, the data in these larger datasets still contains sampling biases whose removal is the subject of ongoing investigations.

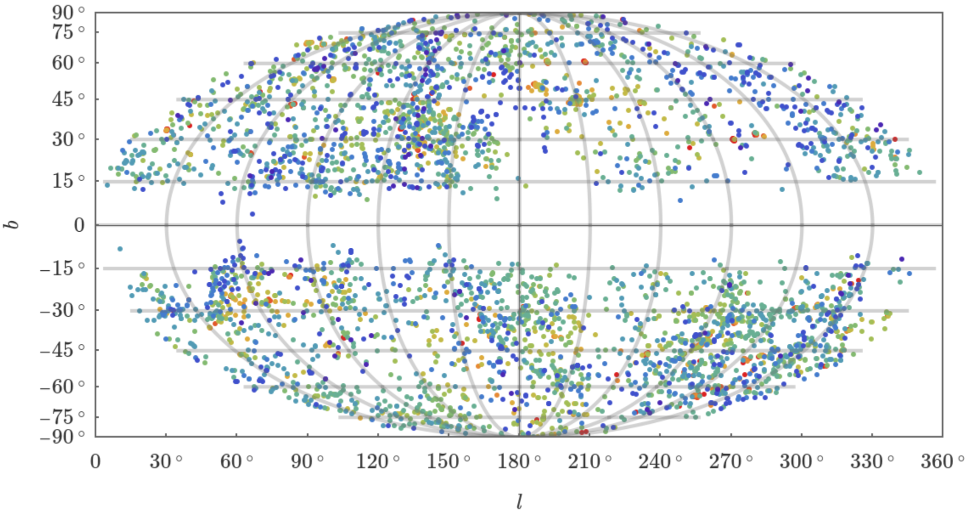

Figure 3.3: Angular distribution of the COMPOSITE dataset on the sky in standard galactic coordinates (l, b). The band of sparse coverage along $b = 0°$ is due to the 'Zone of Avoidance' caused by obscuration from the Milky Way.

parameters, with the overall motion not attributable to the presence of nearby structures (e.g. the Great Attractor at $\sim 40\,h^{-1}$ Mpc). Despite the range of characteristic depths and the different distant measurement techniques that were used, the constituent samples of COMPOSITE are found to be statistically consistent with each other. These results are also consistent with the later reanalysis performed by Feldman *et al.* (2010), where the erroneous contributions to COMPOSITE from the SFI++ survey are corrected for Malmquist bias.

As demonstrated in fig. 3.3, the COMPOSITE sample has excellent coverage over the sky, with exception to the 'Zone of Avoidance' obscured by the Milky Way between approximately $\pm 15°$ of the galactic plane ($b = 0°$). Around 85% of the sample resides within the range of $100\,h^{-1}$ Mpc (see fig. 3.4), with the observations becoming much sparser towards $\sim 150\,h^{-1}$ Mpc. Each galaxy within the dataset is supplied with its redshift z_i, luminosity distance d_i, peculiar velocity v_i and uncertainty Δv_i (which correspond to individual distance uncertainties of $\Delta d_i = \Delta v_i / H_0$). The position of each galaxy in galactic coordinates (l_i, b_i) is also provided within the dataset.

To assess the dataset for systematic uncertainties occurring due to incomplete sky coverage, the previous investigation of [4] performed 12 million random reshuffles of the data in independent radial shells. For a binning scale of $\Delta d = 12.5\,h^{-1}$ Mpc (or equivalently $\Delta z \simeq 0.001$), they found their results pertaining to the dipole anisotropy were robust over scales of $0.002 < z < 0.04$. Nevertheless, BNW performed additional tests upon the data, including:

- Analysing the fluctuations $\Delta H_0 / H_0$ instead of just the spherically averaged H_0.

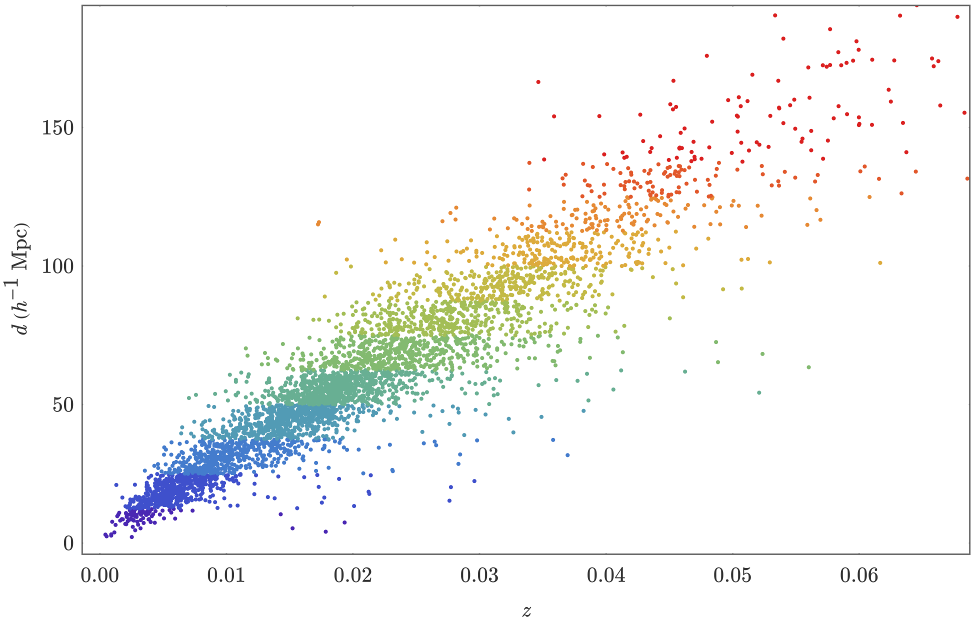

Figure 3.4: Redshift-distance diagram of the COMPOSITE dataset. All 4534 galaxies and clusters within the sample are included, with the colours grouping the sample into increasing 12.5 h^{-1} Mpc shells based on the distance d.

Because $\delta H_0 = 0$ for a perfectly homogeneous and isotropic universe (hypothetically speaking), a largely incomplete sky coverage should still have an undetectable anisotropy.

- Analysing the dipole and quadrupole anisotropies of 100,000 reshuffled COMPOSITE datasets, which were made by randomly reshuffling the angular position (l, b) for each set of z and d_L. They concluded from this that the anisotropies present in the original dataset are not spurious.

- Additionally checking for the presence of spurious anisotropies using 100,000 randomly selected halves of the COMPOSITE dataset. The anisotropies present in each half were analysed and compared with the dipole and quadrupole of the original sample. This again confirmed that the measured anisotropies were indeed not spurious.

3.4 The Hubble Expansion Anisotropy

After generating a ray traced CMB sky for an observer located at $(r, \theta, \phi)_{\rm obs}$ within our Szekeres model, the observed CMB dipole at $(\ell, b) = (276.4^\circ, 29.3^\circ)$ in galactic coordinates is mapped onto the ray traced dipole in the Szekeres local sky coordinates. The COMPOSITE dataset, when aligned appropriately, can then be ray traced to determine each galaxy's observed redshift as influenced by the underlying Szekeres model.

In a general inhomogeneous cosmology, one cannot expect an isotropic distance-redshift relation of the form (1.11) at low redshifts. Recently, Heinesen [120] has developed an alternative low-redshift cosmographic expansion applicable to a wide variety of cosmological models, which incorporates anisotropic effects of differential expansion. Nonetheless, we will use (1.11) in our redshift-distance determinations, since our Szekeres model is asymptotically FLRW at modest redshifts.

By rearranging equation (1.11) for a spatially flat FLRW model, the Hubble constant at low redshifts is

$$H_0 = \frac{c}{d_L}\left[z + \frac{1}{2}(1-q_0)z^2 - \frac{1}{6}\big(1 - q_0 - 3{q_0}^2 + j_0\big)z^3\right] + \mathcal{O}\big(z^4\big)\,. \tag{3.38}$$

However, as the distance uncertainties within COMPOSITE are typically of order $\sim 15\%$, it is more optimal to consider (3.38 with d_L as an independent variable in the numerator in terms of the propagation of the uncertainties. The value of H_0 can then be determined by performing a chi-squared minimisation of the form,

$$\chi^2 = \sum_i \left(\frac{d_i - c\,\xi_i/H_0}{\Delta d_i}\right)^2 , \tag{3.39}$$

where ξ_i is simply,

$$\xi_i = \left[z_i + \frac{1}{2}(1-q_0){z_i}^2 - \frac{1}{6}\big(1 - q_0 - 3{q_0}^2 + j_0\big){z_i}^3\right]. \tag{3.40}$$

This is effectively a weighted sum over the $i \in [1, ..., 4534]$ objects of the COMPOSITE dataset, with d_i and z_i being the luminosity-distance and redshift of the i-th object, respectively.

In the previous work of [4], only the luminosity distance was smoothed for spherical averages in independent radial shells, with the angular smoothing considered separately. However, to determine the average local value of H_0 centred on galactic coordinates (l, b) and redshift z we apply a Gaussian window function that smooths jointly in both solid angle and redshift

$$H_0 = \frac{\sum_i H_i\, w_{d,i}\, w_{z,i}\, w_{\theta,i}}{\sum_i w_{d,i}\, w_{z,i}\, w_{\theta,i}} , \tag{3.41}$$

where H_i is given by

$$H_i = \frac{c\,\xi_i}{d_i}\,. \tag{3.42}$$

The smoothing weights of this sum are given by

$$w_{d,i} = \frac{c\,\xi_i\,d_i}{(\Delta d_i)^2}\,, \tag{3.43a}$$

$$w_{z,i} = \frac{1}{\sqrt{2\pi}\,\sigma_z}\,\exp\left[-\frac{1}{2}\left(\frac{z-z_i}{\sigma_z}\right)^2\right], \tag{3.43b}$$

$$w_{\theta,i} = \frac{1}{\sqrt{2\pi}\,\sigma_\theta}\,\exp\left[-\frac{1}{2}\left(\frac{\theta_i}{\sigma_\theta}\right)^2\right], \tag{3.43c}$$

where Δd_i is the distance uncertainty and the window function parameters are set to $\sigma_z = 0.01$ and $\sigma_\theta = 25°$. The angle θ_i is between the direction of each source (l_i, b_i) and the direction of an arbitrary point of the sky (l, b) where,

$$\cos\theta_i = \cos b\,\cos b_i\,\cos(l - l_i) + \sin b\,\sin b_i\,. \tag{3.44}$$

Due to the 15° 'Zone of Avoidance' either side of the galactic mid-plane, the angular Gaussian smoothing scale of $\sigma_\theta = 25°$ is used to extrapolate data from this region, instead of applying an appropriate mask. This reduces the biases that the masking of the region could otherwise introduce, while having minimal influence on the large-scale results.

Utilising the HEALPix scheme that was earlier described, we can use equations (3.41)-(3.44) to calculate all contributions to the Hubble constant for a given pixel direction on the sky. Then, similar to characterising the temperature anisotropies of the CMB, we can express the variation in the Hubble flow as

$$\frac{\Delta H_0}{\langle H_0\rangle} = \frac{H_0(l,b,z) - \langle H_0\rangle}{\langle H_0\rangle} \tag{3.45}$$

where

$$\langle H_0\rangle = \frac{1}{4\pi}\int \mathrm{d}\Omega\; H_0(l,b,z)\,, \tag{3.46}$$

is the spherically averaged value of equation (3.41). This variation can then undergo a spherical harmonic decomposition similar to that performed for the CMB anisotropies,

$$\frac{\Delta H_0}{H_0} = \sum_{\ell,m} a_{\ell m} Y_{\ell m}\,, \tag{3.47}$$

so that its fluctuations can be examined in terms of the angular power spectrum C_ℓ.

3.5 Kinematic Interpretation of Anisotropies

To test the kinematic dipole hypothesis as discussed in section 1.4, BNW produced 100,000 mock COMPOSITE catalogues in the CMB frame, where the universe is presumed to be spatially homogeneous. For each galaxy of the COMPOSITE dataset, the FLRW model is first used to obtain the redshift z_{FLRW} at which $d_L = d_i$ through solving

$$d_L = \frac{(1+z)\,c}{H_0}\int_0^{z_{\mathrm{FLRW}}} \frac{dz}{\sqrt{\Omega_{m0}(1+z)^3 + 1 - \Omega_{m0}}}\,, \tag{3.48}$$

where the best fit *Planck* value of $\Omega_{m0} = 0.315$ is used. The redshift z_{FLRW} is then adjusted for a boost to the frame of the local group by

$$\begin{aligned} 1 + z_{\mathrm{FLRW-B}} &= \gamma\,(1 - \beta_o\, \cos\theta_i)(1 + z_{\mathrm{FLRW}}) \\ &\simeq (1 - \beta_o\, \cos\theta_i)(1 + z_{\mathrm{FLRW}})\,, \end{aligned} \tag{3.49}$$

where $\beta_o = v_o/c = (2.1 \pm 0.1) \times 10^{-3}$ while the $\cos\theta_i$ term is given by (3.44). Within the mock catalogues, each galaxy's redshift z_i is replaced with a boosted redshift $z_{\mathrm{FLRW-B}}$ that is randomly drawn from a Gaussian distribution. Then, each distance d_i that is used in obtaining z_{FLRW} is replaced with a randomly drawn distance $d_{\mathcal{N}} = \mathcal{N}(\mu = d_i, \sigma = \Delta d_i)$. The resulting mock datasets may then be spherically averaged over the observer's sky following the method of section (3.4).

Chapter 4

The Ray Tracing Simulations

4.1 The Hubble Expansion Anisotropy

Following the procedure described in section 3.3, we have carried out a series of ray tracing simulations for the COMPOSITE dataset using the Szekeres model of BNW. In what follows, we compare our results for the ray traced Hubble expansion anisotropy variation with those originally obtained by BNW, which includes the bug in their null vector initialisation. These results are then considered in terms of their match to the COMPOSITE anisotropy, as well as for boosted FLRW mocks obtained following section 3.5. We also explore the variation of both the CMB and Hubble expansion anisotropy for various observer positions throughout the Szekeres model.

4.1.1 Comparison with Bolejko *et al.* 2016

A primary aim within this thesis was to examine how applying corrections to the erroneous null vector initialisation routine of BNW impacts the ray traced Hubble expansion anisotropy they originally presented. To accomplish this, we have reproduced the Szekeres ray tracing results of BNW using the incorrect null vector initialisation routine, which we then compare to results obtained by applying the corrections detailed in section 3.3.1. Overall, we find that there are significant differences in the spherically averaged Hubble expansion dipole when compared to the incorrect results of BNW. Our results are presented in fig. 4.1 for both the dipole C_1 and quadruple C_2 variation. We can immediately observe that correcting the null initialisation routine produces a dipole anisotropy almost three times larger than was originally reported by BNW, with the difference being especially prominent for $z \lesssim 0.04$.

For the BNW results shown in fig. 4.1, a CMB dipole amplitude of $\Delta T_d = 3.26\,\mathrm{mK}$ and

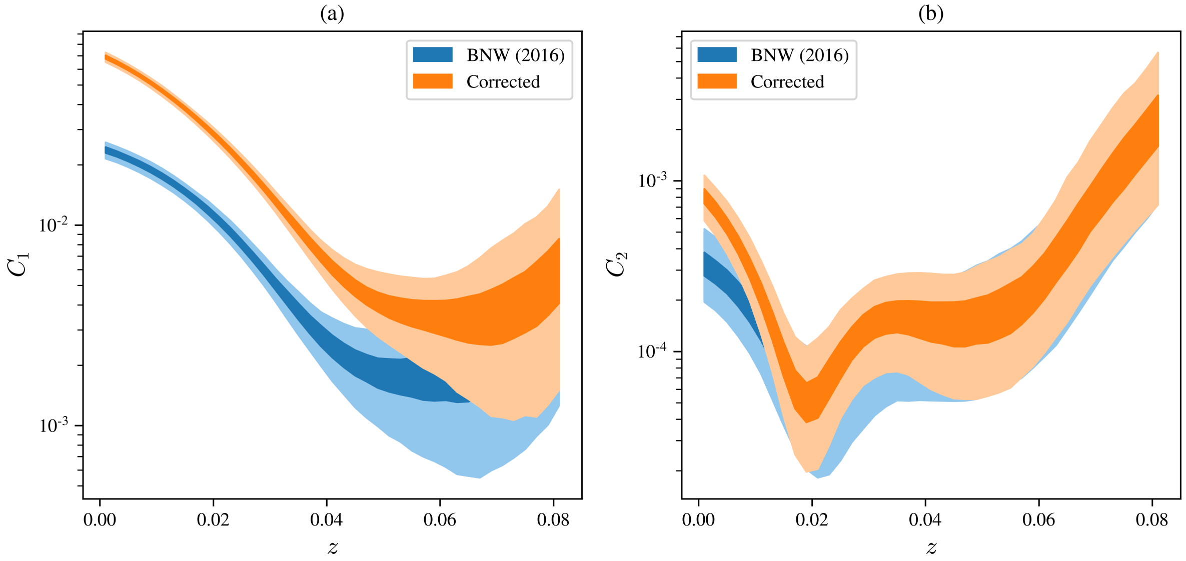

Figure 4.1: The Hubble expansion anisotropy variation observed in the ray traced Szekeres-COMPOSITE dataset. The *left-hand* panel (a) shows the dipole C_1 variation of the original BNW result of 2016 compared to the results of this thesis (where the corrected BNW ray tracing routines were used). The *right-hand* shows the same comparison of the results but for the quadrupole C_2 variation. The bands of each distribution give the 65% and 95% confidence intervals based on 1000 mock datasets at each redshift interval of the averaging.

a quadrupole amplitude of $\mathcal{D}_2 = 7.92\,\mu\mathrm{K}^2$ are obtained using the uncorrected ray tracing routine. This varies somewhat from the values reported by BNW, who state a CMB dipole amplitude of $\Delta T_d = 5.58\,\mathrm{mK}$ and a CMB quadrupole amplitude $\mathcal{D}_2 = 8.26\,\mu\mathrm{K}^2$. However, the significant difference in the dipole amplitude can be traced to the method used in its calculation. In the original codes of BNW, the dipole amplitude is determined by taking the difference of the maximum and minimum values of the HEALPix map – a method which is only valid if the map contains simply a dipole and quadrupole moment. As the maximum and minimum values may also not be at the antipodes, the presence of small $l > 3$ contributions can lead to an over-estimation of the dipole component. As the CMB dipole given in this thesis is determined from the a_{10} spherical harmonic (or C_1 coefficient), it is therefore smaller than the stated BNW value.

In the corrected results shown in figure 4.1, we instead find a CMB dipole amplitude of $\Delta T_d = 5.61\,\mathrm{mK}$ and a quadrupole amplitude of $\mathcal{D}_2 = 26.53\,\mu\mathrm{K}^2$, which is consistent with the results of Dam [107]. The quadrupole amplitude remains an order of magnitude smaller than that observed for the CMB, although this could be due to the relative simplicity of the specific axially symmetric Szekeres model that we have employed (which BNW themselves have argued [1]). Overall, it is apparent that the choice of parameters (3.7) and (3.8), that BNW determine by inadvertently using the incorrect null vector initialisation routine, no longer provide a match to the COMPOSITE anisotropy. This means a re-parametrisation of the Szekeres model and the observer position will most

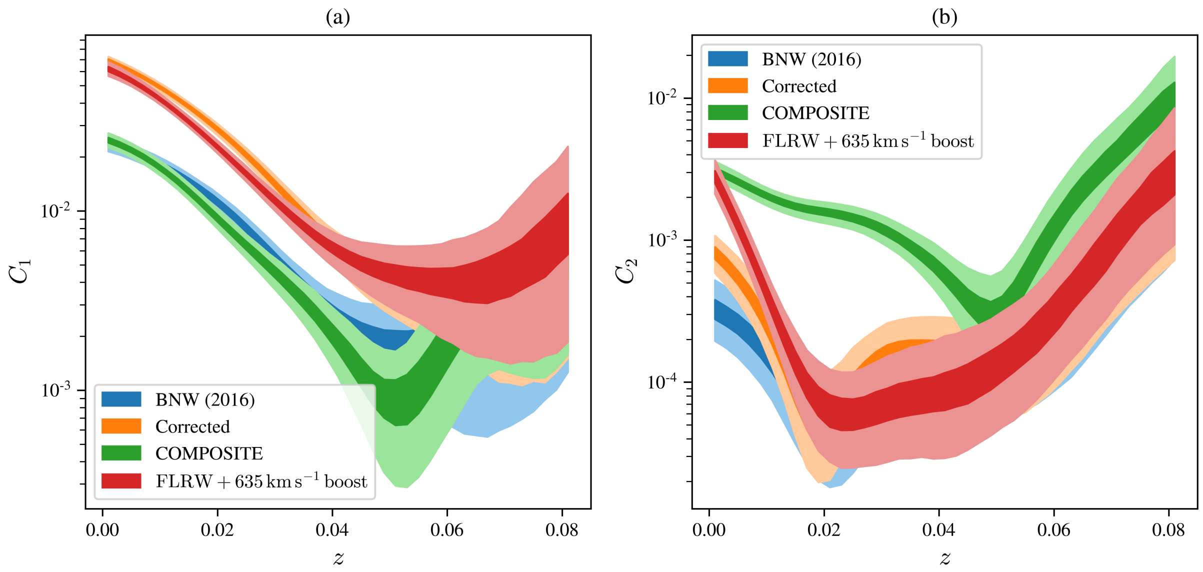

Figure 4.2: The Hubble expansion anisotropy results of figure 4.1 compared with that of the COMPOSITE dataset. Also shown are the results of producing mock COMPOSITE catalogues based on FLRW redshifts under a local boost of 635 km s^{-1}, which demonstrates the purely kinematic dipole interpretation. Again, the *left-hand* panel (a) shows the dipole C_1 variation, while the *right-hand* panel (b) shows the quadrupole C_2 variation. The bands of each distribution indicate the 65% and 95% confidence intervals obtained from the mock sampling.

likely be required to reinterpret the conclusions of BNW.

To further assess the influence of the incorrect routine on the results, we also considered the effects on the CMB dipole and Hubble expansion anisotropy individually. The ray tracing routines are executed at two distinct stages of the simulation. The first stage is when the CMB sky of the Szekeres observer is generated (step 1 of section 3.3), and the second stage is when the COMPOSITE dataset is ray traced following an alignment to the generated CMB dipole (step 3 of section 3.3). However, we find that regardless of whether the CMB is correctly or incorrectly ray traced, the difference in the alignment of the CMB dipole axis has a minimal effect on the subsequent determination of the Hubble expansion anisotropy. Therefore, the majority of the observed differences in the BNW and now corrected results shown in fig. 4.1 is due to whether or not the initial null vectors were correctly normalised when ray tracing each point in the COMPOSITE dataset, with the prior ray tracing of the CMB making minimal impact.

In order to fully test the kinematic dipole hypothesis in the same fashion as BNW, we display the Hubble expansion anisotropy of the COMPOSITE dataset itself, as well as for mock COMPOSITE catalogues with FLRW redshifts transformed by a 635 km s^{-1} local boost. These results are presented in figure 4.2 for both the dipole and quadrupole anisotropy. While the incorrect BNW results provide a match to the low redshift dipole anisotropy of the COMPOSITE dataset by design, the corrected results are almost three times larger.

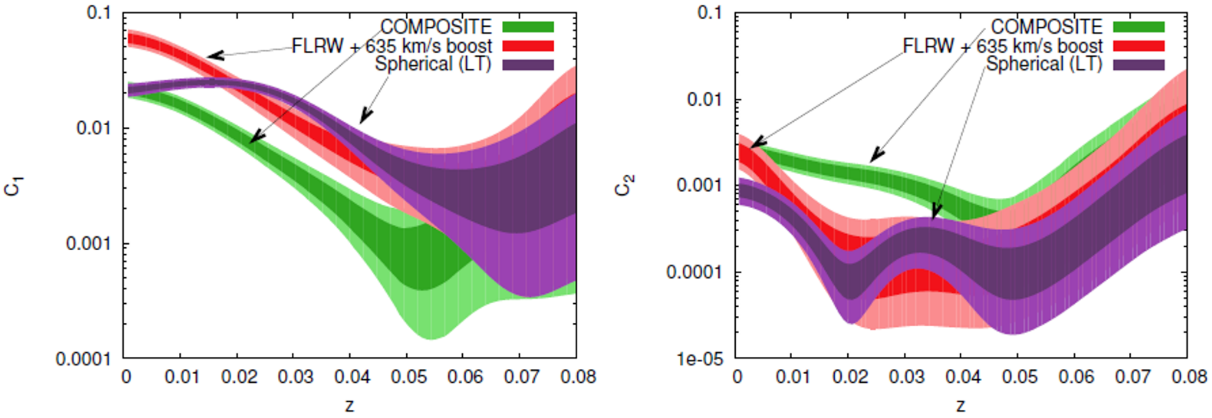

Figure 4.3: The Hubble expansion anisotropy of the COMPOSITE dataset and mock FLRW catalogues as compared with the mock catalogues for an LTB model with $\alpha = 0$, $\delta_0 = -0.95$ $r_0 = 45.5\,h^{-1}\,\mathrm{Mpc}$ and $\Delta r = 4.55\,h^{-1}\,\mathrm{Mpc}$, and an observer position of $(r_{\rm obs}, \theta_{\rm obs}, \phi_{\rm obs}) = \left(28\,h^{-1}\,\mathrm{Mpc}, \pi/2, \pi/2\right)$. Image credit: BNW [1]

Intriguingly, the corrected results are a closer match to the FLRW mocks with a local boost over the whole redshift range. The closeness of this fit is all the more surprising when we compare the result found by BNW for the LTB model fine-tuned to match the Hubble variance dipole of the COMPOSITE dataset at $z = 0$, as we reproduce in fig. 4.3. In that case, the redshift dependence of the dipole is quite different, only approaching the mock FLRW samples at larger values of z. BNW argued that this is the result of an effective point symmetry along the axis connecting the off-centre observer to the centre of the void. It would appear that the axis defined by the matter dipole in the Szekeres model gives a similar effect, producing a Hubble variance dipole which is numerically closer to the ordinary kinematic term on top of an FLRW model when fit to the CMB dipole anisotropy in the LG frame. Evidently, for particular observer positions the Szekeres model can be degenerate with models for which the usual kinematic interpretation applies.

As for the quadrupole variation of fig. 4.2, none of the mock samples – or even the boosted FLRW dataset for that matter – reproduce the variation seen in the COMPOSITE dataset. This was also noted in the results of BNW, where it was again suggested that a more complex Szekeres may be required to obtain more precision in the quadrupole determination.

4.1.2 Varying the Observer Position

In addition to determining the Hubble expansion anisotropy measured by the 'best-fit' observer at $(r_{\rm obs}, \theta_{\rm obs}, \phi_{\rm obs}) = (25\,h^{-1}\,\mathrm{Mpc}, 0.705\,\pi, 0.5\,\pi)$, we further explore the observed anisotropy measured by observers throughout our Szekeres model. Fig. 4.4 shows the CMB observed dipole and quadrupole variation with the observer position, with the crosses marking the position of our 'best-fit' observer who measures the same CMB dipole as us. The amplitudes of both the dipole and quadrupole can be seen to increase as the observer is positioned closer to the $X = 0$ axis, which is interior the void region of the model. This increasing amplitude roughly corresponds to the region in panel (a)[1] of fig. 3.1, where the gradient of the transition between the over-density and the under-dense void region is greatest. The CMB quadrupole amplitude can also be seen to vary with much greater sensitivity to the observer position than the dipole. However, for this particular parametrisation of the Szekeres model, the maximum observable CMB quadrupole is still an order of magnitude smaller than what is actually observed.

In fig. 4.5, the dipole and quadrupole moments of the spherically averaged Hubble expansion anisotropy are shown for variations of the observer position at $z = 0$. While the redshift dependence of the Hubble anisotropy closely resembles that of the CMB dipole in fig. 4.4, the Hubble quadrupole anisotropy displays a far more complex pattern of positional variation within the central void region of the model compared to the CMB quadrupole. Also shown in fig. 4.5 is the fractional variation in the amplitude of the Hubble dipole $\delta H_0 = \big(H_0 - \bar{H}_0\big)/\bar{H}_0$ from that of the background FLRW expansion. Observers interior to the void and deep within the Szekeres over-density measure up to an almost 30% difference in the Hubble expansion rate, with a difference of 22% observed at the location of the observer whose CMB dipole matches our own.

Furthermore, we also consider the angular separation between the Hubble expansion dipole and the CMB dipole as a function of the observer position in fig. 4.6. If the maximum of the temperature dipole anisotropy coincides exactly with the minimum of the Hubble expansion dipole anisotropy, then the angular separation will be 180°. We do expect a close correlation of this sort[2], and indeed this is what is found. The observer whose CMB dipole matches our own (indicated by the cross in fig. 4.6) measures a separation of $\sim 162^\circ$ between their observed Hubble expansion dipole and the CMB dipole at $(l, b) = (276.4^\circ,\ 29.3^\circ)$ as observed in the Local Group frame.

---

[1] The plotting of figs. 4.4, 4.5 and 4.6 does not include the shell shifting effect that was demonstrated in fig. 3.1. This is because the compression of the Szekeres shells along the $+Z$ direction squashes the detail in the anisotropy distribution beyond readability. One should therefore compare the anisotropy distributions with panel (a) of fig. 3.1, which gives the density distribution of the Szekeres model without the shell shifting correction.

[2] Consider a simple linear Hubble law of the form $cz = H_0 r$. For fixed r, an additional small blueshift will increase the CMB temperature while decreasing the value of z and the inferred value of H_0.

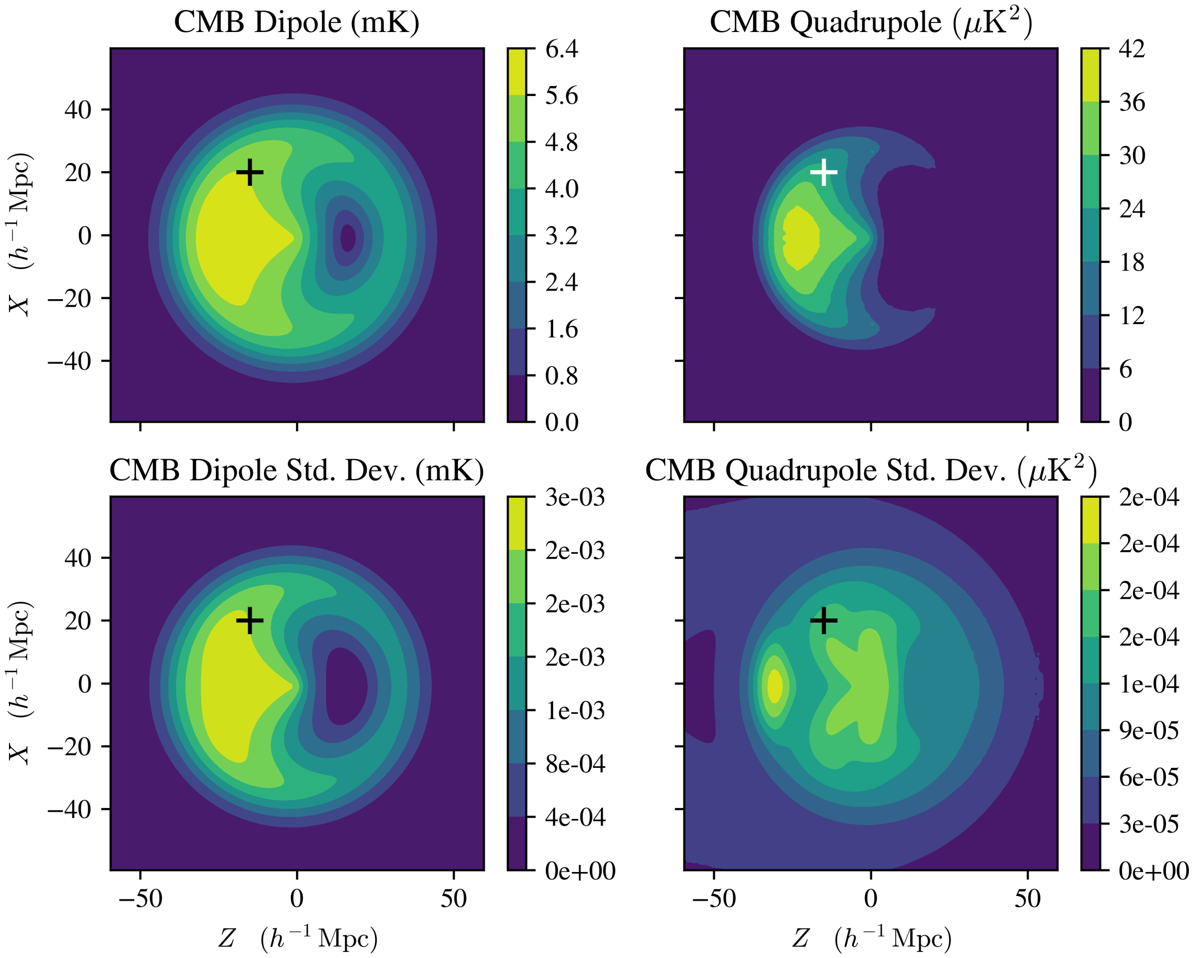

Figure 4.4: Corrected BNW base model: The CMB dipole and quadrupole amplitude (as well as the standard deviation for each) are shown as a function of the observer position. In each panel, the position of the observer whose CMB dipole matches our own, with the coordinates (3.8), is indicated by a cross. Note: these plots do not take the shell shifting effects into account.

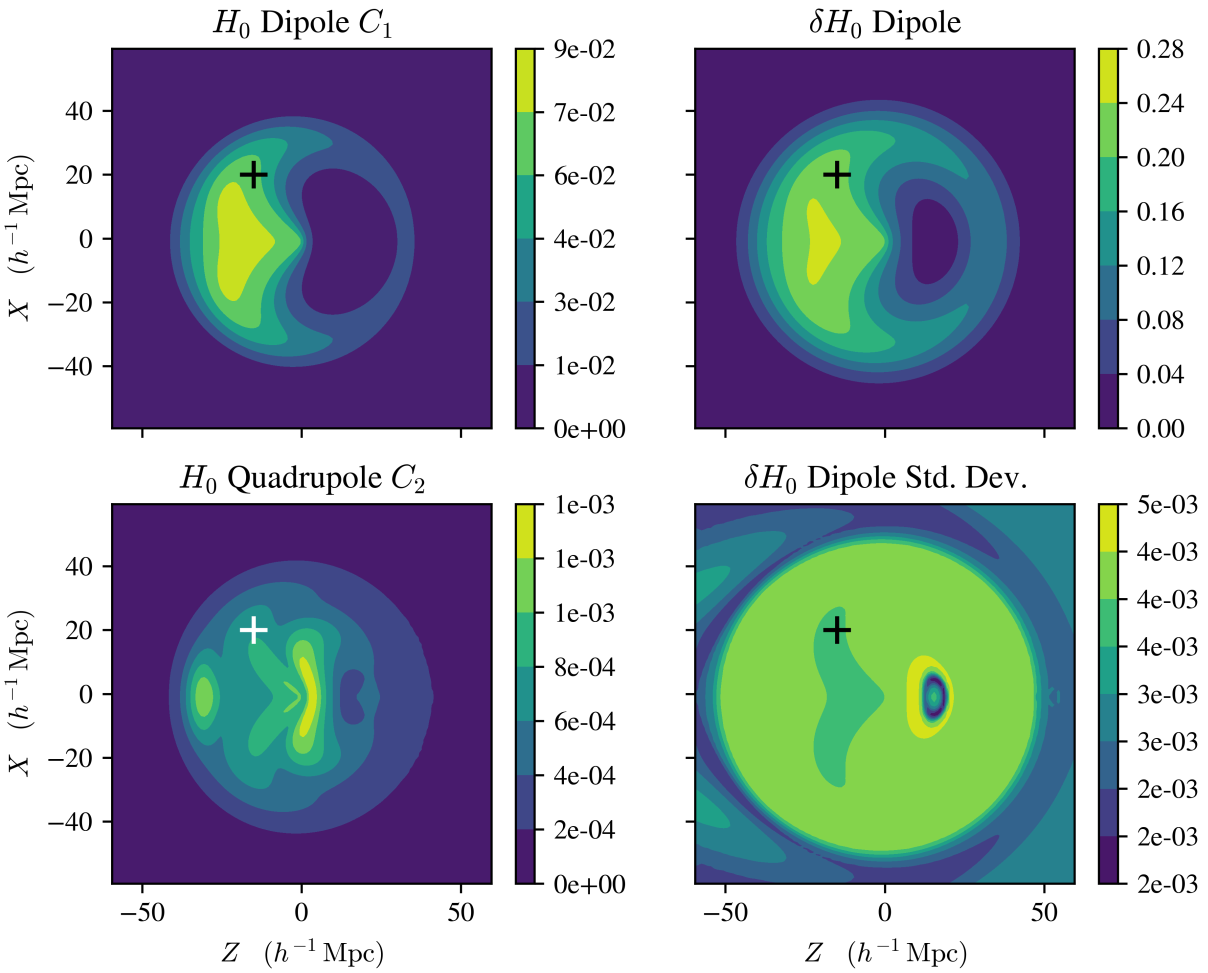

Figure 4.5: Corrected BNW base model: The amplitude of the dipole and quadrupole anisotropies in the variation of H_0 are shown as a function of the observer position at $z = 0$. Also shown is the fractional variation $\delta H_0 = \left(H_0 - \bar{H}_0\right)/\bar{H}_0$ in the amplitude of the Hubble expansion dipole from the background FLRW expansion. In each panel, the position of the observer whose CMB dipole matches our own, with the coordinates (3.8), is again indicated by a cross. Note: these plots do not take the shell shifting effects into account.

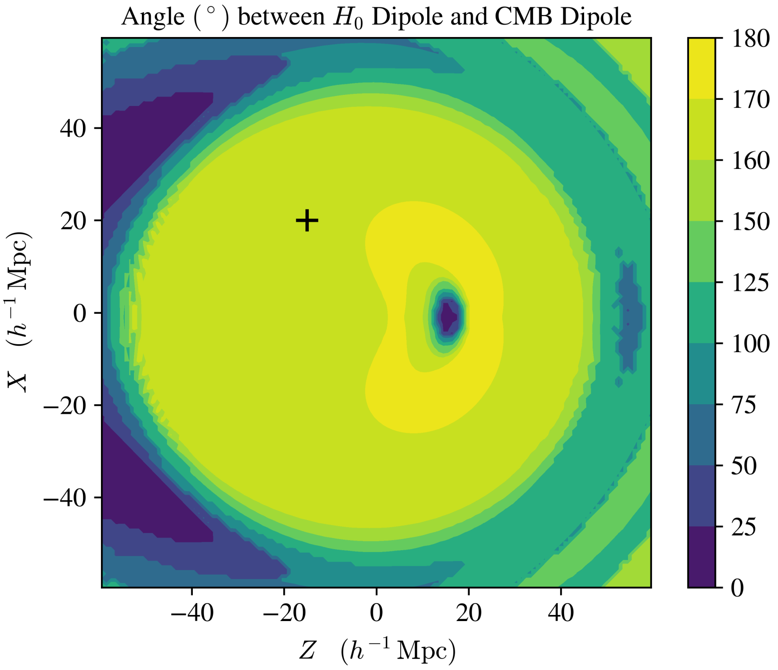

Figure 4.6: The angular separation (in degrees) between the Hubble expansion dipole and the CMB dipole as a function of the observer position. The position of the observer whose CMB dipole matches our own is again indicated by a cross. Note: this plot does not take the shell shifting effects into account.

4.2 Inclusion of Haantjes Transformations

The Szekeres model of BNW needs to be modified to account for the Hubble expansion anisotropy of the COMPOSITE dataset. We are interested in using the Haantjes transformations described in section 2.2.5 as a systematic means of creating Szekeres models with more observationally realistic characterisations of differential expansion. Because these transformations can be simply parametrised in terms of the three position variables (ϑ, φ, r_l), before being applied to our original axially symmetric Szekeres model, they allow for minor adjustments to the density dipole while leaving the parameters (3.7) and (3.8) fixed.

In fig. 4.7, we explore the effects that applying various Haantjes transformations have on the density of our Szekeres model (which was shown in fig. 3.1). We have opted to include the effects of Szekeres shell shifting in this figure (see section 2.2.4), as the density distribution will be smeared out with the relative shell rotations induced by having $P'(r)$ and $Q'(r)$ non-zero. The transformations demonstrated in fig. 4.7 are produced using combinations of $\vartheta = -\pi/16, -\pi/8, -\pi/4$ and $r_l = 0.1\,h^{-1}, 1\,h^{-1}, 2\,h^{-1}$ Mpc with $\varphi = 0$. The angles (ϑ, φ) correspond to the new positioning of over-density measured at the minimum radial location of the anisotropy r_l, which then transform the Szekeres dipole functions (2.63) via (2.65).

Modifying the dipole functions (P, Q, S) through (2.63) can be interpreted as modifying (2.44) by including additional terms. The form of $\mathcal{E}'/\mathcal{E}$ under a Haantjes transformation becomes

$$\left(\frac{\mathcal{E}'}{\mathcal{E}}\right)_{\text{Haan}} = -\frac{S'\cos\theta + N\sin\theta}{S} - \frac{2(D_1\cos\phi + D_2\sin\phi)\,B\sin\theta}{S} + \frac{T'}{T}\left[\cos\theta + \frac{((P + D_1\,A)\cos\phi + (Q + D_2\,A)\sin\phi)\sin\theta}{S}\right], \tag{4.1}$$

where $N(r, \phi) \equiv (P'\cos\phi + Q'\sin\phi)$ as before, $T(r)$ is defined by (2.64) and

$$A(r) = P^2 + Q^2 + S^2\,, \qquad B(r) = PP' + QQ' + SS'\,. \tag{4.2}$$

As (4.1) will multiply the mass function $M(r)$ in the numerator of the Szekeres density (2.48), as well as the factor of R^3 in denominator, there will be a proportional change in the density distribution depending on the magnitude of the Haantjes transformation parameters. As the values of D_1 and D_2 determined by (2.65) vary exponentially in terms of $-S(r_l)$, values of r_l that are a significant fraction of the void size r_0 will decrease the overall size of the Haantjes transformation.

The Haantjes transformation angle ϑ of (2.65) can be seen to induce an angular shifting and smearing of the density dipole about the origin. As the size of this angle increases towards $-\pi/4$, the amount by which the dipole over-density is dragged towards its new location also increases. For the smallest shown angle of $\vartheta = -\pi/16$ with $r_l = 2\,h^{-1}\,\text{Mpc}$, the density deviates minimally from its untransformed distribution shown in panel (b) of fig. 3.1. Decreasing the anisotropy parameter r_l from $r_l = 2\,h^{-1}\,\text{Mpc}$ down to $r_l = 0.1\,h^{-1}\,\text{Mpc}$ results in a broadening of the dipole over-density in the radial direction. For values of r_l approaching the characteristic void size r_0, one finds that the ray traced CMB dipole tends to its unmodified amplitude, which is the minimum obtainable value when performing these Haantjes transformations.

To further explore the effect that performing a small Haantjes transformation has on the Hubble expansion anisotropy, we trialled various combinations of Haantjes parameters on the base Szekeres model of section 3.1.3. In fig. 4.8, we show the results of a Haantjes transformation where we have set $(\vartheta,\ \varphi,\ r_l) = (\pi/16,\ 0\pi,\ 10\,h^{-1}\,\text{Mpc})$ in (2.65), in order to modify $S(r)$, $P(r)$ and $Q(r)$ in the model according to (2.63). Although this particular parametrisation is found to yield a slightly higher CMB dipole amplitude of $\Delta T_d = 7.22\,\text{mK}$, the quadrupole amplitude increases excessively to $\mathcal{D}_2 \simeq 20 \times 10^6\,\mu\text{K}^2$. Nevertheless, the distribution of the Hubble expansion anisotropy under the transforma-

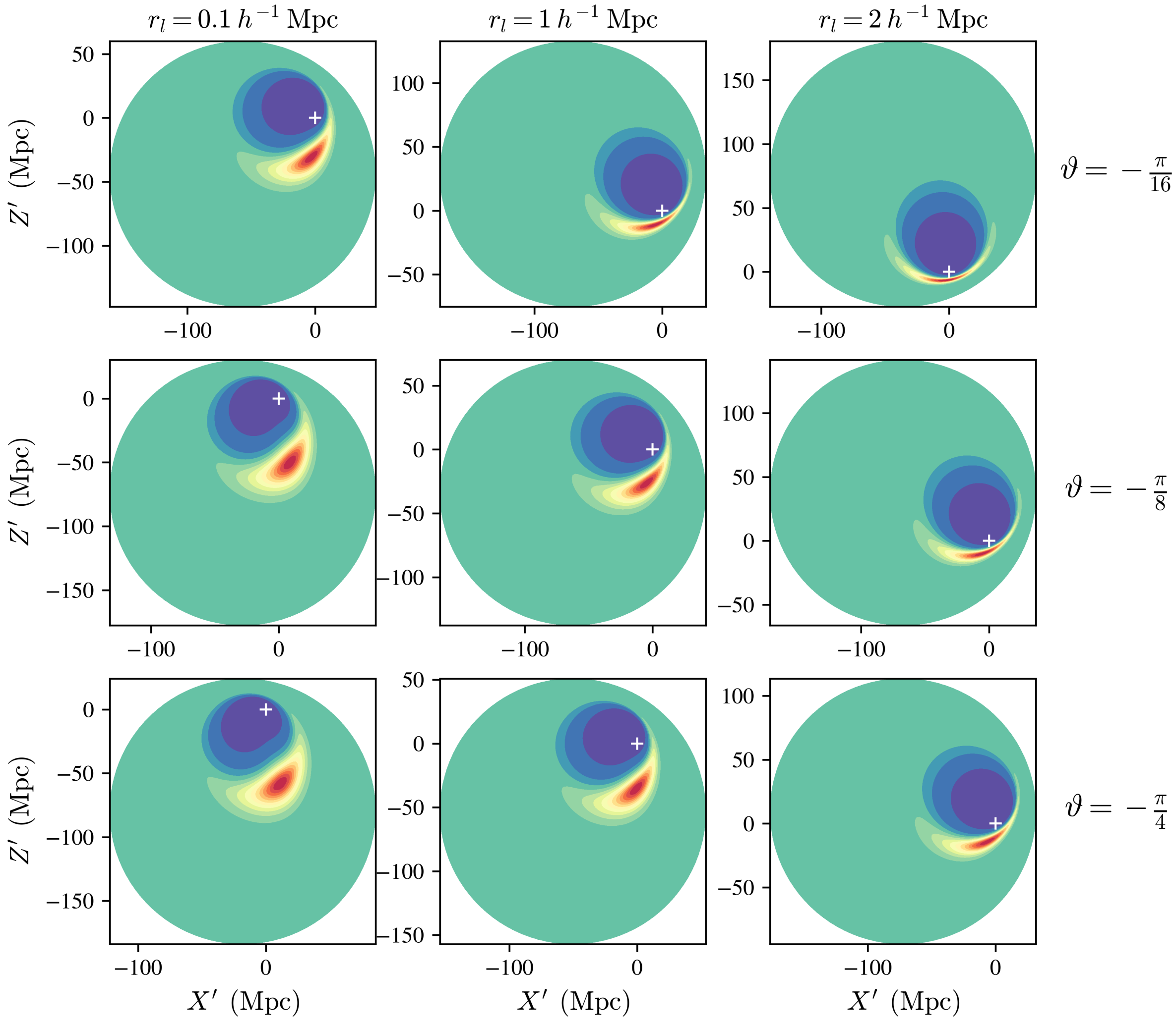

Figure 4.7: The density of the axially symmetric Szekeres model shown in fig. 3.1 under various Haantjes transformations (following the methodology detailed in section 2.2.5), with crosses marking the origin point $(X', Z') = (0, 0)$. Note: in these density plots the effects of shell shifting and rotation are included. In each case, r_l is specified at the top of each column in units of h^{-1} Mpc where $h = 0.673$.

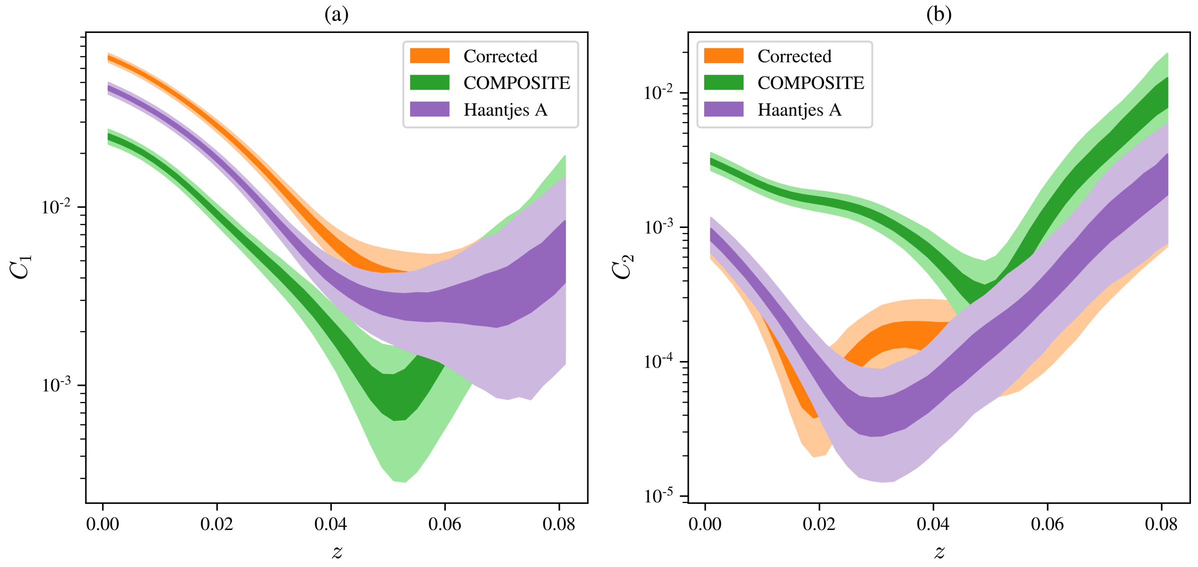

Figure 4.8: The effect of performing a small Haantjes transformation (denoted here as ‘Haantjes A’) on the Hubble expansion anisotropy. The base, axially symmetric Szekeres model defined in section 3.1.3 is maintained, with the Haantjes transformation applied through specifying the parameters $(\vartheta, \varphi, r_l)$ of (2.65) and modifying $S(r)$, $P(r)$ and $Q(r)$ according to (2.63). To obtain Haantjes A, the Haantjes parameters were set $(\vartheta,\, \varphi,\, r_l) = \big(\pi/16,\, 0\pi,\, 10\, h^{-1}\,\text{Mpc}\big)$, before the COMPOSITE dataset was ray traced using the corrected null vector initialisation routine.

tion shifts downwards in magnitude towards the COMPOSITE anisotropy. This suggests that performing a Haantjes transformation to correct the Hubble expansion anisotropy to match that of COMPOSITE, while simultaneously matching the CMB dipole and quadrupole anisotropies, is very non-trivial. Clearly a grid search is required – however, given the number of free parameters to be varied, it is a task that really requires parallel processing on a high-performance machine.

The particular Haantjes transformation applied to obtain the results in fig. 4.8 is actually miniscule when compared to the density of the untransformed Szekeres model. In fig. 4.9, the resultant density of the ‘Haantjes A’ transformation is shown with a line tracing the shifts of each Szekeres shell. The deviation of this line from the $X' = 0$ plane is barely perceptible, with a slight gradient of approximately 2.2×10^{-4}. This illustrates just how sensitive the ray tracing results are to small model changes.

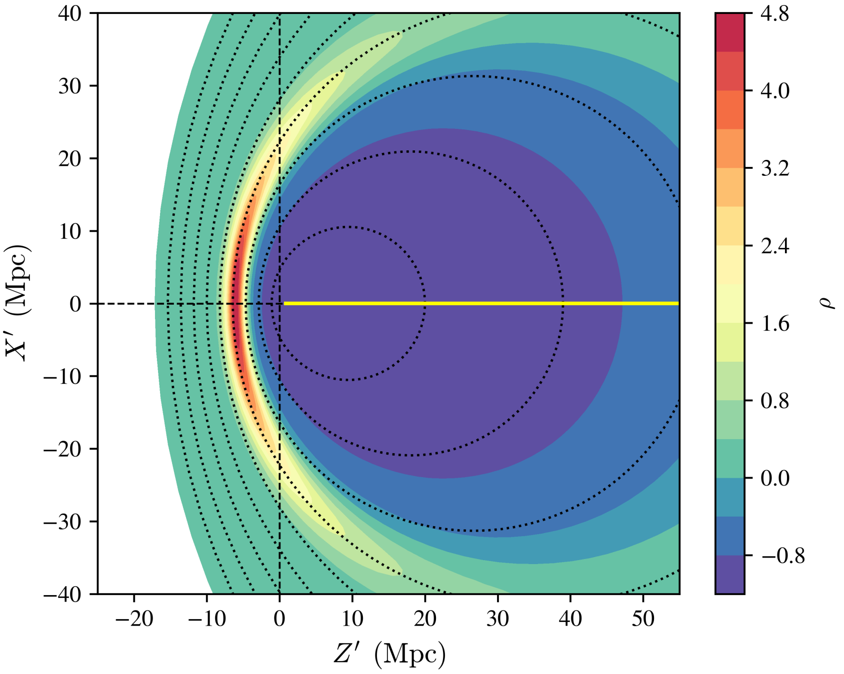

Figure 4.9: The density of the base Szekeres model with a Haantjes transformation of $(\vartheta, \varphi, r_l) = (\pi/16,\, 0\pi,\, 10\,h^{-1}\,\mathrm{Mpc})$, which we refer to as 'Haantjes A' in fig. 4.8. The yellow line tracks the shifts in position of $\theta = 0$ on each shell, although its deviation from $Z' = 0$ axis is virtually imperceptible. Note: the density in this figure is plotted including the shell shifting and rotation effects.

Chapter 5

Conclusion

By performing ray tracing analyses with Szekeres cosmological models, we have characterised the influence that local inhomogeneities have on the spherically averaged Hubble expansion on $\lesssim 150\,h^{-1}\,\mathrm{Mpc}$ scales. We found that correcting an erroneous null vector initialisation routine, first noted by Dam [107], significantly modified the reported Hubble expansion anisotropy. Once corrected, the spherically averaged Hubble expansion anisotropy (presented in fig. 4.1) is nearly three times as large as that reported by BNW at redshifts $z \lesssim 0.04$, although the distribution retains much the same shape. Since the particular Szekeres model parameters had been best fit to match the local Hubble expansion anisotropy of the COMPOSITE dataset with a critical error in the code, clearly the parameters of the model have to be readjusted to fulfil the original aims of BNW, if it is indeed at all possible. In this thesis, we have taken further steps towards this goal.

Firstly, we explored the effects of repositioning the observer within the axially symmetric Szekeres model with the parameters specified by BNW. While we indeed observed variations of the amplitude of the dipole and quadrupole moments consistent with the Szekeres structures and the relative position of the observer, a simple repositioning of the observer did not improve the match to the COMPOSITE data anisotropy. Not only must the observed CMB dipole remain consistent for a repositioned observer, but the position itself must be consistent with respect to the local structures.

As was also noted by both BNW and Dam [107], the CMB quadrupole amplitude obtained in the ray traced Szekeres model is an order of magnitude smaller than actually observed in the CMB. From fig. 4.4, it is evident that the CMB quadrupole amplitude is fairly sensitive to the observer position, although its maximum possible value on the interior of the void is still much lower than the observed expectation. Similarly, for the quadrupole of the Hubble expansion anisotropy shown in fig. 4.5, the ray traced results are considerably smaller than observed for COMPOSITE.

Unfortunately, a re-parametrisation of our Szekeres model is expected to be computationally expensive, as there are a total of seven free parameters to be explored. Only five of these parameters (α, r_0, δ_0, $r_{\rm obs}$, $\theta_{\rm obs}$) were actively varied by BNW, with $\phi_{\rm obs} = 0.5\,\pi$ and $\Delta r = 0.1\,r_0$ set to simplify down the parameter space. In the limit of keeping with the axially symmetric Szekeres model with only $S'(r) \neq 0$, it is conceivable to perform a much more rigorous parameter space search that includes the variation of all seven free variables. However, this is assuming that a satisfactory parameter set is obtainable in what is a relatively simplistic Szekeres model.

Szekeres models that are non-axially symmetric, or that have $P'(r) \neq 0$ and/or $Q'(r) \neq 0$, have been previously studied by Bolejko [121]. In such cases, one must decide on appropriate parametrisations of both $P(r)$ and $Q(r)$ that produce a consistent, viable form of the model. This is especially the case when the model is non-axially symmetric, which could further complicate the numerical integration of geodesics within our simulations. Since performing a suitable Haantjes transformation relocates the density dipole of the model while automatically ensuring $P(r)$, $Q(r)$ and $S(r)$ jointly satisfy the axial symmetry conditions, it could further prove useful in applying minor model adjustments.

Beyond a much needed re-parametrisation of the Szekeres model, it could be the case that a simple dipole density distribution lacks the required complexity to successfully capture the quadrupole moments of both the CMB and Hubble expansion anisotropy [1]. One could further investigate adding more complex structures into the Szekeres model, e.g. by creating elaborate networks of evolving density extrema, as is demonstrated in depth by Sussman and collaborators [122, 123]. This particular approach considers Szekeres models in terms of covariant scalars, whose extrema can be positioned almost arbitrarily in terms of spherical coordinates. One such covariant scalar is the density of the Szekeres model, with its maxima and minima physically corresponding to the over-densities and under-densities within the model. Moreover, as these density extrema are not comoving with the FLRW background, they intuitively express deviations from the FLRW expansion e.g., in terms of their peculiar velocities.

Over the past few years, numerous investigations into bulk flows, number count dipoles and differing notions of scales of statistical homogeneity have fuelled interest in the potential observational effects linked to local inhomogeneities and expansion rate variations. However, as the previous examinations of the spherically averaged Hubble anisotropy of *Cosmicflows-II* have demonstrated [101, 124], many of these investigations may still have to contend with persisting systematics and biases. Nonetheless, it could still prove insightful to explore their results as interpreted in an inhomogeneous cosmological model.

In light of ongoing interest and debate concerning the non-kinematic nature of the dipole in number counts of quasars and other distant radio galaxy samples [95, 97, 125], it is very important to perform a similar ray tracing analysis to that of this thesis for datasets such as the 1.36 million CatWISE quasar sample of Secrest *et al.* [95]. This dataset has a far larger mean redshift of $z = 1.2$ compared to COMPOSITE's mean redshift of $z = 0.02$. Such an endeavour would require that we first determine Szekeres models which can realistically reproduce the local Hubble expansion variance seen in low redshift samples such as COMPOSITE.

Finally, there is the potential for new insights into the effects of local inhomogeneity and anisotropy by considering more generalised forms of the luminosity distance-redshift expansion (1.11). A promising approach is that of Heinesen [120, 126], who has developed a low-redshift cosmographic expansion allowing for anisotropies of the sort we model with exact solutions. Heinesen's formalism makes very few assumptions – in particular, no field equations are prescribed. It makes the minimal assumptions that timelike observer congruences, as well as null geodesics obey equations of geodesic deviation equations governed by the Riemann curvature tensor, as in general relativity. Consequently the Sachs optical equation (1.37) can be applied along with additional equations which describe the evolution of the light ray bundle, and of the observer congruence. In addition, the formalism does not apply to observer congruences which are contracting – which would give rise to the problems of shell-crossing etc. In the presence of local inhomogeneities, there will, in general, be additional terms to the usual FLRW cosmographic coefficients in (1.11). Furthermore, since Heinesen's approach is background independent, quantities such as the deceleration parameter are redefined from first principles.

Significantly, the coefficients of the formalism devised by [120] can be directly tested by measurements with sufficiently large cosmological datasets, such as will become available in the next two decades. The possibilities for general relativistic predictions are already under investigation within large scale numerical relativity simulations. For example, working with dust models which evolve on average as an Einstein–de Sitter model, Macpherson & Heinesen [127] find a 0.6% cosmic variance in the 'effective' observed Hubble parameter coarse–grained on very large scales of $200\,h^{-1}\,$Mpc. It would thus be both interesting and complementary to examine the generalised luminosity distance expansion on the $\lesssim 150\,h^{-1}\,$Mpc scales that our ray tracing simulations probe. In particular, in combination with Szekeres model ray tracing, Heinesen's formalism may be useful for definitively characterising relativistic differential expansion.

Overall, the research into ray traced Szekeres models and the Hubble expansion anisotropy undertaken in this thesis has yielded many new lines of inquiry to be explored in future work. It is hoped that by increasing the sophistication of our ray tracing simulations within more complex Szekeres models, we can better characterise the inhomogeneities and anisotropies present in our local universe – using the full advantages of our general relativistic approach. Furthermore, with the anticipated increase in both the precision and volume of full sky surveys over the next decade, it is desirable that the inference of cosmological results becomes less constrained by the various model assumptions involved in analysing the data. Analyses of the kind performed in this thesis will potentially further our progress towards this goal.

Bibliography

[1] K. Bolejko, M. A. Nazer, and D. L. Wiltshire, "Differential Cosmic Expansion and the Hubble Flow Anisotropy", Journal of Cosmology and Astroparticle Physics 06, 035 (2016).

[2] A. Einstein, "Kosmologische Betrachtungen Zur Allgemeinen Relativitätstheorie", Sitzungsberiche der Preussischen Akademie der Wissenschaften (Berlin), 142–152 (1917), [English translation: *"The collected papers of Albert Einstein. Vol.* **6***"* (Princeton Univ. Press, 1997) pp. 421–432].

[3] E. A. Milne, "World Structure and the Expansion of the Universe", Nature **130**, 9–10 (1932).

[4] D. L. Wiltshire, P. R. Smale, T. Mattsson, and R. Watkins, "Hubble Flow Variance and the Cosmic Rest Frame", Physical Review D **88**, 083529 (2013).

[5] D. L. Wiltshire, "Cosmic Clocks, Cosmic Variance and Cosmic Averages", New Journal of Physics **9**, 377–377 (2007).

[6] M. Giovannini, *A Primer On The Physics Of The Cosmic Microwave Background* (World Scientific Publishing Company, Singapore, 2008).

[7] S. W. Hawking and G. F. R. Ellis, *The Large Scale Structure of Space-Time* (Cambridge University Press, Cambridge, United Kingdom, 1973).

[8] G. W. Gibbons, *Phantom Matter and the Cosmological Constant*, (Feb. 2003) `http://arxiv.org/abs/hep-th/0302199`.

[9] A. Einstein and W. de Sitter, "On the Relation Between the Expansion and the Mean Density of the Universe", Proc. Nat. Acad. Sci. **18**, 213–214 (1932).

[10] S. Weinberg, *Cosmology* (Oxford University Press, Oxford, United Kingdom, 2008).

[11] N. Aghanim, Y. Akrami, M. Ashdown, et al. (Planck), "*Planck* 2018 Results: VI. Cosmological Parameters", Astronomy & Astrophysics **641**, A6 (2020).

[12] W. de Sitter, "Einstein's theory of gravitation and its astronomical consequences. Third paper", Monthly Notices of the Royal Astronomical Society **78**, 3–28 (1917).

[13] S. Weinberg, “The cosmological constant problem”, Reviews of Modern Physics **61**, 1–23 (1989).

[14] B. Ratra and P. J. E. Peebles, “Cosmological Consequences of a Rolling Homogeneous Scalar Field”, Physical Review D **37**, 3406 (1988).

[15] R. R. Caldwell, R. Dave, and P. J. Steinhardt, “Cosmological imprint of an energy component with general equation of state”, Physical Review Letters **80**, 1582–1585 (1998).

[16] E. J. Copeland, M. Sami, and S. Tsujikawa, “Dynamics of Dark Energy”, International Journal of Modern Physics D **15**, 1753–1935 (2006).

[17] D. J. Fixsen, “The Temperature of the Cosmic Microwave Background”, Astrophysical Journal **707**, 916–920 (2009).

[18] D. J. Fixsen, E. S. Cheng, J. M. Gales, et al., “The Cosmic Microwave Background Spectrum from the Full COBE/FIRAS Data Set”, Astrophysical Journal **473**, 576–587 (1996).

[19] N. Aghanim, C. Armitage-Caplan, M. Arnaud, et al. (Planck), “Planck 2013 Results. XXVII. Doppler Boosting of the CMB: Eppur Si Muove”, Astronomy & Astrophysics **571**, A27 (2014).

[20] P. J. E. Peebles and D. T. Wilkinson, “Comment on the Anisotropy of the Primeval Fireball”, Physical Review **174**, 2168–2168 (1968).

[21] R. M. Sullivan and D. Scott, *The CMB Dipole: Eppur Si Muove*, (Nov. 23, 2021) `http://arxiv.org/abs/2111.12186`.

[22] W. T. Hu, “Wandering in the Background: A CMB Explorer”, PhD thesis (UC Berkeley, Aug. 1995).

[23] R. K. Sachs and A. M. Wolfe, “Perturbations of a cosmological model and angular variations of the microwave background”, Astrophysical Journal **147**, 73–90 (1967).

[24] M. J. Rees and D. W. Sciama, “Large scale Density Inhomogeneities in the Universe”, Nature **217**, 511–516 (1968).

[25] Y. B. Zel’dovich and R. A. Sunyaev, “The interaction of matter and radiation in a hot-model universe”, Astrophysics and Space Science **4**, 301–316 (1970).

[26] R. A. Sunyaev and Y. B. Zel’dovich, “Small-scale fluctuations of relic radiation”, Astrophysics and Space Science **6**, 358–376 (1970).

[27] J. P. Ostriker and E. T. Vishniac, “Generation of microwave background fluctuations from nonlinear perturbations at the ERA of galaxy formation”, Astrophysical Journal Letters **306**, L51–L54 (1986).

[28] C. L. Bennett, A. Banday, K. M. Gorski, et al., "Four year COBE DMR cosmic microwave background observations: Maps and basic results", Astrophysical Journal Letters **464**, L1–L4 (1996).

[29] P. de Bernardis, P. A. R. Ade, J. J. Bock, et al., "A flat Universe from high-resolution maps of the cosmic microwave background radiation", Nature **404**, 955–959 (2000).

[30] S. Hanany, P. Ade, A. Balbi, et al., "MAXIMA-1: A Measurement of the Cosmic Microwave Background Anisotropy on Angular Scales of 10'-5°", Astrophysical Journal Letters **545**, L5–L9 (2000).

[31] C. B. Netterfield, P. A. R. Ade, J. J. Bock, et al., "A Measurement by BOOMERANG of Multiple Peaks in the Angular Power Spectrum of the Cosmic Microwave Background", Astrophysical Journal **571**, 604–614 (2002).

[32] A. J. Banday, K. M. Gorski, L. Tenorio, et al., "On the RMS Anisotropy at 7 degrees and 10 degrees in the COBE-DMR Two-Year Sky Maps", Astrophysical Journal Letters **436**, L99–L102 (1994).

[33] D. N. Spergel, L. Verde, H. V. Peiris, et al. (WMAP), "First year Wilkinson Microwave Anisotropy Probe (WMAP) observations: Determination of cosmological parameters", Astrophysical Journal Supplement Series **148**, 175–194 (2003).

[34] C. Copi, D. Huterer, D. Schwarz, and G. Starkman, "The Uncorrelated Universe: Statistical Anisotropy and the Vanishing Angular Correlation Function in WMAP Years 1-3", Physical Review D **75**, 023507 (2007).

[35] A. Gruppuso, "Two-point correlation function of Wilkinson Microwave Anisotropy Probe 9-yr data", Monthly Notices of the Royal Astronomical Society **437**, 2076–2082 (2014).

[36] P. A. R. Ade, N. Aghanim, C. Armitage-Caplan, et al. (Planck), "Planck 2013 results. XXIII. Isotropy and statistics of the CMB", Astronomy & Astrophysics **571**, A23 (2014).

[37] P. A. R. Ade, N. Aghanim, Y. Akrami, et al. (Planck), "Planck 2015 results. XVI. Isotropy and statistics of the CMB", Astronomy & Astrophysics **594**, A16 (2016).

[38] Y. Akrami, M. Ashdown, J. Aumont, et al. (Planck), "Planck 2018 Results. VII. Isotropy and Statistics of the CMB", Astronomy & Astrophysics **641**, A7 (2020).

[39] C. J. Copi, D. Huterer, D. J. Schwarz, and G. D. Starkman, "Lack of large-angle TT correlations persists in WMAP and Planck", Monthly Notices of the Royal Astronomical Society **451**, 2978–2985 (2015).

[40] D. J. Schwarz, C. J. Copi, D. Huterer, and G. D. Starkman, "CMB Anomalies after Planck", Classical and Quantum Gravity **33**, 184001 (2016).

[41] M. Tegmark, A. de Oliveira-Costa, and A. Hamilton, "A high resolution foreground cleaned CMB map from WMAP", Physical Review D **68**, 123523 (2003).

[42] H. K. Eriksen, A. J. Banday, K. M. Gorski, F. K. Hansen, and P. B. Lilje, "Hemispherical power asymmetry in the three-year Wilkinson Microwave Anisotropy Probe sky maps", Astrophysical Journal Letters **660**, L81–L84 (2007).

[43] J. Hoftuft, H. K. Eriksen, A. J. Banday, et al., "Increasing evidence for hemispherical power asymmetry in the five-year WMAP data", Astrophysical Journal **699**, 985–989 (2009).

[44] D. J. Schwarz, G. D. Starkman, D. Huterer, and C. J. Copi, "Is the low-l microwave background cosmic?", Physical Review Letters **93**, 221301 (2004).

[45] A. de Oliveira-Costa, M. Tegmark, M. Zaldarriaga, and A. Hamilton, "The Significance of the Largest Scale CMB Fluctuations in WMAP", Physical Review D **69**, 063516 (2004).

[46] K. Land and J. Magueijo, "The Axis of Evil", Physical Review Letters **95**, 071301 (2005).

[47] K. Land and J. Magueijo, "The Axis of Evil Revisited", Monthly Notices of the Royal Astronomical Society **378**, 153–158 (2007).

[48] C. J. Copi, D. Huterer, D. J. Schwarz, and G. D. Starkman, "On the Large-Angle Anomalies of the Microwave Sky", Monthly Notices of the Royal Astronomical Society **367**, 79–102 (2006).

[49] J. Kim and P. Naselsky, "Anomalous Parity Asymmetry of the Wilkinson Microwave Anisotropy Probe Power Spectrum Data at Low Multipoles", Astrophysical Journal Letters **714**, L265–L267 (2010).

[50] J. Kim and P. Naselsky, "Anomalous Parity Asymmetry of WMAP Power Spectrum Data at Low Multipoles: Is it Cosmological or Systematics?", Physical Review D **82**, 063002 (2010).

[51] M. Cruz, L. Cayon, E. Martinez-González, P. Vielva, and J. Jin, "The Non-Gaussian Cold Spot in the 3 Year Wilkinson Microwave Anisotropy Probe Data", Astrophysical Journal **655**, 11–20 (2007).

[52] A. Kovács, N. Jeffrey, M. Gatti, et al., "The DES view of the Eridanus supervoid and the CMB cold spot", Monthly Notices of the Royal Astronomical Society **510**, 216–229 (2022).

[53] S. M. Carroll, "The Cosmological Constant", Living Reviews in Relativity **4**, 1 (2001).

[54] M. Rameez and S. Sarkar, "Is there really a Hubble tension?", Classical and Quantum Gravity **38**, 154005 (2021).

[55] G. F. R. Ellis, R. Maartens, and M. A. H. MacCallum, *Relativistic Cosmology* (Cambridge University Press, Cambridge, United Kingdom, 2012).

[56] A. G. Riess, S. Casertano, W. Yuan, L. M. Macri, and D. Scolnic, “Large Magellanic Cloud Cepheid Standards Provide a 1% Foundation for the Determination of the Hubble Constant and Stronger Evidence for Physics beyond ΛCDM”, Astrophysical Journal **876**, 85 (2019).

[57] A. G. Riess, “The Expansion of the Universe Is Faster than Expected”, Nature Reviews Physics **2**, 10–12 (2020).

[58] J. R. Gott III, M. Jurić, D. Schlegel, et al., “A Map of the Universe”, Astrophysical Journal **624**, 463–484 (2005).

[59] R. G. Clowes, K. A. Harris, S. Raghunathan, et al., “A Structure in the Early Universe at $z \sim 1.3$ That Exceeds the Homogeneity Scale of the R-W Concordance Cosmology”, Monthly Notices of the Royal Astronomical Society **429**, 2910–2916 (2013).

[60] A. M. Lopez, R. G. Clowes, and G. M. Williger, *A Giant Arc on the Sky*, (Jan. 18, 2022) `http://arxiv.org/abs/2201.06875`.

[61] D. C. Pan, M. S. Vogeley, F. Hoyle, Y.-Y. Choi, and C. Park, “Cosmic Voids in Sloan Digital Sky Survey Data Release 7”, Monthly Notices of the Royal Astronomical Society **421**, 926–934 (2012).

[62] F. Hoyle and M. S. Vogeley, “Voids in the PSCz Survey and the Updated Zwicky Catalog”, Astrophysical Journal **566**, 641–651 (2002).

[63] F. Hoyle and M. S. Vogeley, “Voids in the Two-Degree Field Galaxy Redshift Survey”, Astrophysical Journal **607**, 751–764 (2004).

[64] A. Gabrielli, F. Sylos Labini, M. Joyce, and L. Pietronero, *Statistical Physics for Cosmic Structures* (Springer, Berlin, 2005).

[65] R. Arnowitt, S. Deser, and C. W. Misner, “Dynamical structure and definition of energy in general relativity”, Physical Review **116**, 1322–1330 (1959).

[66] R. Durrer, *The Cosmic Microwave Background*, 2nd (Cambridge University Press, New York, 2020).

[67] M. Scrimgeour, T. Davis, C. Blake, et al., “The WiggleZ Dark Energy Survey: The Transition to Large-Scale Cosmic Homogeneity”, Monthly Notices of the Royal Astronomical Society **425**, 116–134 (2012).

[68] D. W. Hogg, D. J. Eisenstein, M. R. Blanton, et al., “Cosmic Homogeneity Demonstrated with Luminous Red Galaxies”, Astrophysical Journal **624**, 54–58 (2005).

[69] G. F. R. Ellis, “Relativistic Cosmology: Its Nature, Aims and Problems”, in *General Relativity and Gravitation: Invited Papers and Discussion Reports of the 10th International Conference on General Relativity and Gravitation, Padua, July 3–8, 1983*, edited by B. Bertotti, F. de Felice, and A. Pascolini (Springer Netherlands, Dordrecht, 1984), pp. 215–288.

[70] G. F. R. Ellis and W. Stoeger, “The ‘Fitting Problem’ in Cosmology”, Classical and Quantum Gravity **4**, 1697–1729 (1987).

[71] D. L. Wiltshire, “What Is Dust? - Physical Foundations of the Averaging Problem in Cosmology”, Classical and Quantum Gravity **28**, 164006 (2011).

[72] L. B. Szabados, “Quasi-local energy-momentum and angular momentum in general relativity”, Living Reviews in Relativity **12**, 1–163 (2009).

[73] D. L. Wiltshire, “Cosmic Structure, Averaging and Dark Energy”, in *Proceedings of the XVth Brazilian School of Cosmology and Gravitation*, edited by S. Perez Bergliaffa and M. Novello (Cambridge Scientific Publishers, Cambridge, UK, 2014), pp. 203–244.

[74] T. Buchert, “On Average Properties of Inhomogeneous Fluids in General Relativity. 1. Dust Cosmologies”, General Relativity and Gravitation **32**, 105–125 (2000).

[75] T. Buchert, “On Average Properties of Inhomogeneous Fluids in General Relativity: Perfect Fluid Cosmologies”, General Relativity and Gravitation **33**, 1381–1405 (2001).

[76] T. Buchert, P. Mourier, and X. Roy, “On Average Properties of Inhomogeneous Fluids in General Relativity III: General Fluid Cosmologies”, General Relativity and Gravitation **52**, 27 (2020).

[77] D. L. Wiltshire, “Average observational quantities in the timescape cosmology”, Physical Review D **80**, 123512 (2009).

[78] I. M. H. Etherington, “On the Definition of Distance in General Relativity.”, Philosophical Magazine **15**, 761 (1933), [Reprinted in: Gen. Relativ. Grav. **39**, 1055–1067 (2007)].

[79] P. J. E. Peebles, *Principles of Physical Cosmology* (Princeton University Press, Princeton, NJ, USA, 1993).

[80] E. V. Linder, “Cosmic growth history and expansion history”, Physical Review D **72**, 043529 (2005).

[81] R. B. Tully, E. J. Shaya, I. D. Karachentsev, et al., “Our Peculiar Motion Away from the Local Void”, Astrophysical Journal **676**, 184–205 (2008).

[82] R. Watkins, H. A. Feldman, and M. J. Hudson, “Consistently Large Cosmic Flows on Scales of 100 Mpc/h: A Challenge for the Standard LCDM Cosmology”, Monthly Notices of the Royal Astronomical Society **392**, 743–756 (2009).

[83] H. A. Feldman, R. Watkins, and M. J. Hudson, “Cosmic Flows on 100 H-1 Mpc Scales: Standardized Minimum Variance Bulk Flow, Shear and Octupole Moments: Cosmic Flows Minimum Variance Moments”, Monthly Notices of the Royal Astronomical Society **407**, 2328–2338 (2010).

[84] F. Qin, D. Parkinson, C. Howlett, and K. Said, “Cosmic Flow Measurement and Mock Sampling Algorithm of Cosmicflows-4 Tully-Fisher Catalogue”, Astrophysical Journal **922**, 59 (2021).

[85] D. Lynden-Bell, S. M. Faber, D. Burstein, et al., “Spectroscopy and Photometry of Elliptical Galaxies. V - Galaxy Streaming toward the New Supergalactic Center”, Astrophysical Journal **326**, 19 (1988).

[86] U. Feindt, M. Kerschhaggl, M. Kowalski, et al., “Measuring Cosmic Bulk Flows with Type Ia Supernovae from the Nearby Supernova Factory”, Astronomy & Astrophysics **560**, A90 (2013).

[87] G. F. R. Ellis and J. E. Baldwin, “On the Expected Anisotropy of Radio Source Counts”, Monthly Notices of the Royal Astronomical Society **206**, 377–381 (1984).

[88] C. Blake and J. Wall, “A Velocity Dipole in the Distribution of Radio Galaxies”, Nature **416**, 150–152 (2002).

[89] A. K. Singal, “Large Peculiar Motion of the Solar System from the Dipole Anisotropy in Sky Brightness Due to Distant Radio Sources”, Astrophysical Journal **742**, L23 (2011).

[90] M. Rubart and D. J. Schwarz, “Cosmic Radio Dipole from NVSS and WENSS”, Astronomy & Astrophysics **555**, A117 (2013).

[91] M. Rubart, D. Bacon, and D. J. Schwarz, “Impact of Local Structure on the Cosmic Radio Dipole”, Astronomy & Astrophysics **565**, A111 (2014).

[92] J. Colin, R. Mohayaee, M. Rameez, and S. Sarkar, “High Redshift Radio Galaxies and Divergence from the CMB Dipole”, Monthly Notices of the Royal Astronomical Society **471**, 1045–1055 (2017).

[93] C. A. P. Bengaly, R. Maartens, and M. G. Santos, “Probing the Cosmological Principle in the Counts of Radio Galaxies at Different Frequencies”, Journal of Cosmology and Astroparticle Physics 04, 031 (2018).

[94] A. K. Singal, “Solar System Peculiar Motion from the Hubble Diagram of Quasars and Testing the Cosmological Principle”, Monthly Notices of the Royal Astronomical Society **511**, 1819–1829 (2022).

[95] N. Secrest, S. von Hausegger, M. Rameez, et al., "A Test of the Cosmological Principle with Quasars", Astrophysical Journal Letters **908**, L51 (2021).

[96] C. Dalang and C. Bonvin, *On the Kinematic Cosmic Dipole Tension*, (Nov. 5, 2021) `http://arxiv.org/abs/2111.03616`.

[97] T. M. Siewert, M. Schmidt-Rubart, and D. J. Schwarz, "The Cosmic Radio Dipole: Estimators and Frequency Dependence", Astronomy & Astrophysics **653**, A9 (2021).

[98] P. Tiwari and A. Nusser, "Revisiting the NVSS number count dipole", Journal of Cosmology and Astroparticle Physics 03, 062 (2016).

[99] M. L. McClure and C. C. Dyer, "Anisotropy in the Hubble Constant as Observed in the HST Extragalactic Distance Scale Key Project Results", New Astronomy **12**, 533–543 (2007).

[100] N. Li and D. J. Schwarz, "Scale Dependence of Cosmological Backreaction", Physical Review D **78**, 083531 (2008).

[101] J. H. McKay and D. L. Wiltshire, "Defining the Frame of Minimum Nonlinear Hubble Expansion Variation", Monthly Notices of the Royal Astronomical Society **463**, 3285–3305 (2016), Erratum: **463**, 3113 (2016).

[102] R. B. Tully, H. M. Courtois, A. E. Dolphin, et al., "Cosmicflows-2: The Data", Astronomical Journal **146**, 86 (2013).

[103] D. Kraljic and S. Sarkar, "Frames of Most Uniform Hubble Flow", Journal of Cosmology and Astroparticle Physics 10, 016 (2016).

[104] W. A. Hellwing, A. Nusser, M. Feix, and M. Bilicki, "Not a Copernican Observer: Biased Peculiar Velocity Statistics in the Local Universe", Monthly Notices of the Royal Astronomical Society **467**, 2787–2796 (2017).

[105] W. A. Hellwing, M. Bilicki, and N. I. Libeskind, "Uneven flows: On cosmic bulk flows, local observers, and gravity", Physical Review D **97**, 103519 (2018).

[106] C. A. P. Bengaly, J. Larena, and R. Maartens, "Is the local Hubble flow consistent with concordance cosmology?", Journal of Cosmology and Astroparticle Physics 03, 001 (2019).

[107] L. Dam, "Inhomogeneous Cosmological Models and the Cosmic Microwave Background", MSc Thesis (University of Canterbury, Christchurch, New Zealand, 2016).

[108] G. Lemaitre, "Evolution of the Expanding Universe", Proceedings of the National Academy of Sciences of the United States of America **20**, 12–17 (1934).

[109] R. C. Tolman, "Effect of Inhomogeneity on Cosmological Models", Proceedings of the National Academy of Sciences of the United States of America **20**, 169–176 (1934).

[110] H. Bondi, “Spherically Symmetrical Models in General Relativity”, Monthly Notices of the Royal Astronomical Society **107**, 410–425 (1947).

[111] J. Plebański and A. Krasiński, *An Introduction to General Relativity and Cosmology* (Cambridge University Press, Cambridge, UK, 2006).

[112] R. G. Buckley and E. M. Schlegel, “Physical Geometry of the Quasispherical Szekeres Models”, Physical Review D **101**, 023511 (2020).

[113] B. J. T. Jones, *Precision Cosmology: The First Half Million Years* (Cambridge University Press, Cambridge, UK, 2017).

[114] G. Lemaître, “The Expanding Universe”, General Relativity and Gravitation **29**, 641–680 (1997).

[115] N. R. Sen, “On the stability of cosmological models”, Zeitschrift für Astrophysik **9**, 215 (1934), [Reprinted in: Gen. Relativ. Grav. **29**, 1477–1488 (1997)].

[116] K. Bolejko, A. Krasiński, C. Hellaby, and Célérier, Marie-Noëlle, *Structures in the Universe by Exact Methods* (Cambridge University Press, Cambridge, UK, 2010).

[117] P. Szekeres, “A Class of Inhomogeneous Cosmological Models”, Communications in Mathematical Physics **41**, 55 (1975).

[118] C. Hellaby and R. G. Buckley, “Rotation, Embedding and Topology for the Szekeres Geometry”, Physical Review D **103**, 043510 (2021).

[119] K. M. Górski, E. Hivon, A. J. Banday, et al., “HEALPix: A Framework for High-Resolution Discretization and Fast Analysis of Data Distributed on the Sphere”, Astrophysical Journal **622**, 759–771 (2005).

[120] A. Heinesen, “Multipole decomposition of the general luminosity distance Hubble law — a new framework for observational cosmology”, Journal of Cosmology and Astroparticle Physics 05, 008 (2021).

[121] K. Bolejko, “Structure Formation in the Quasispherical Szekeres Model”, Physical Review D **73**, 123508 (2006).

[122] R. A. Sussman and I. Delgado Gaspar, “Multiple Nonspherical Structures from the Extrema of Szekeres Scalars”, Physical Review D **92**, 083533 (2015).

[123] R. A. Sussman, I. Delgado Gaspar, and J. C. Hidalgo, “Coarse-grained description of cosmic structure from Szekeres models”, Journal of Cosmology and Astroparticle Physics 03, 012 (2016).

[124] J. H. McKay, “The Cosmological Rest Frame”, MSc Thesis (University of Canterbury, Christchurch, New Zealand, 2015).

[125] K. Migkas, G. Schellenberger, T. H. Reiprich, et al., “Probing Cosmic Isotropy with a New X-ray Galaxy Cluster Sample through the $L_{\mathrm{X}} - T$ Scaling Relation”, Astronomy & Astrophysics **636**, A15 (2020).

[126] A. Heinesen, “Multipole decomposition of redshift drift – model independent mapping of the expansion history of the Universe”, Physical Review D **103**, 023537 (2021).

[127] H. J. Macpherson and A. Heinesen, “Luminosity distance and anisotropic sky-sampling at low redshifts: A numerical relativity study”, Phys. Rev. D **104**, 023525 (2021), Erratum: **104**, 109901 (2021).